Investigating the Impact of Pre-Strain on the Embrittlement Behavior of S355ML Steel in Offshore Wind Turbine Monopiles

MSc Thesis

Sara Fernández Iniesta
5606152

Supervisors:
Casper Versteylen (TNO)
Vera Popovich (TU Delft)

Materials Science & Engineering
Faculty of Mechanical Engineering
Delft University of Technology
The Netherlands
March 2025

Contents

List of Figures

List of Tables

Nomenclature

AC	Air Cooled
$ACPD$	Alternating Current Potential Drop
AF	Acicular Ferrite
$AISI$	American Iron and Steel Institute
$ASTM$	American Society for Testing and Materials
BCC	Body Centered Cubic
$CGHAZ$	Coarse Grain Heat Affected Zone
CLT	Constant Load Test
$CTOD$	Crack Tip Opening Displacement
$DASW$	Drawn-arc stud welding
$DCPD$	Direct Current Potential Drop
$DScell$	Devanathan-Stachurski cell
EAC	Environmental Assisted Cracking
$EBSD$	Electron Backscatter Diffraction
$EDEDM$	Uniform Deformation Energy Density Model
FCC	Face Centered Cubic
$FCGR$	Fatigue Crack Growth Rate
$FWHM$	Full Width at Half Maximum
GND	Geometrically Needed Dislocations
$HA-FCG$	Hydrogen Assisted Fatigue Crack Growth
HAZ	Heat Affected Zone
HE	Hydrogen Embrittlement
$HEDE$	Hydrogen Enhanced Decohesion
HEI	Hydrogen Embrittlement Index
$HELP$	Hydrogen Enhanced Localised Plasticity
HER	Hydrogen Evolution Reaction
$HESIV$	Hydrogen Enhanced Strain-Induced Vacancy
$ICCP$	Impressed-Current Cathodic Protection
IG	Intergranular
kgf	Kilogram-Force

MVC	Microvoid Coalescence
MW	Megawatt
ND	Normal Direction
OM	Optical Microscope
PD	Potential Drop
PF	Proeutectoid Ferrite
PIP	Profilometry-Based Indentation Plastometry
QC	Quasi Cleavage
RD	Rolling Direction
SEM	Scanning Electron Microscope
SPT	Small Punch Test
SSD	Statistically Stored Dislocations
$SSRT$	Slow Strain Rate Test
$SSTT$	Small Specimen Test Technique
TC	True Cleavage
TD	Transverse Direction
TDS	Thermal Desorption Spectroscopy
TEM	Transmission Electron Microscope
TG	Transgranular
TM	Thermomechanical Rolled
$TRIP$	Transformation induced plasticity
UB	Upper Bainite
UDM	Uniform Deformation Model
$USDM$	Uniform Stress Deformation Model
UTS	Ultimate Tensile Strength
WM	Weld Metal
$wppm$	Weight Parts per Million
$wppms$	Weight Parts per Million per Second
XRD	X-Ray Diffraction
YS	Yield Strength

Abstract

Offshore wind turbines are now more essential than ever for transitioning to a greener, sustainable society. Since the foundations of these wind turbines are surrounded by seawater during operation, they must be protected against corrosion. One method of corrosion protection is the impressed current cathodic protection (ICCP) system, which can lead to hydrogen production due to over-protection when the potential falls into the hydrogen evolution reaction (HER) region. S355ML is typically the chosen material for the most common wind turbine foundation type, the monopile, which is bent and welded during its manufacturing process.

In this MSc thesis, the effect of pre-strain and microstructure on the hydrogen embrittlement (HE) behavior of S355ML is studied. Different levels of pre-strain (0%, 2%, 8%, 16%) are applied to S355ML in the thermomechanical rolled (TM) condition. The goal is to study and compare the binding energies of the traps and the hydrogen concentration at each pre-strain level. Additionally, the binding energies and hydrogen concentration of the heat-affected zone (HAZ, replicated by heat treatment) and the TM microstructures pre-strained at 8

To investigate how the mechanical properties of S355ML are affected by the presence of hydrogen in the material, slow strain rate tests (SSRT) and profilometry-based indentation plastometry (PIP) analysis have been carried out on uncharged 0% pre-strained TM samples and hydrogen-charged, 8% pre-strained TM samples. The SSRT tests show that the hydrogen-charged samples experience HE, as the elongation at failure of charged samples decreases with strain rate, with a 37% decrease for the slowest crosshead displacement rate. Since strain rate plays an important role in HE phenomena, it is observed that PIP tests are not suitable for studying the HE behavior of S355ML.

It is found that without the effect of pre-strain, S355ML in the TM condition does not retain hydrogen. Moreover, hydrogen concentration increases with pre-strain following the power law $H = 0.12\epsilon^{0.54}$

Therefore, dislocations seem to be the main traps present in S355ML samples in the two studied microstructures. However, the values of binding energies vary with pre-strain level and microstructure and do not match those usually assumed for dislocations: 19.0 kJ/mol for the traps of 2% pre-strained TM samples, 15.6 kJ/mol for the traps of 8% pre-strained TM samples, 34.2 kJ/mol for the traps of 16% pre-strained TM samples, and 8.2 kJ/mol for the HAZ microstructure with 8% pre-strain. The variation of binding energies with pre-strain and microstructure can be attributed to the presence of overlapping peaks in the thermal desorption spectroscopy (TDS) analysis, making it difficult to apply the Kissinger equation to the correct data points. Consequently, a higher number of samples should be tested to determine the accuracy of the Kissinger theory and the Choo-Lee plot for binding energy determination.

Acknowledgments

I'd like to begin by thanking my supervisors for their invaluable guidance, support and insight throughout this project. To Casper Versteylen, thank you for your innovative, thoughtful feedback and for always listening and supporting my ideas and approach. To Vera Popovich, I am deeply grateful for your expertise, guidance, attention to detail and generosity.

I would also like to extend my sincere thanks to Richard IJzerman, Richard Huizenga, Raymond Dekker, Elise Reinton and Ton Riemslag, who have contributed with their knowledge and were always available to assist with any technical challenges. Your expertise and readiness to help were essential to the successful completion of this project.

This MSc has given me the opportunity to meet and to work with two great men both professionally and personally. I'd like to thank Tim Boot and Pascal Kommelt for always be willing to share their knowledge. Thanks for your guidance. I have grown as a professional working with you, for what I will be forever grateful.

On the same line, I'd like to thank Yaiza González and María Santofimia for being so approachable, helpful and supportive during my Masters. You inspire me.

Thanks to my wonderful friends: Alex, Ana, Eider, Kike, Leila and Pablo. You are my shelter.

Thank you Remi for everything.

Thanks to Fernando, Enrique and Raquel. My life is better since you are in it.
To Lourdes, the one of the miracles, I will forever carry you and all we are learning and growing with me. I consider myself to be really lucky to have had found you.

The fondest thank you to my beloved little family for being my beacon. To my grandparents for caring and providing. To my uncles, aunts and cousins. To my Tía. To my parents, thanks for all the hard work and always having given me the best of you. To the coolest, strongest and most supportive mom. To the most special dad. I wish you were here, although you always are.

1 Introduction

The depletion of fossil fuels, along with the pollution that their use generates, makes the energy transition to greener and more abundant sources of energy an urgent matter. In this context, wind energy it is proving to be a good alternative to hydrocarbons. Although wind turbines have been used to generate electricity since the end of the 19^{th} century, it was not until the 1973 oil crisis when this technology caught more attention of the industry. At first, wind turbines were only located onshore, until in 1991 the first offshore wind farm was built: eleven wind turbines were erected in Denmark, having been in use for 25 years. Since then, offshore wind turbines have demonstrated to be a good alternative to onshore turbines due to the stronger winds of the sea and the bigger size of the offshore turbines compared to the onshore ones; these two factors are translated in more energy generated [1]. Moreover, offshore wind farms can be bigger than onshore ones due to the availability of larger areas in the sea, while causing less visual and noise impacts. As drawbacks, offshore wind turbines are more expensive and complex to install and to maintain. As a consequence, when taking into account the investment per megawatt (MW), offshore wind turbines are 50% more expensive than onshore ones as a consequence of the more complex process of installation [2]. Another factor that makes fixed-bottom offshore wind turbines more expensive is the foundation, as their capital expenditure (CapEx) represents 13.5% of the total of the turbine whereas for onshore turbines, foundations are responsible for 4% of the costs [3].

Monopiles are the most common offshore wind turbine foundation in shallow water (10-30 m depth) due to its simple design and production [4]. The production process of monopiles is the following: steel plates are hot rolled and then cut to the desired size. The resultant sheet is bent via three roll bending process and then the extremes are longitudinally welded to achieve the cylindrical shape. The three roll bending process is a continuous manufacturing process that allows to deform one part of the plate at a time by bending it between three cylindrical rolls and the sheet slides to allow the local deformation of other points of the piece and produce tensile strains in the outer surface of the sheet and compressive strains in the inner surface [5]. These induced strains, together with the ones that the monopiles can go through while in service may have a repercussion in the monopile performance, so study their effects on material behavior is an important matter.

Another issue that the offshore wind turbine foundations have to go through is the risk of corrosion. To avoid monopiles undergoing corrosion two main approaches are taken: coatings and cathodic protection. Coatings serve as as a support of cathodic protection systems, which can be in turn sacrificial anode or impressed current systems. For the sacrificial anode technique, a less noble material that the one that has to be protected is attached to its surface, avoiding by this to be corroded since the sacrificial anodes are preferential sites for corrosion. On the other hand, the impressed current technique makes use of an external power supply to generate one current between the material to be protected, which will act as the cathode, and an electrochemical inert material is chosen as the anode to close the circuit. However, when the cathodic polarization exceeds certain value, hydrogen generation starts to take place causing hydrogen embrittlement of the structure that was wanted to be protected [6].

That is why studying the effect of pre-strain in the hydrogen embrittlement susceptibility of steels that are used for offshore wind monopiles is important, to ensure a good performance during their in-service life.

2 Literature Review

In this section, a literature review of factors that contribute to hydrogen embrittlement for the specific case of wind turbine monopiles is presented in order to try to gather the already known information in this topic and to identify the current gaps of knowledge. To do that, the hydrogen embrittlement phenomena is described, the effect of pre-strain and microstructure is discussed, the different mechanical tests that are usually carried out to study HE are shown and hydrogen detection methods are explained.

2.1 Hydrogen Embrittlement

Hydrogen embrittlement (HE) is being thoroughly investigated in different industries as it is a limiting factor in their development: energy transition, automotive manufacturing, nuclear energy, offshore constructions and refining and petrochemical industries are just examples of the sectors in which this phenomenon occurs.

HE can be defined as the mechanism by which hydrogen deteriorates some mechanical properties of metals (i.e ductility, impact strength [7, 8]) when in contact with them if a critical concentration is achieved, causing delayed and unforeseen failures. However, the presence of hydrogen is not enough to cause HE. There is a synergistic effect of hydrogen, stresses and microstructure that causes a material to be embrittled. This can be understood by the fact that the potentially hazardous hydrogen is the mobile hydrogen. This hydrogen diffuses to areas with higher tensile stresses and deformation levels at low temperatures.

2.1.1 Trapping

Trapping is the process by which hydrogen atoms stay at specific locations of the crystal called traps instead of diffusing through the lattice. The behaviour of the traps depends on their binding energy, which in turn will depend on the metal's composition and microstructure, as well as the loads at which it is subjected to. Traps sites have two main characteristics: saturation and reversibility [9]. The non saturable traps are the ones that increase their ability to store hydrogen as its concentration in the material increases (cracks, voids) while the saturable ones are only capable of storing a finite quantity of hydrogen. On the other hand, depending on their binding energy, the traps can be classified into two categories: shallow or reversible trapping sites and deep or irreversible traps. [10] establishes that strong traps are the ones having a binding energy $>60\ kJ/mol$ and weak traps as the ones with a binding energy $<30\ kJ/mol$ whereas [11] defines weak traps as the ones with a free energy of trapping $|\Delta G| < 35\ kJ/mol$ and strong traps with values of $57\ kJ/mol < |\Delta G| < 70\ kJ/mol$, increasing the binding energy after cold rolling. Figure 1 graphically exemplifies the different binding energies and how they relate to the place in which hydrogen is whit in the metal: E_d is the diffusion energy needed to move through the lattice, E_b is the binding energy of the trap and E_a is the energy needed by the hydrogen to escape the trap. The strong traps are the first ones to be filled according to [12].

Trap's reversibility depends on temperature, as the binding energy can be overcome by thermal activation [13]. The hydrogen present in the reversible traps is the one that can lead to damage in steels given the appropriate conditions. In fact, one way to mitigate HE is to ensure that there are enough and well distributed irreversible traps that are able to retain the hydrogen.

As HE takes place as a consequence of the weak trapped hydrogen diffusing to high triaxiality stresses zones, trapping plays a crucial role in this phenomena. And trapping is determined by the material's susceptibility and applied mechanical loads, which will in turn influence the number of dislocations. So, ultimately, the dislocations and the microstructural features are the main factors influencing HE.

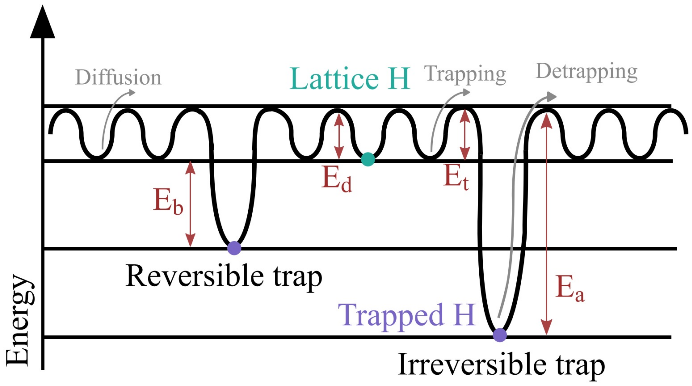

Figure 1: Schematic of the energy states of hydrogen [14]

2.1.2 Effect of Hydrogen in mechanical properties

Hydrogen has an effect on ductility [15, 16]. The ductility loss is usually measured by the HE index, defined in Equation 1, where ϵ_{ch} is the elongation of the charged sample and ϵ_{un} is the elongation of the uncharged sample. The HEI can also be evaluated with the relative strength loss [17].

$$\%HE = 100\left(1 - \frac{\epsilon_{ch}}{\epsilon_{un}}\right) \tag{1}$$

Another property that is affected by hydrogen is the hardness, which usually increases with hydrogen content [7, 8]. Zhao et al. studied the effect that the hydrogen content has on hardness in steel and concluded that high hydrogen quantities cause a hardening effect while low hydrogen content softens the material [12].

Regarding the tensile properties, some studies report that yield strength and Ultimate Tensile Strength (UTS) are not notably affected by hydrogen [18, 16]. However, Vandewalle et al. observe a decrease of UTS with decreasing tensile strain rate [14].

2.1.3 HE submechanisms

The complexity of HE makes it difficult to study and describe it. In order to explain this process thoroughly, different models are being investigated.

2.1.3.1 Hydrogen Enhanced Decohesion: HEDE

This theory explains HE as a consequence of the hydrogen weakening the interatomic bonds in metallic materials. The interatomic forces decrease as the hydrogen content increases [19, 20]. It is based in the fact that hydrogen diffuses to zones of high triaxial stresses, like crack tips. Therefore, when hydrogen diffuses to the front of a crack tip, it lowers the interatomic interactions, decreasing the critical crack tip opening displacement (CTOD). When this critical CTOD is achieved, decohesion takes place [21]. Experimentally, this mechanism is backed up by the reduction of crack tip opening angle with hydrogen content as reported by Vehoff et al. and by the presence of brittle fracture surfaces (i.e cleavage, intergranular) [22]. However, Martin et al. inspected the fracture surface of a nickel alloy, finding that what a lower magnifications looks as a brittle intergranular fracture caused by hydrogen, at higher magnification and resolution shows slip bands underneath which there is a high number of dislocations, arriving to the conclusion that plasticity plays a key role in HE [23]. Li et al. emphasize that the role of plasticity in HEDE mechanism should be further investigated [19].

2.1.3.2 Hydrogen Enhanced Localised Plasticity: HELP

This model is based on hydrogen enhancing dislocation motion and facilitation of dislocation generation [19]. As seen before, the hydrogen diffuses to the highest level of stress, bringing dislocations also there. As a consequence, plastic deformation appears (softening effect) at lower stress levels [21]. This can happen because hydrogen reduces the short-range interactions of dislocations and the stacking fault energy, enabling them to move with less external applied stress [24]. Another study showed the movement of dislocations in stainless steel when hydrogen was introduced in the material [25]. Moreover, it was exposed that fractography surfaces that seemed to be caused by the HEDE mechanism present roughness when looking at them with higher resolution tools and at higher magnification. Moreover, Transmission Electron Microscope (TEM) micrographs revealied high dislocation density just underneath the fractography surfaces, which could be explain with the HELP mechanism [26, 27].

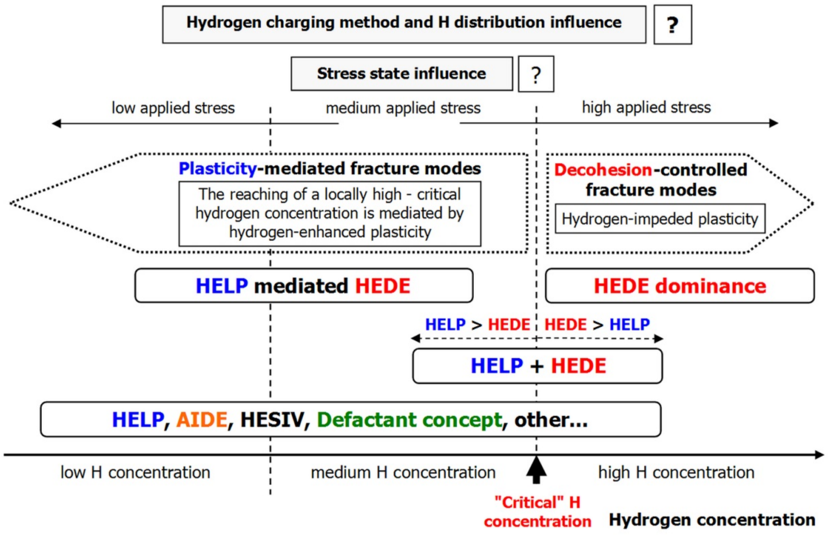

Figure 2: Unified model: HE mechanisms as a function of hydrogen concentration and applied stress [28]

2.1.3.3 Other mechanisms

Figure 2 shows the unified HE model, which relates the HE submechanisms with the hydrogen quantity inside the material and the applied stress. In this model, other HE submechanisms are described. HELP mediated HEDE is based in the idea that HELP is needed to activate HEDE whereas HELP+HEDE defends that HE is a consequence of the synergy of HELP (plasticity) and HEDE (brittleness) [29]. HELP+HEDE supports that, although both mechanisms can coexist, one can be dominant over the other depending on the conditions at which the metal is subjected. The hydrogen-enhanced strain-induced vacancy (HESIV) proposes that hydrogen enhances dislocation clusters and enhances dislocation density [24]. All these proposed submechanisms explain in one way or another the HE phenomena. However, the sometimes conflicting results or the lack of consensus in the literature regarding the definitions of the HE submechanisms themselves make difficult to understand the effect of each one of them in the embrittlement of metals. A deep study of each case should be done using different and complementary characterization techniques to obtain as much information as possible to describe the different HE mechanisms playing a role in the change of properties of the material in contact to hydrogen.

2.2 Hydrogen sources

Hydrogen adsorption and absorption into the metal can occur during the manufacturing processes of the material itself and of the metallic pieces (i.e pipelines, automotive's parts) or during lifetime via direct contact with hydrogen or via corrosion. The hydrogen can enter into the material via gaseous source for or via electrolysis.

2.2.1 Gaseous source

Gaseous hydrogen charging is performed by placing the specimen in a chamber able to store hydrogen gas at different pressures.

2.2.1.1 Adsorption and Absorption:

According to Marcus et al. and Truschner et al., the process of gaseous hydrogen absorption can be seen in Figure 3 and it is summarized in the following steps [30, 31]:

- H_2 is transported to the metal's surface
- Physisorption: Adsorption of the molecular hydrogen
- Dissociation of the molecular hydrogen following the equation:

$$H_{2(g)} + 2(M) \longrightarrow 2H_{ads}(M) \tag{2}$$

  Where:
  (M) is an empty metal surface site for hydrogen
  $H_{ads}(M)$ is a hydrogen atom in a surface site

- Surface-bulk transfer:

$$H_{ads}(M) + [M] \longleftrightarrow H_{diss}[M] + (M) \tag{3}$$

  Where:
  $[M]$is an empty bulk site for hydrogen
  $H[M]$ is a hydrogen atom bonded to a bulk site

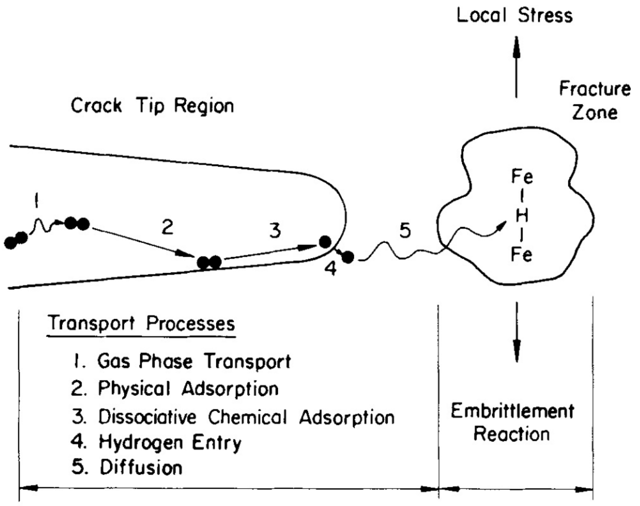

Figure 3: Schematic of hydrogen entry in the metal [32]

2.2.1.2 Effect of gaseous charging parameters in HE susceptibility

Experiments have been taken place with different hydrogen pressures: From low hydrogen pressures as 0.1MPa reported by Williams et al. to pressures up to 96MPa by Loginow et al., all steels subjected to gaseous hydrogen show HE [33, 34]. It has been proven that proven that the HE increased with the pressure of the hydrogen gas [35, 36].

The susceptibility to HE increased also with the strength of the steel [34, 35] as seen in Figure 4 and, while the ductility was degraded, the exposure to gaseous hydrogen did not have a significant effect on the yield strength and ultimate tensile strength [35, 15].

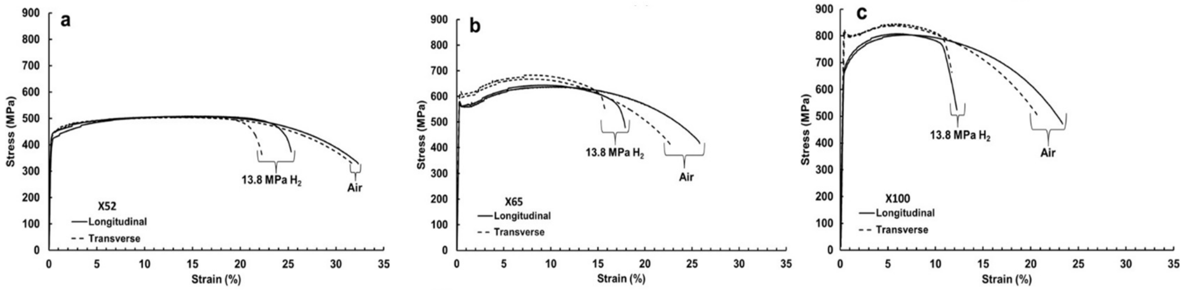

Figure 4: Stress–strain curves for different alloy specimens tested in 13.8 MPa gaseous hydrogen at strain rate of $7 \cdot 10^{-3} s^{-1}$ [35]

2.2.2 Electrochemical source

Another way to introduce hydrogen in the material is by means of cathodic charging using a galvanostat or a potentiostat. In this process the sample to be charged is acting as the cathode to ensure the hydrogen evolution reaction (HER) to happen in its surface. With the help of a recombination poison that prevents molecular hydrogen to be formed, atomic hydrogen goes into the specimen.

2.2.2.1 Hydrogen reactions

An overview of the reactions taking place during HE process in an aqueous electrolyte is described by Marcus et al. and it is summarized below [30]:

- **Adsorption by Volmer reaction in aqueous electrolyte in neutral or basic medium:**

$$\mathrm{H_2O} + e^-_{(M)} + (M)_{aq} \longleftrightarrow H_{ads}(M)_{aq} + OH^-_{(aq)} \tag{4}$$

Where
$e^-_{(M)}$ is an electron given by the metal
$(M)_{aq}$ is one hydrated hydrogen site available for adsorption
$H_{ads}(M)_{aq}$ is a hydrated hydrogen atom adsorbed at a (M) place.

Surface-Bulk transfer of hydrogen:

$$H_{ads}(M)_{aq} + [M] \longleftrightarrow H_{diss}[M] + (M)_{aq} \tag{5}$$

Where
(M) is an empty surface site for hydrogen
$[M]$ is an empty bulk site for hydrogen

The hydrogen can recombine instead of being absorbed following the Tafel or Heyrovsky mechanisms as seen in Figure 5, desorpting from the metal and finishing the HER creating molecular hydrogen.

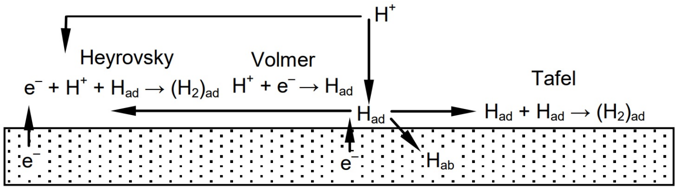

Figure 5: Schematic of the HER (ads: adsorbed, diss: dissolved)[37]

2.2.2.2 Effect of cathodic charging parameters in HE susceptibility

Venezuela et al. report an increase in hydrogen concentration when increasing the overpotential η [36], which is defined as the difference between the applied potential and the equilibrium potential for hydrogen in the solution. This is in line with the study of Hardie et al., where it was observed that the ductility decreases with current density. Nevertheless, the ductility can be recovered leaving the samples enough time at room temperature to allow the diffusible hydrogen effuse from the material [18]. Charging time is also important when introducing hydrogen into the material, increasing the hydrogen content with it [38].

2.2.3 Comparison: Gaseous vs Electrochemical

While gaseous charging can mimic better the conditions that take place in service, it is more expensive and difficult to perform than electrolytic charging. Another drawback of the gaseous charging is that the specimens have to be cooled down after charging, and in that time lapse may be hydrogen effusion.

Liu et al. propose that charging methods can be treated as equivalent if they generate the same activity of hydrogen in steel [39]. The activity is expressed then with the term hydrogen fugacity, which is a measure of how easy is for hydrogen to be uptaken into the metal's surface. On the same line, Koren et al. suggest that is the sub-surface hydrogen concentration the one that can be compared to determine if gaseous and electrochemically charging methods produce the same effects regarding hydrogen content [40].

Venezuela et al. study the way to relate gaseous and electrochemical charging with the equivalent hydrogen fugacity $f_{H_2}^{eq}$ [36]. However, the results obtained are difficult to demonstrate experimentally as the $f_{H_2}^{eq}$ obtained for certain combinations of overpotential and electrolyte are really high and with high degree of inaccuracy (i.e for 0.1M NaOH and -869 ± 35 mV of overpotential, the $f_{H_2}^{eq}$ has a value of 5053 ± 922 bar). However for other combinations of electrolyte and overpotential the results could be experimentally validated and compared with gaseous charging like in the case of 3.5% NaCl at an overpotential of -399 ± 25 mV as the $f_{H_2}^{eq}$ has a value of 136 ± 25 bar. In the latter case a comparison between a gaseous hydrogen charging at 136 bar (typical pressure that high-pressure pipeline steels sustains) and an electrolytic charging with an overpotential at -399 ± 25 mV in 3.5% NaCl electrolyte can be perform to corroborate the accuracy of this method. A drawback of this method is that the fugacity depends on the material, electrolyte and on the applied current density or potential.

Moreover, Nanninga et al. explain that, even if the fugacities of gaseous and electrochemical charging are the same, the processes may be not comparable after necking due to the formation of cracks in the surface (phenomena associated with triaxial stress state at the crack tip after necking) [35]. It is possible that the crack tips vary their chemistry via mass transport or metal dissolution (and thus, their chemical potential) with respect to the bulk material [41]. If that is the case, when in an electrolyte, the material will behave differently than when being gaseous charged even at equivalent fugacities when surface cracks appear.

2.2.4 Comparison: ex-situ vs in-situ charging

While ex-situ charging requires less advanced infrastructures to be carried out, it has the drawback of the potential effusion of the hydrogen during the tests. To avoid hydrogen effusion during ex-situ charging, a thin film of face centered cubic (FCC) material (i.e Zn) can be electrodeposited in the base material to avoid effusion due to the lower diffusivity of FCC as a consequence of their closer packed structures with respect to body centered cubic (BCC) metals. On the contrary, although in-situ charging uses more challenging set-ups, it does not face the problem of hydrogen effusion.

An example of the effect of effusion during ex-situ charging is given by Wang et al. [16]. In this study ex-situ and in-situ hydrogen charging were compared. Although the material was ex-situ charged until saturation, this charging experiment showed almost no HE while but in-situ charging caused a decrease in elongation and showed brittle fracture surfaces and multiple secondary cracks on the gauge surface. On the same line, Zafra et al. studied the effect of gaseous charging conditions in the HE mechanism of a steel subjected to fatigue loading [42]. The ex-situ charged samples showed a fatigue crack growth rate (FCGR) acceleration factor that decreased until reaching a plateau with value 1 for high values of ΔK (i.e, no embrittlement). To understand this, a study of the effect of time and fatigue loading in hydrogen concentration at the crack tip was carried out. While the in-situ charging shows a constant hydrogen concentration ahead of the crack tip, the ex-situ concentration decreases with time. The two-case scenario is depicted in Figure 6, where ΔK, the charging method and frequency are correlated to the hydrogen concentration.

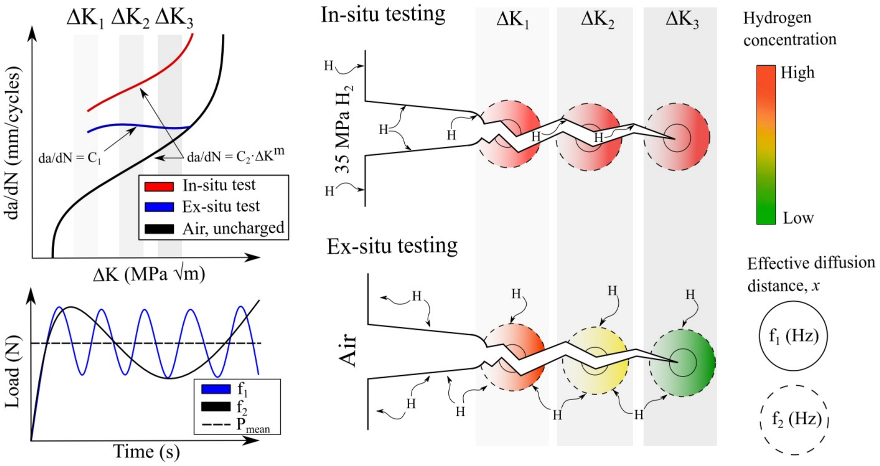

Figure 6: Schematic of the differences between in-situ charging and ex-situ charging. The effect of the frequency on hydrogen diffusion in the crack tip vecinity is shown)[42]

2.3 Effect of microstructure in HE

Microstructure is a key parameter to understand HE behavior of metals, since its different components act as hydrogen traps. In this context, nature (random or special) of grain boundaries, grain size, presence and nature of precipitates and the behavior of different steel phases are the main parameters that are being studied to explain HE. Since it is a broad and difficult to assess topic, this Literature Review will cover the effect of HE in ferritic-pearlitic steels in their tensile properties since this MSc Thesis will study the effect of hydrogen in tensile properties of a ferritic-pearlitic steel. Moreover, the HE in welds will also be described in this section.

2.3.1 HE in ferritic-perlitic steels

Nanninga et al. studied the effect of gaseous hydrogen at 13.8 MPa on the tensile properties of X52, X65, and X100 pipeline steels [35]. X52 and X65 have a microstructure conformed by ferrite and pearlite, the X65 having more pearlite. The test results show degradation in ductility (lower reduction of area and elongation at failure) when testing in the hydrogen atmosphere if compared to the results of the tests performed in air. However, hydrogen did not affected the yield strength and the ultimate tensile strength.

Similar results were obtained when tensile testing X80 at different pressures by Moro et al. in [43]. X80 is another pipeline steel with ferritic–pearlitic microstructure, since it was proven that hydrogen did not influence greatly the yield strength or the tensile strength but it did caused a decrease in the elongation at failure. Apart from that, the strain to failure decreased with the strain rate, showing that lower strain rates increase the HE of this steel.

2.4 Effect of pre-strain in HE

In the context of structural steels, study how pre-strain interacts with hydrogen is useful taking into account that certain manufacturing processing that metallic pieces go through such as rolling, introduce compressive strains in the material. In the specific case of S355, which is used as monopile foundation, the fabrication process also involves pre-straining by three point bending. Moreover, the offshore structures undergo corrosion, which in turn can lead to HE. So for offshore structural materials, the combination of pre-strain with hydrogen is crucial.

However, not only the type of induced strain should be taken into account when studying HE, but also the pre-strain rate and if the pre-strain was induced ex-situ or in-situ.

Li et al. delve into the effect of pre-strain in high strength steels by SSRT exposed to hydrogen [17]. The different levels of pre-strain were produced by tensile SSRT at a strain rate of $2 \cdot 10^{-4} s^{-1}$. It was found that the UTS increases with levels of pre-strain of less than 3% and decreases with higher levels of pre-strain when submitting the samples to SSRT at strain rate of $2 \cdot 10^{-5} s^{-1}$, which is explained by the competing mechanisms of strain hardening and HEDE. For pre-strains higher than 3% HEDE mechanism dominates. On the other hand, elongation decreases with pre-strain for all pre-strain levels. Furthermore, it was also proven that the content of hydrogen increases with pre-strain level as seen in Figure 7, meaning that the dislocations induced by pre-strain act as trapping sites. Moreover, Han et al. concluded that an increase in the level of tensile pre-strain increases the dislocation density [44]. The higher the dislocation density, the lower the effective diffusion D_{eff}, as dislocations act as hydrogen reversible traps. As a consequence, the hydrogen present in the dislocations is able to diffuse until the high stress regions generated in the samples with the tensile test, increasing the HE susceptibility with the level of pre-strain.

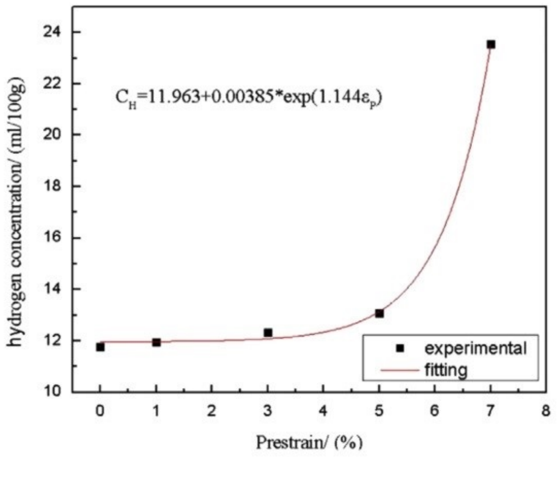

Figure 7: Effects of pre-strain in diffusible hydrogen concentration. Experimental results of [17]

To understand the effect of pre-strain on HE of a 304L austenitic stainless steel, specimens were tensile strained in the plastic region at a rate of $2.7 \cdot 10^{-4} s^{-1}$ to obtain pre-strains of 3, 6, 15, 20 and 25% [45]. It was observed that the HE susceptibility increased with the pre-strained induced martensite α'. When the pre-strain was not enough to generate α', the HE was insignificant, whereas for levels of pre-strain greater than 6%, the martensite α' increased with increasing levels of pre-strain and so did HE susceptibility.

The effect of pre-strain in 304 austenitic stainless steel in a hydrogen environment was also examined by Zhou et al. [46]. Samples were tensile strained at a rate of $5 \cdot 10^{-5} s^{-1}$ until levels of 0, 5, 10, 15, 20, 30 and 40% of pre-strain are achieved. After applying the pre-strain, the following SSRT were performed: group 1 was not pre-charged and was tested in air (hydrogen free, HF), group 2 was cathodically pre-charged and tested in air (hydrogen charged, HC), group 3 was not pre-charged and was tested in 5 MPa hydrogen gas (hydrogen gas, HG) and group 4 was cathodically pre-charged and tested in 5 MPa hydrogen gas (hydrogen charged hydrogen gas, HC-HG). With pre-strain the material became stronger and more brittle. A change in the tendency of elongation with pre-strain is observed in the HC and HG groups at 15% of pre-strain, as illustrated in Figure 8. This is explained by assuming that at pre-strains lower than 10% HE is controlled by environmental hydrogen while for pre-strains of more than 20% the HE is controlled by internal hydrogen. It is also observed that the pre-strained induced martensite α' increases with pre-strain. At 10% pre-strain, the microstructure had 1.27% of α' while for 20% of pre-strain there is a 7.82% of α' in the microstructure. And, as explained in the study, the diffusion coefficient of α' is four orders of magnitude higher than that of austenite, so the diffusion of hydrogen increased with α' content, which will support the theory that for pre-strains higher than 20% HE is mainly controlled by internal hydrogen.

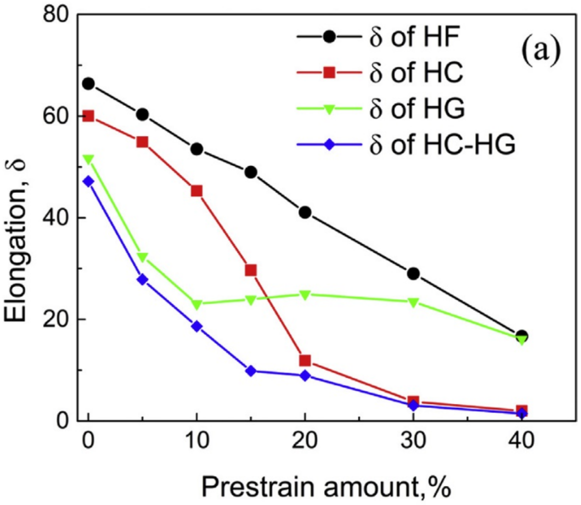

Figure 8: Stress-strain curves of 304 ASS with (a) 0% pre-strain, (b) 10% pre-strain, (c) 20% pre-strain and (a) 30% pre-strain in the four groups tested [46]

The impact of tensile pre-strain in the HE of Transformation induced plasticity (TRIP) steels was studied by Ronevich et al. comparing microstructures and hydrogen embrittlement response to SSRT [47]. The study analyzed the difference states of a same base TRIP steel: as-heat-treated (without pre-strain) and pre-strained 5% at different temperatures (-20ºC, 23ºC, 102ºC), which in turn will have different content of retained austenite and deformation induced martensite. It was proven that the quantity and distribution of the trapped hydrogen in dislocations is what makes the difference in terms of the HE resistance. Therefore, the more uniform the distribution of dislocations in the material, the better. This is explained by the fact that an uniform distribution of hydrogen prevents it from reaching critical concentrations that may cause embrittlement.

2.4.1 Dislocation density calculation: X-ray diffraction (XRD)

Dislocation densities can be measured by different characterization techniques such as TEM, Electron Backscatter Diffraction (EBSD) or X-Ray Diffraction (XRD) [48]. For the XRD case, the analysis is based in the broadening of the peaks that conform the XRD spectra. Peak broadening can appear due to:

- Crystallite size effect: The smaller the crystallites, the broader the XRD peaks as a consequence of having less diffraction planes.
- Lattice distortions as a consequence of strain.

The broadening of XRD peaks is measured as full width at half maximum (FWHM). While the Scherrer method only takes into account the crystallite size effect on peak broadening, other methods exist that take into account the role that microstrains have on XRD's peaks widening, such as the Williamson-Hall method. Within the FH method, different models can be applied to study XRD spectra: uniform deformation model (UDM), uniform stress deformation model (USDM), and uniform deformation energy densitymodel (UDEDM). USDM separates the two peak broadening contributions of peak broadening while having into account crystal anisotropy [49], as it is shown in Eq. 6.

$$\beta_{hkl} \cos\theta = \frac{K\lambda}{D} + \frac{4\sigma}{E_{hkl}} \sin\theta \tag{6}$$

Where:

β_{hkl}: Full Width at Half Maximum (FWHM) for the measured Miller index plane (hkl), in radians,

θ: Bragg angle (degrees or radians),

K: Scherrer constant (shape factor, unitless),

λ: X-ray wavelength (nm or Å),

D: Crystallite size (nm or Å),

σ: Residual stress in the material (GPa),

E: Young's modulus for the measured plane (hkl), in GPa

In order to get the crystallite size D and the residual stress, the USDM Modified Williamson-Hall Plot has to be used. This plot makes use of the term $\beta_{hkl} \cos\theta$ along y-axis and $\sin\theta / E_{hkl}$ along x-axis and it is form by points that correspond to individual XRD peaks. The slope of the line gives the residual stress whereas the intercept represents the crystallite size (D). From there, microstrain can be calculated with the Hooke's law. And dislocation density is then calculated from the strain value obtained.

2.5 Mechanical tests to study HE behavior

Different mechanical tests can be performed in order to study the response of materials exposed to hydrogen. The main ones are fracture toughness, fatigue, constant load and slow strain rate tests.

2.5.1 Fracture toughness tests

Fracture toughness is the mechanical property of the material that describes its resistance to crack propagation. In the context of hydrogen embrittlement is a particularly interesting property to study as the material behavior changes when in contact with hydrogen, the change in crack extension resistance is an important matter for performance evaluation. There are different methods to obtain the fracture toughness of materials, the most used ones are described in the standard ASTM E1820 [50]: using the stress intensity factor K, J-integral and crack tip opening displacement (CTOD) (δ).

2.5.2 Fatigue tests

When a material is subjected to cyclic loading conditions, it can fail at lower stresses than if it is subjected to static loads. This phenomenon is called fatigue. Depending on the number of cycles, fatigue can be classified into low cycle fatigue ($< 10^5$), high cycle fatigue ($10^5 - 10^7$) or ultrahigh cicle fatigue ($10^7 - 10^{12}$).

Nanninga et al. differentiate between two phenomena when fatigue is taking place in a hydrogen environment: hydrogen assisted fatigue crack growth (HA-FCG) and hydrogen embrittlement [51]. In the case of HA-FCG, K_{IH}, the stress intensity factor for a statically applied load in a H-present environment above which subcritical crack growth will happen, is the same as K_{IC}, so the material is immune to the effect of hydrogen when a static load is applied. As seen in Figure 9, type A behavior corresponds to HA-FCG. In type A, the effect of hydrogen decreases the ΔK_{th}, so Stage I starts before. Type B from Figure 9 represents the fatigue curve of a material that is susceptible to HE, as $K_{IH} < K_{IC}$.

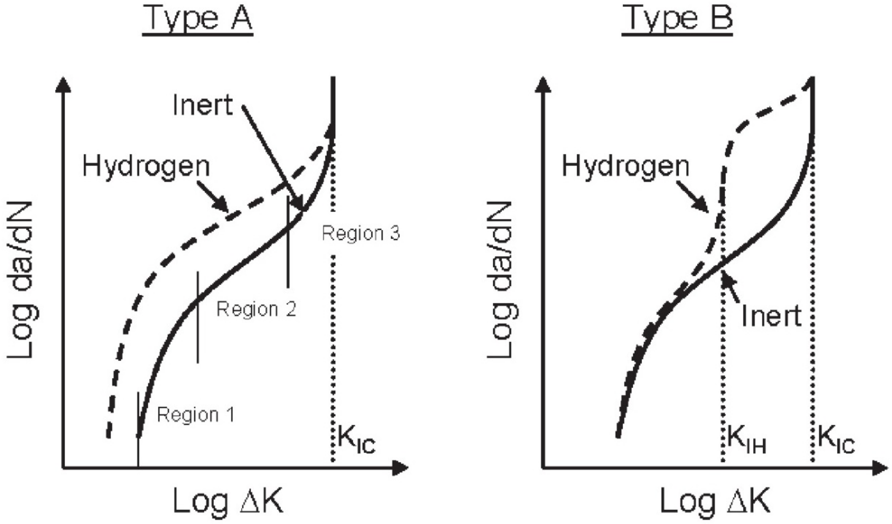

Figure 9: Possible effects of hydrogen on fatigue behavior [51]

2.5.3 Constant load tests (CLT)

In general, the goal to perform CLT on hydrogen charged samples is to find the threshold stress at which there is no failure for a certain content of H in the material. It is simple to perform and gives valuable information such as: time to failure, fracture stress and threshold stress. It is described in ISO 16573-1:2020.

2.5.4 Slow Strain Rate Tests (SSRT)

According to ASTM G129, SSRT is defined as a dynamic slowly increasing strain imposed until the material fails [52]. Regarding this standard, for a test to be considered SSR, the strain rate must be comprised between $2.54 \cdot 10^{-3}$ mm/s and $2.54 \cdot 10^{-6}$ mm/s. This test is used to force the diffusion and accumulation of hydrogen to the zones that concentrate higher stresses in the material [53].

SSRT produces less scattering in the results than constant load tests (CLT) [54]. On the other hand, it tends to be a conservative test to study environmental assisted cracking (EAC) while in other cases it does not reproduce EAC failures seen in service [52]. It was demonstrated that the strain rate plays a fundamental role in HE, since at high strain rates the hydrogen does not have enough time to diffuse to high stress zones and, as a consequence, no HE takes place [37].

2.6 Off-shore wind turbine monopiles

2.6.1 Materials for monopile construction: S355

Offshore wind turbines foundations need to sustain cyclic loads due to wind, waves and tides, that is why structural high strength steels are chosen to construct them. This, together with the need to be weldable, makes the structural steel S355 a good choice one for this purpose.

According to EN 10025-4 [55], S355 is a thermomechanical low alloyed rolled structural steel with a value of the minimum yield strength up to 355 MPa and a maximum tensile strength of 630 MPa. S stands for ”structural” and the termn ML means that the minimum values of impact energy specified in the standard are for temperatures higher than -50 °C.

The chemical composition of S355ML is shown in 1 and its microstructure is composed by ferrite and cementite. This material is widely used in offshore applications such as wind turbine foundations due to good weldability (due to its low carbon equivalent $C_{eq} = 0.28$), high strength as a consequence of their fine grain structure and relatively low cost price [56, 57].

Steel	<%C	<%Si	<%Mn	<%P	<%S	<%Al
S355ML	0.14	0.5	1.6	0.025	0.025	0.02

Table 1: Chemical composition of S355ML steel wt% [55]

2.6.2 Manufacturing of monopiles

As it can be observed in Fig.10, the first manufacturing process steps of monopiles implies bending and welding metal plates. The bending causes the internal radius to be compressed until the neutral axis, and then tensile stresses start from the neutral axis to the outer radius.

The amount of cold working introduced by the bending will vary with the monopile dimensions, and the final microstructure due to welding will also vary depending on the pre-heating treatment,the welding method and the metal sheet thickness. Nevertheless, the presence of pre-strain and HAZ in monopiles can not be avoided.

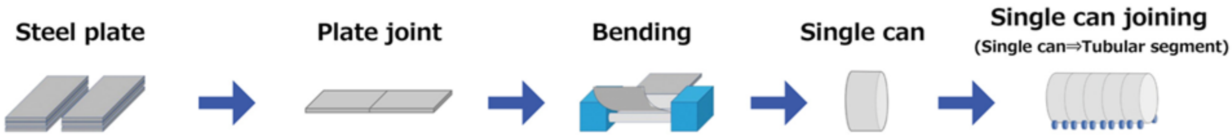

Figure 10: Manufacture process of offshore monopiles [58]

2.6.3 Effect of pre-strain in mechanical behavior of S355

In order to study the effect of the cold work induced during the production process of monopiles, different levels of uniform tensile pre-strain (0%, 5% and 10%) were induced in S355 by Anandavijayan et al [56]. The samples were then subjected to fatigue, since the monopiles are exposed to cyclic loads caused by the wind and waves. It was found that, although fatigue life decreases with increasing levels of pre-strain, the fatigue crack growth was not affected by pre-strain. This latter effect could be due to the competing effects caused by the pre-strain, as it increases the strength of the material at the same time that decreases the strain at failure.

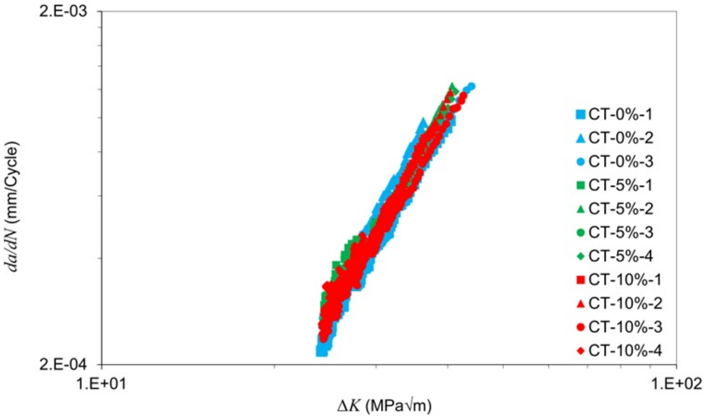

Figure 11: Fatigue crack growth curves for different levels of pre-strain [56]

The same authors delve into the effect of pre-strain in S355 G10+M structural steel [59]. To do that, tensile pre-strains of 0%, 5% and 10% are submitted to fracture toughness tests. They found out the average initiation toughness of the material using 0.2 mm exclusion line. With that data, J_{IC}, was 0.86 $MPa \cdot m$ for the as received specimen (0% pre-strain), 0.79 $MPa \cdot m$ for the 5% pre-strain specimen and 0.71 $MPa \cdot m$ pre-strain specimen. This is explained by the fact that, the higher the pre-strain, the lower the ductility and the energy required for crack initiation is lower. The results of the R-curve for each level of pre-strain can be observed in Figure 12.

Although knowing the effects that pre-strain has in the mechanical response of S355 is useful, the same studies should be carried out including also the hydrogen effect in these properties when the material has been pre-strained. This is justified by the possibility of hydrogen generation during impressed currents cathodic protection processes, as explained before.

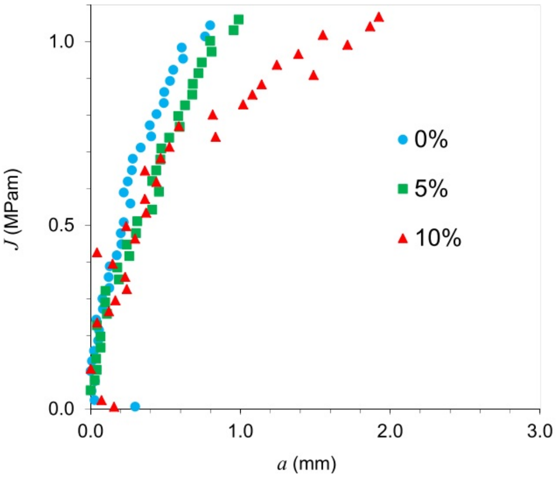

Figure 12: R-curves for different levels of pre-strain [59]

2.6.4 Effect of strain rate in HE behavior of S355

Álvarez et al. examined the effect of strain rate in on the fracture toughness response of hydrogen embrittled S355 and in a quenched and tempered H8 steel [60]. For that, strain rates of 0.1, 0.01 and 0.001 mm/min were applied. It was shown that hydrogen reduced fracture toughness of S355 steel by 60%, although no significant difference is seen between strain rates, as can be seen in Figure 13. It was also observed that the response regarding hydrogen embrittlement is material dependent since the H8 steel shows more HE with decreasing strain rate. This could be caused because the diffusible hydrogen content of S355 was 0.17 ppm while the one of H8 was 0.70 ppm.

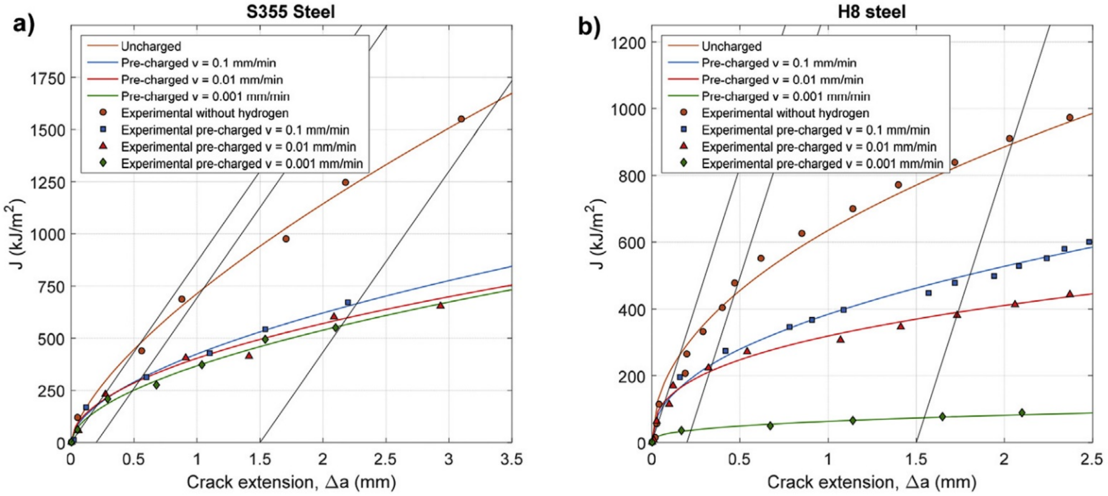

Figure 13: J-R curves for a) S355 steel, b) H8 steel. [60]

To further understand the effect of hydrogen in these two steels, the diffusivity of hydrogen in both cases steels was also determined by means of permeation experiments. The effective diffusion coefficient of S355 is $130 \cdot 10^{-11}\ m^2/s$, while the one of H8 is $8.5 \cdot 10^{-11}\ m^2/s$, around 15 times lower, which can be justified by the presence of more traps in martensite than in ferrite or pearlite. This could explain the difference in behaviors of both steels as a higher trap density will retain more hydrogen and will decrease the hydrogen diffusion coefficient, while the structure of S355 is highly diffusible for hydrogen. To do a more reliable comparison, in-situ tests should be carried out to not have the effect of effusion during the tests.

2.7 Characterization methods to study HE behavior

The way certain concepts are described in literature, such as quasi-cleavage (QC), is inconsistent. M.B. Djukic et al. define QC as "any fracture surface appearance that cannot otherwise be explained as either intergranular (IG), microvoid coalescence (MVC) or true cleavage" in [8] whereas M. Wasim et al. describe QC as the presence of MVC and transgranular (TG) in [61]. In this report, QC will be understood as a characteristic feature of hydrogen embrittled steels that could resemble to cleavage-like fractures but which differs from the latter in its facets: QC facets are smaller and more numerous than for true cleavage (TC).

On the other hand, although certain studies (i.e [62]) sustain that QC is a brittle fracture provoked by HEDE, others such as M.L. Martin et al. came to the conclusion that QC surfaces were produced by void growth and coalescence parallel to slip bands enhanced by the presence of hydrogen and not by true cleavage-like mechanisms [26], information that is supported by A. Nagao et al. [63]. Additionaly, Merson et al. found nano-voids at the tip of secondary cracks of hydrogen-embrittled samples, arriving to the conclusion that nucleation and coalescence of those nano-voids is an intrinsic part of the QC fracture mechanism[64].
There is also the question of what is the difference between TC and QC. Some papers distinguish between them depending on the crystallographic planes in which the crack grows, but different studies obtain contradicting results regarding this data. E. Merson et al. expose the discrepancies when defining the orientation of the crack propagation among a high number of papers and tries to understand if the contradictory conclusions at which they arrive when defining QC are due to to the fact that there is not enough information in this field or because each material behaves differently [65]. Nagao et al. conclude that studying the fractographic surfaces is not enough to know which failure mechanisms take place in the case of HE [62]. Correspondingly, another techniques such as Electron Backscatter Diffraction (EBSD) to investigate the path of the crack and thus to gain insight about the HE phenomena taking place [64, 20] or transmission electron microscopy (TEM) to study the microstructure beneath the fractographic surface [62] are being conducted to understand HE.

Consequently, a more accurate approach is always to combine different techniques in order to have a better understanding of the mechanisms taking place, avoiding biased conclusions. This is specially important when studying the HE submechanisms taking place.

2.8 Hydrogen concentration and binding energy determination by Thermal Desorption Spectroscopy (TDS)

TDS is a technique used to study hydrogen desorption kinetics of a sample that was previously charged with hydrogen. Samples are heated up inside of the TDS and the hydrogen contained in them escapes due to thermal activation. The analyser uses a carrier gas at atmospheric pressure to transport the effused hydrogen gas from the heated sample which is later quantified.

TDS is the most common method by which hydrogen content inside a sample can be measured, usually in weight parts per million (wppm, $\mu g/g$).

H.E. Kissinger developed a method to determine kinetic parameters using thermal analysis. In his studies, small quantities (of the order of mg) of a material were heated at differemnt heating rates Φ and while recording the exothermic peak. The temperature at which the maximum of the exothermic peak takes place (T_m) is measured at each heating rate. He formulated the Kissinger equation (See Eq. 7), which will later be used in 1982 by W.Y Choo and J.Y. Lee to study the activation energy of dislocations in pure iron [66].

$$\frac{d(ln\frac{\Phi}{T_{max}^2})}{d(\frac{1}{T_{max}})} = -\frac{E_a}{R} \tag{7}$$

Where Φ is the heating rate (K/min), $T_{max}(K)$ the peak temperature, $E_a(J/mol)$ de activation energy needed to de-trap hydrogen and R$(J \cdot K^{-1} \cdot mol^{-1})$ the universal gas constant. By plotting ln(Φ/T_{max}^2) vs $(1/T_{max})$, E_a of traps can be determined [67, 68].

2.9 Conclusions

The primary objective of this literature review is to provide an overview of the various parameters that must be considered when studying the Hydrogen Embrittlement phenomena, particularly in the case of wind turbine monopiles.

1. HE submechanisms are not fully understood. To better comprehend the HE phenomena a correlation between an analytical and experimental approach by fractography and the underlying microstructure should be carried out to have a wider perspective on the fracture mechanisms. Also tracking the crack initiation and propagation times and processes could help to understand better the HE mechanisms.

2. Since the main HE submechanisms are based on how hydrogen interacts with dislocations, it is a must to understand the role that dislocation distribution, density and type (screw, edge, mixed) play on HE. Moreover, the fact that dislocations are not static and evolve during mechanical tests should be taken into account.

3. A method to compare electrochemical and gaseous charging still has to be developed.

4. In-situ charging experiments should be done when possible to avoid hydrogen effusion out of the material and to be able to study HE in similar conditions as the ones experienced in service.

5. The response of each material to HE is unique and it is based on its composition and microstructural features, which will determine the nature and density of traps. Therefore, a deep knowledge of the microstructure of the material to be studied should be acquired.

6. A deeper study of the pre-strain in HE should be carried out, disclosing the effect of strain rate, the type of pre-strain (tensile, compressive) and the moment at which the pre-strain is applied with respect to the hydrogen.

7. Due to the bending and welding that S355ML plates go through during the monopile manufacture process, together with the possibility of these monopiles to be exposed to hydrogen while in service, a thoughtful study of the effect of pre-strain and welding (change in microstructure, stress concentrations) on the hydrogen embrittlement behavior of S355ML should be carried out.

2.10 Research goals

To study the effect of pre-strain and microstructure in the HE response of structural steels used to construct offshore wind turbine monopiles, the following points should be researched:

- Study how the hydrogen concentration changes with increasing levels of pre-strain: 0%, 2%, 8% and 16%.
- Relate the hydrogen concentration to dislocation density at different levels of pre-strain: 0 % and 8%.
- Reproduce the HAZ microstructure of S355ML welds and compare its HE behavior to the one of the base metal S355ML at 8% pre-strain.
- Calculate the hydrogen binding energies of the different traps with increasing levels of pre-strain (0%, 2%, 8% and 16%) for the base material and the HAZ microstructure replication.
- Investigate how the mechanical properties of S355ML are affected by the presence of hydrogen in the material.
- Analyze the suitability of PIP method, to be compared with conventional SSRT, to understand how hydrogen affects the mechanical properties of S355ML.
- Perform PIP experiments at different times (10 to 50 minutes) from the end of hydrogen charging to understand if mechanical properties vary due to hydrogen effusion out of the material.

3 Material and Methodology

3.1 Material

According to EN 10025-4 [55], S355 is a thermomechanical (TM) low alloyed rolled structural steel with a value of the minimum yield strength up to 355 MPa and a maximum tensile strength of 630 MPa. S stands for "structural" and the termn ML means that the minimum values of impact energy specified in the standard are for temperatures higher than -50 °C. The chemical composition of S355ML is shown in Table 1 and its microstructure is composed by ferrite and pearlite. This material is widely used in offshore applications such as wind turbine foundations because of its good weldability (due to its low carbon equivalent $C_{eq} = 0.28$), high strength as a consequence of their fine grain structure and relatively low cost price [56, 57].

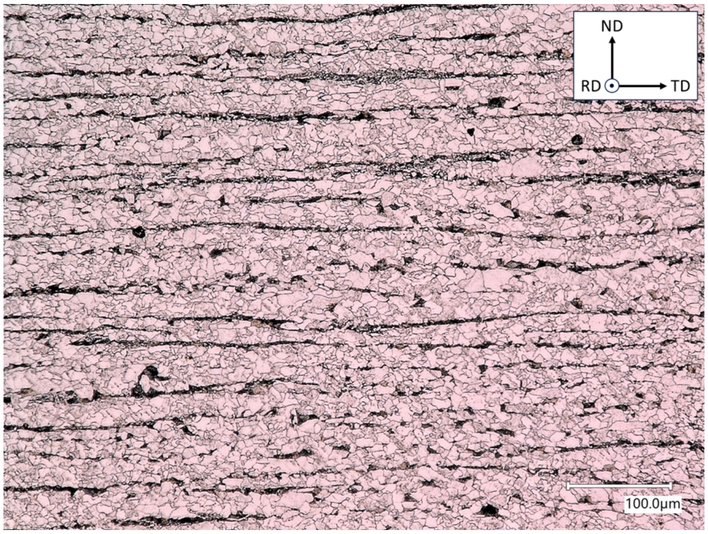

Figure 14: Microstructures of TM samples

Steel	Element Quantity (wt%)									
	C	**Si**	**Mn**	**Cu**	**Mo**	**Ni**	**Cr**	**Ti**	**V**	**Nb**
S355ML	0.093	0.38	1.49	0.030	0.017	0.046	0.034	0.0019	0.0012	0.020

Table 2: Chemical composition of S355ML steel wt%

3.2 Experimental methods

3.2.1 Research Strategy

The strategy followed in this project is summarized in Fig. 15, where it can be seen that:

- Rod samples are used to determine the hydrogen concentration and binding energy of the traps of: 0%, 2%, 8% and 16% of S355ML in the TM microstructure and 8% of the 1050AC microstructure.
- The HE behavior of the S355ML is studied with through SSRT and PIP tests. Both tests are performed in 0% pre-strained, uncharged samples and hydrogen charged 8% pre-strained with

TM microstructure.

- The dislocation density of 0% and 8% pre-strained TM samples was researched with the intention to relate it to the hydrogen concentration variations at different levels of pre-strain.
- The effect of stress in the diffusion of hydrogen out of the 8% pre-strained TM samples with time was investigated by comparing the hydrogen concentrations of SSRTand PIP samples after failure and completion of the test respectively, to samples that were charged for the same amount of time and were left in the laboratory at ambient temperature (TDS samples).

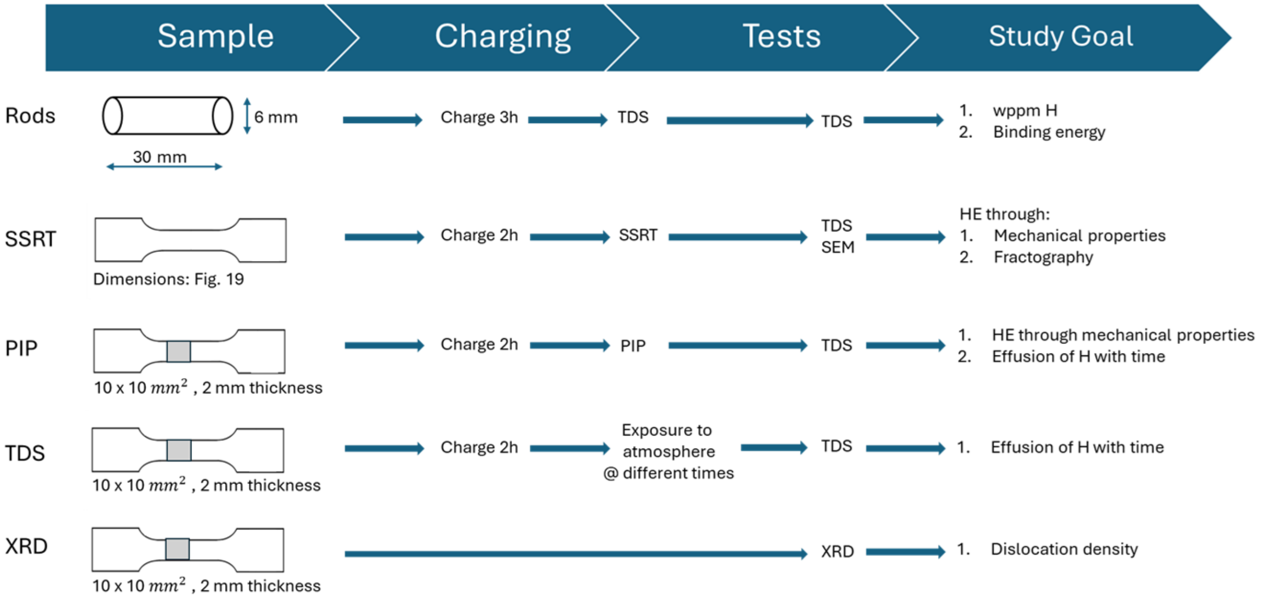

Figure 15: Schematic of the research strategy of this MSc Thesis

3.2.2 Overview of Samples

Fig. 16 shows the samples' orientation with respect to the rolling direction (RD). The samples used to determine how hydrogen content and binding energy vary with pre-strain and microstructure in Section 3.2.3 and the ones used in SSRT tests in Section 3.2.4.1 are machined with their long direction parallel to RD.

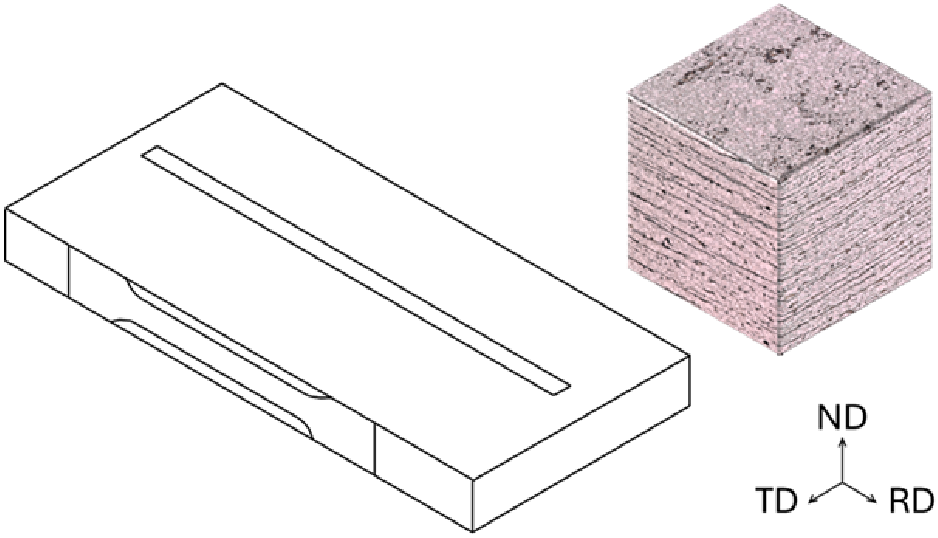

Figure 16: Schematic of the different sample types with respect to rolling direction, transverse direction (TD) and normal direction (ND)

3.2.3 Hydrogen content and trapping energy determination

3.2.3.1 Sample preparation

The samples used for determining the trapping energy were water jet cut (to preserve the TM microstructure) 300 mm long rods with 6.4 mm diameter. Some of these rods went through a heat treatment (1h at 1050°C and then air cooled) to replicate the HAZ microstructure. Then, two different preparation methods were followed:

- **Sample preparation method 1** (carried out at TNO): Samples were machine cut, then the base and the top of the sample were polished. After that, spot welding was applied to the top of the sample to join it to an Ag wire to prevent the metal clamps to touch the solution when charging, preventing galvanic coupling and thus unnecessary corrosion to take place, as well as avoiding an alternative pathway for the current to flow to the clamps. When the spot welding was applied, the sample was polished with a grinding paper of 46 μm SiC grinding paper in the lateral section. As a last step, the Ag wire was electrically insulated with a PU coating.
- **Sample preparation method 2** (carried out at TU Delft): To save preparation time, this procedure was developed. The 300 mm rods were hand sewed after the application of the pre-strain. Then, the samples were polished with 75 μm followed by 46 μm SiC grinding papers. The samples that followed this method were totally submerged and where directly clamped with a metal clamp when charged.

An overview of the samples used to determine trapping energies can be seen in the Table 3 and the steps followed to obtain the necessary data needed to apply the Kissinger's equation are described in Fig. 17

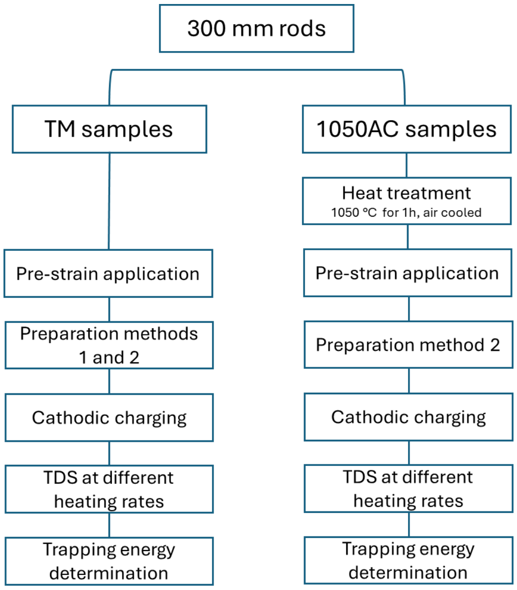

Figure 17: Schematic of the process followed by the samples used to determine the hydrogen trapping energy in TM and 1050AC samples

Microstructure	**Pre-strain (%)**	**Preparation method**	**TDS heating rate (°C/s)**
TM	0	1	1
TM	2	1	0.66, 1, 1.5
		2	0.8, 1.2
TM	8	1	0.66, 1, 1.5
		2	0.8, 1.2
TM	16	2	0.8, 1, 1.2, 1.5, 2
1050AC	8	2	0.8, 1, 1.2, 1.5

Table 3: Table representing the TDS heating rates for different microstructures and pre-strain conditions.

3.2.3.2 Electrochemical charging

3.2.3.2.1 Potentiostatic charging The charging method applied in this study is the electrochemical potentiostatic charging. A negative potential is applied to the WE, cathodically charging it to allow atomic hydrogen to be formed in its surface, which later will be absorbed.

The RE is an Ag/AgCl electrode and the CE is a rectangular net of Pt electrode that acts as the anode. To determine the potential at which the charging experiments were going to take place, and following [69], two cathodic polarization curves at a sweep rate of 0.5 mV/s were conducted in two 0% pre-strained TM samples in order to determine the hydrogen reduction potential. The hydrogen reduction potential is between -900 to -1000 mV (Ag/AgCl), as seen in Fig. 18.

According to [69], the HE susceptibility increases with a decrease in the charging potential in ranges between -800 mV and -1200 mV (vs SCE). As a consequence, the chosen potential to be applied in charging was -1200 mV (vs Ag/AgCl, which is -1.156V vs SCE), with an overppotential of -1.2 V to the hydrogen evolution reaction potential (HER).

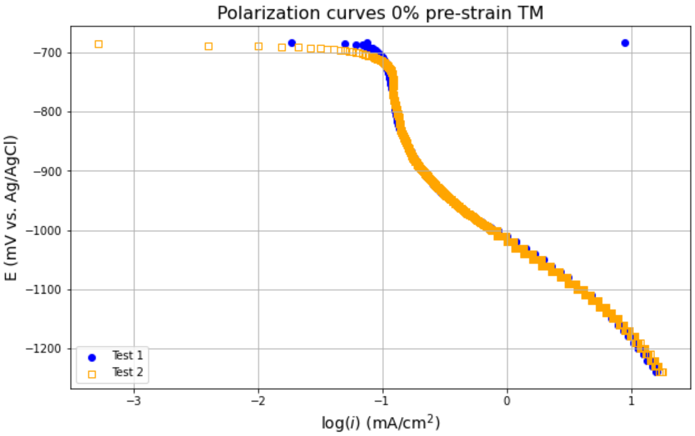

Figure 18: Cathodic polarization curves of 0% pre-strain TM samples in 3% NaCl + 0.3% ammonium thiocyanate with a sweep rate of 0.5 mV/s.

3.2.3.2.2 Time Once the hydrogen reduction potential was determined, different charging experiments with diverse charging times (3.5h, 7h, 21h) were carried out in 0% pre-strained TM samples to define the optimal charging time. As no difference between charging times was observed, the chosen charging time was set to 3.5h since it is the most efficient one.

3.2.3.2.3 Electrolyte The chosen electrolyte is 3% NaCl + 0.3% ammonium thiocyanate following studies such as [70] and based on prior experiments (external research project at TATA Steel Europe), since the hydrogen quantity that was obtained within the same conditions to the same material and sample geometry and preparation method was consistent and with low standard deviation. Ammonium thiocyanate has been used as a recombination inhibitor to prevent the reaction of atomic hydrogen, increasing the hydrogen uptake into the samples during cathodic charging (i.e suppresses the Tafel and Heyrovsky reactions).

3.2.3.3 TDS analysis

A Bruker G8 Galileo, together with an external infrared IR furnace, were used to measure the hydrogen quantity within the samples. The sample were placed in the IR furnace and heated up until all hydrogen was released. Each combination of pre-strain and heat treatment was charged at least four times to then be heated at different heating rates (see Table 3) so the Kissinger theory could be used to determine the binding energy of the different traps present in the samples to be studied.
The TDS results had to be modified to convert them to wppm/s (weight parts per million per second).

TDS data analysis steps:

1. Define the temperature range of the TDS test having into account the heating rate (the speed at which the sample is heated), which in turn determines the time delay that takes the hydrogen to leave the sample and get to the sensor such as

$$T_{\text{actual}} = T_{\text{measured}} - \text{Heating rate } (^\circ\text{C/s}) \times 33 \text{ (seconds)} \tag{8}$$

2. The baseline of the sensor output values is subtracted from the hydrogen signal. Only the positive values of hydrogen's signal are taken into account to get the total amount of hydrogen measured.
3. The total quantity of hydrogen (H_{total}) is obtained by adding all the positive values of the hydrogen signal (integral) and dividing it by the Slope. The slope of the hydrogen signal curve from the G8 Galileo software is obtained dividing the adoption factor (2000000) by the calibration factor.

$$\text{slope} = \frac{2000000 \text{ (Adoption factor)}}{\text{Calibration factor}} \tag{9}$$

$$H_{total} = \frac{\text{Calibration factor} \times \text{integral}}{2000000 \text{ (Adoption factor)}} \tag{10}$$

4. To get the total hydrogen concentration in the sample,

$$H_{wppm} = \frac{H_{total}}{\text{Sample weight (g)}} \tag{11}$$

5. H_{wppm} has to be multiplied by 5 (since the TDS sensor gives 5 data points per second) in order to finally get the $H_{wppm/s}$ value.

3.2.3.4 Binding energy determination

Since the obtained data from TDS is noisy, fitting into a smoother line was needed to determine with the highest accuracy possible the temperature at which the maximum of the peak takes place, which will be needed to calculate the binding energies. The TDS spectra ($H_{wppm/s}$ vs T_{actual}) was fitted in two ways:

1. With one Gaussian distribution function: Assumes that TDS's peaks are formed by only one kind of trap.
2. Deconvoluting the TDS spectra into a fit that is conformed by adding two Gaussian distribution functions. This fitting method assumes that each TDS peak is conformed by two different, smaller peaks: Peak 1 and Peak 2. Each one of them represent a different trap.

To ensure a reliable deconvolution of the TDS spectra, the two Gaussian peaks must be similar in size to agree to the Oriani's bulk diffusion theory, which states that the concentrations of hydrogen in all trapping sites must be of the same order [71]. A difference in size between both peaks of 10% was allowed .

The goal of both fitting methods is to obtain the temperature at which the maximum effusion of hydrogen takes place, T_{max}. Once T_{max} is obtained,it is possible to apply the Kissinger equation to the different heating rates to study which approach is better determining the binding energy of the traps. The procedure to obtain the single Gaussian fit and the deconvolution into two Gaussian fits appears in Annex B.

3.2.4 Study of effect of Hydrogen in Mechanical Properties

3.2.4.1 Slow Strain Rate Test (SSRT)

The SSRT were carried out in a GTM Gassmann Theiss Messtechnik GmbH Load Cell of 100 kN with Instron tensile grips. The test matrix can be seen in Table 4.

Sample Code	Pre-strain **(%)**	**Charging time (h)**	**Displacement rate (mm/min)**
SSRT1	0	-	1.00
SSRT2, SSRT3	8	2	2.70
SSRT4	8	2	0.46
SSRT5, SSRT6, SSRT7	8	2	0.11

Table 4: SSRT test matrix

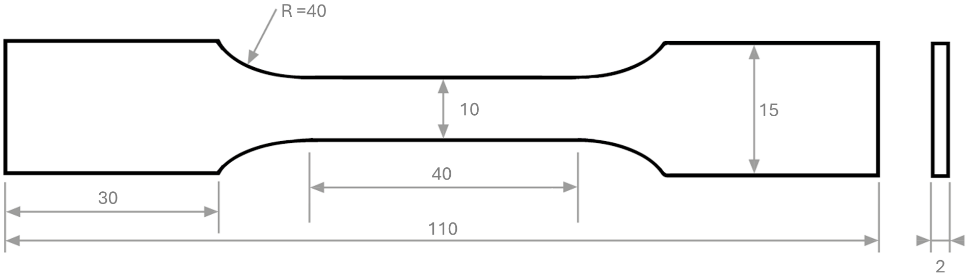

Figure 19: SSRT geometry and dimensions (mm)

The SSRT samples are obtained by water jet cutting to preserve the TM microstructure and their dimensions can be observed in Fig. 19. The samples were manually polished with 75 μm followed by 46 μm SiC grinding papers and then charged for 2h with a potential of -1.2 V vs Ag/AgCl. Once the charging was finished, they were cleaned with demi water, blown dry and placed in the tensile test machine prepare test to be

3.2.4.2 Profilometry-based Indentation Plastometry (PIP)

PIP tests obtain a material's stress-strain curve from an indent profile by using inverse finite element analysis. First, an indenter creates an indent of 1mm diameter. Then, a profilometer measures the indent's profile and uses this data, together with the indentation force (538 N for the 0% pre-strained and 601 N for the 8% pre-strained) and the Young's modulus and Poisson's ratio of the material (200 GPa, 0.3), to iterate between values of different parameters of the constitutive plasticity law until the maximum compatibility of profiles is achieved between the experimental test and the modeled one. A more detailed explanation of the method followed in order to obtain information about the elasticity and plasticity of the tested material is described by Y.T. Tang et al. in [72]. This study used the same device as the one used in this project: the PLX-Benchtop from Plastometrex, which makes use of the Voce equation:

$$\sigma = \sigma_S - (\sigma_S - \sigma_Y) \exp\left(\frac{-\varepsilon}{\varepsilon_0}\right) \tag{12}$$

where

- σ: von Mises stress
- ϵ: von Mises strain
- σ_Y: Yield stress

- σ_S: Saturation stress (stress at which further straining has no effect on hardening)
- ϵ_0: Characteristic strain (strain when stress is at the saturation level)

These tests were performed to study a possible variation inmechanical properties with time in atmosphere after charging as a consequence of hydrogen effusion at room temperature. The results of the PIP tests will be compared to the ones of the ex-situ SSRT in order to determine if it is a suitable method to study elastoplastic behavior of S355ML.

PIP samples where obtained from the gauge of untested 0 and 8% pre strained SSRT samples by cutting 10mm sections (10x10x2 mm^3) polishing until 4000 SiC polishing paper and charging them for 2h in 3% NaCl + 0.3% ammonium thiocyanate with a potential of -1.2 V vs Ag/AgCl.

The electrolyte was changed every time and the samples were totally submerged and directly clamped with a metal clamp. After charging, one surface was manually polished again for 5-10 seconds with 4000 SiC grit paper to ensure a smooth surface, which is needed for the test. Samples 0ps (0 % pre-strain) and 8A (8 % pre-strain) were not charged, they serve as a baseline, in order to be compared with the charged ones. [73]

Sample	Heat Treatment	Pre-strain (%)	Charging time (h)
0ps	TM	0	0
8A	TM	8	0
8H1, 8H2	TM	8	2

Table 5: Sample Information

3.2.4.3 Microhardness

3.2.4.3.1 Vickers Hardness Microhardness measurements were carried out to study the variation of the mechanical properties after the heat treatment applied to 1050AC samples, to see if they follow the same hardness trend that the HAZ of S355 present in literature. DuraScan micro hardness testes was used to perform one series of 10 in-line measurements in each of the microstructures to be studied: TM and 1050AC. The measurements were carried out applying 0.5 kilogram-force (kgf).

3.2.4.3.2 Brinell Hardness Brinell hardness tests were performed right after every PIP experiment. In this case only TM samples were tested and the objective was to see if the hardness values of TM microstructure descended with time after charging, which could be a sign of hydrogen effusion from the samples.

3.2.5 XRD

XRD was performed in order to determine the dislocation density, for which the differences in peak widths of different samples were measured. Two samples were inspected in the direction of application of pre-strain (parallel to RD): a 0% pre-strained and a 8% pre-strained TM samples. The specimens were obtained from the gauge of untested 0 and 8% pre strained SSRT samples by cutting 10mm sections of it, measuring the XRD samples 10x10x2 mm^3. One of the two 10x10 mm^2 surfaces were manually polished until 1 μm diamond particle's size.

The Bruker D8 Advance diffractometer Bragg-Brentano geometry made use of Cu K radiation at 45 kV and 40 mA.

The samples were illuminated a length of 7 mm to avoid the effect of sample's edges in the measurement. The specimmen was not spinned during the measurement. Soller Slits at 2.5°were used in order to enhance resolution by minimizing peak broadening. LynxEye XE-T Position Sensitive Detector was used in High Resolution setting. The data was evaluated making use of Bruker software Diffrac.EVA vs 7.1.

The measured parameters are θ-2θ, with a step size of 0.02° 2θ, being the acquisition time 1s per step.

In order to analyze the results and obtain the dislocation density corresponding to the different levels of pre-strain (0% and 8%) in the samples that will be used for ex-situ SSRT, USDM was applied.

3.2.6 Characterization Techniques

3.2.6.1 Scanning Electron Microscope (SEM)

JSM-IT100 InTouchScope Scanning Electron Microscope was used for fractographic examination (HE signs determination) and 2D area measurement of fracture surface in order to assess the HE index by area reduction. In this case the area was calculated by measuring the length of the sample and multiplying it by an average of the width of the specimen, which was obtained by measuring the width of the fracture surface every 350 μm in length.

3.2.6.2 VHX5000

Keyence VHX-5000 Digital Microscope was used in order to study the microstructure (determine the grain size and the phases that conform the TM and 1050AC samples). After grinding, polishing and etching with 5% nital (5% nitric acid, HNO_3, and 95% ethanol), the microstructures were analyzed in the Keyence to determine their characteristics.

- The grain size was determined following the Average Grain Intercept Method in five areas of the etched surface with a 500x magnification. To decrease the effect of texture in the grain size determination, circles (instead of straigth lines) were drawn over the revealed microstructure. The number of grains that are intercepted by the circle are counted and then the Mean Intercept Length is calculated by dividing the circle perimeter per the number of intersected grains. Only the ferrite grains were taken into account.
- Phase determination: it was used to determine the percentage of pearlite in the TM structure. It is a subjective method since the pearlite percentage is obtained by measuring the area that was above a threshold value (chosen by the user performing the test), so the pearlite content will vary depending on who is performing the test.

4 Results and Discussion

4.1 Microstructure characterization

Two microstructures are tested in this project. The first one is the material as received, in thermomechanical rolled (TM) condition. For the second microstructure, a heat treatment of TM samples is carried out as will be later described in subsection 4.1.2 in order to reproduce the welding microstructure of S355ML. The idea is to later study which role plays the microstructure of this steel in hydrogen trapping.

Microstructure characterization and hardness measurements have been carried out in both TM and 1050AC samples. The microstructural features and the hardness values and relative changes have been compared to the ones found in literature to discern whether or not 1050AC samples are a reliable representation of the weld that can be found in monopiles made of S355ML.

4.1.1 Thermomechanical rolled (TM) samples

TM samples have a grain size of $7\mu m$ and pearlite represents 16% of the microstructure in the direction observed

4.1.2 Replication of weld microstructure by heat treatment: 1050AC samples

When looking in literature for the microstructure of HAZ of S355ML, only a few articles that studied the HAZ microstructure were found. [74] was the article that showed, not only the HAZ microstructure of S355ML, but it also compares it to the one of S355J2+N, which appears to be quite different even thought they have similar chemical composition, highlighting the importance to look only at this specific steel in the literature when looking for HAZ microstructures. The main difference between the two alloys is that S355ML has less carbon, which increases its weldability, and in terms of microstructure, the production method is different since S355ML is TM and S355J2-N is normalized.

Fig. 20 depicts the heat treatment that TM samples were subjected to in order to get the 1050AC samples.

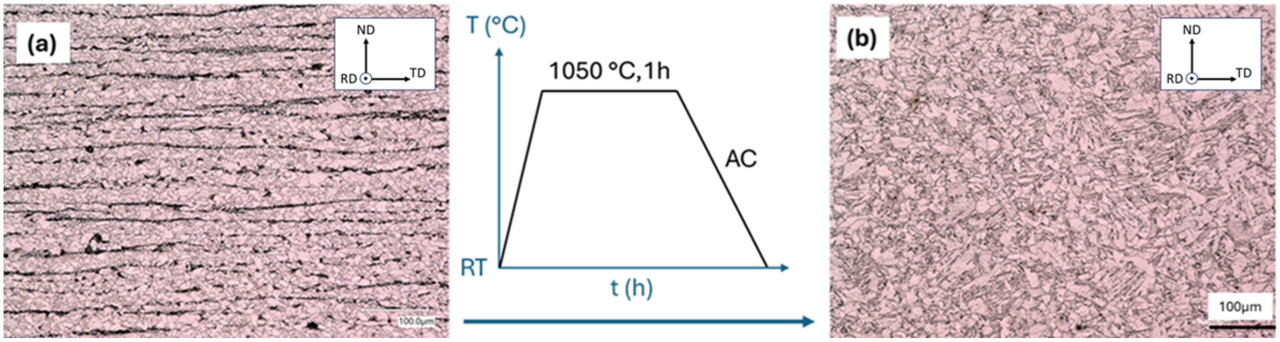

Figure 20: Microstructures of (a) TM samples and (b) 1050AC samples at 500x magnification in transverse direction (TD)

As seen in Fig. 21, the Continuous Cooling Transformation (CCT) diagram shows the different phase transformations depending on cooling rate. The article describes a CGHAZ of S355ML formed by proeutectoide ferrite (PF), upper bainite (UB) and acicular ferrite (AF), and Fig. 22 compares it to the 1050AC microstructure, where PF, UB and AF can also be observed. As a consequence, the 1050AC samples are assumed to be a good replication of the CGHAZ of S355ML stud weld.

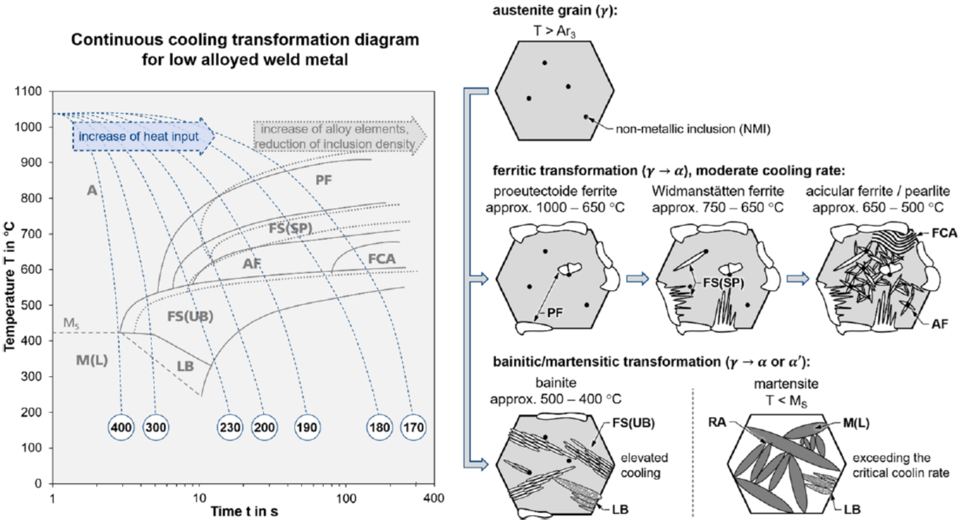

Figure 21: Schematic CCT diagram for non- or low-alloyed ferritic weld metal [74]

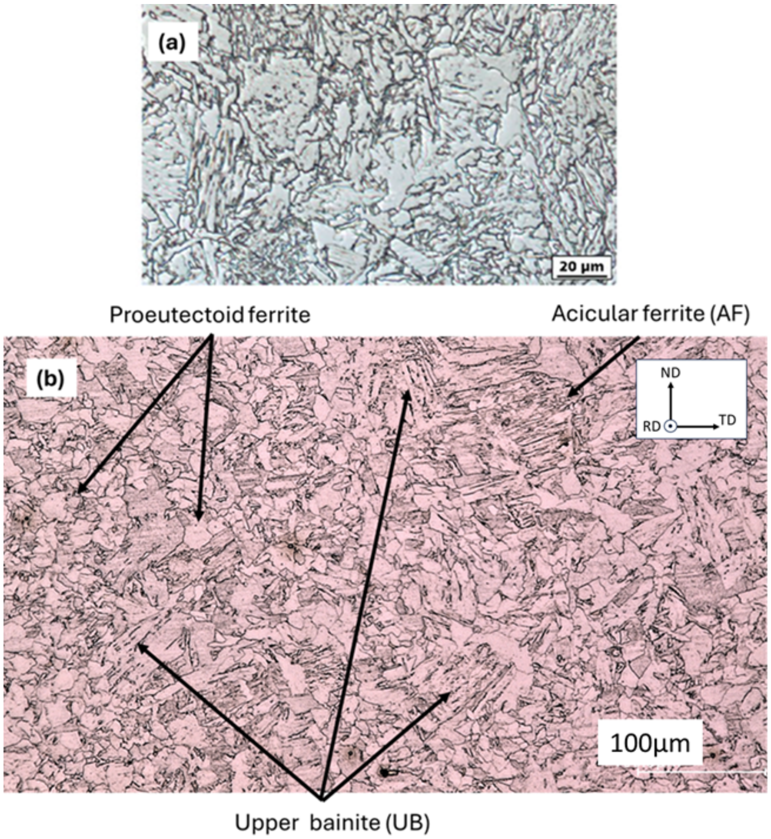

Figure 22: Comparison of the (a) CGHAZ of S355ML from [74] to (b) 1050AC microstructure

4.1.3 Hardness of TM and 1050AC samples

In [74] the hardness of the HAZ and WM is also studied with respect to the BM. As it can be seen in Fig. 23, the hardness of S355ML (HV0.3) does not show relevant hardening in the HAZ, which is consistent with the results of the microhardness measurements (HV0.5) obtained for both microstructures that can be found in Table 6.

Microstructure	Hardness value (HV 0.5)
TM	176.8±6.3
1050AC	171.0±3.8

Table 6: Hardness values obtained in the laboratory for both microstructures studied in this project

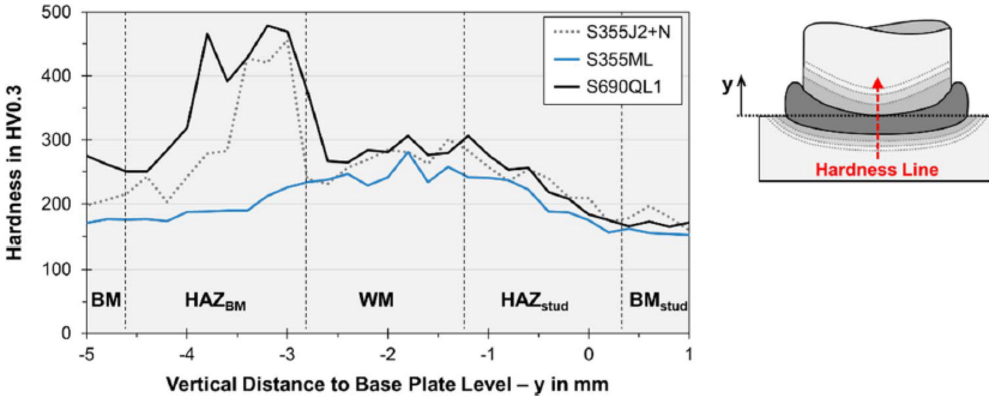

Figure 23: Hardness in weld region of DASW joint [74]

4.1.4 Key findings of microstructure characterization

After both microstructures have been inspected, tested and compared: it seems that the heat treatment applied in this project to the TM samples is able to obtain a similar microstructure to the one described in [74] and shown in Section 4.1.3. Regarding the hardness values obtained, a substantial difference between both sample's group is not observed, which also match literature results.

-Note that in [74] the effect of Drawn-arc stud welding (DASW) is studied, so the microstructure that it shown in the paper and that is taken as a reference may not be directly translated to the case of the welds performed during monopile manufacturing. However, due to the lack of information regarding the microstructural features of the weld of the specific alloy S355ML in the specific case of monopile construction, the microstructure that is shown as CGHAZ in [74] is taken as a reference in this MSc thesis.

Moreover, the 1050AC samples lack the welding residual stresses that could be found in monopiles and that will likely play a role in hydrogen trapping and emnbrittlement of the S355ML. Nevertheless, cooling rates in the case of monopile manufacturing will, most likely, be slower than the ones experienced in the case of stud welds, since DASW presents high cooling rates (For DASW with diameters larger than 12 mm cooling times in the range of $t_{8/5} = 3 - 5$ s are expected.

4.2 Effect of pre-strain in hydrogen trapping

As mentioned before, dislocations play a key role in HE. In this section, the effect of tensile pre-strain in the hydrogen trapping behavior of S355ML in TM and 1050AC samples will be studied in two ways: analyzing how hydrogen concentration changes with pre-strain level and microstructure and studying the binding energy of the different traps.

In order to study these two concepts, groups of same microstructure (TM or 1050AC) and pre-strain levels (0%, 2%,8% and 16%) were heated in the TDS at different rates after being charged for 3.5h in order to obtain the Choo-Lee plot, that will allow to obtain the binding energy of the different traps present in each case.

A filtering method described in Annex C was applied to the different TDS spectra obtained for each particular combination of microstructure and pre-strain in order to increase the reliability of the trap binding energies obtained applying the Kissinger's theory.

The samples followed two preparation methods before being charged, as discussed in Section 3.2.3.1. However, no difference was found in the results among these two methodologies.

4.2.1 Hydrogen trapping in 0% pre-strain TM samples

When the TM samples were not subjected to pre-strain, the hydrogen concentration obtained in the TDS after charging them was no different to the hydrogen concentration of uncharged samples. 0.05 wppm of hydrogen was obtained regardless of the charging time. As a consequence, it is considered that the amount of dislocations that are present in the TM samples is not enough to trap hydrogen, so 0% pre-strained TM samples are taken as the baseline.

4.2.2 Hydrogen trapping in 2% pre-strain TM samples

Five 2% pre-strained TM samples were tested in the TDS with five different heating rates: 0.66, 0.8, 1, 1.2 and 1.5 °C/s. After filtering the data, only the peaks corresponding to the 0.66 °C/S, 0.8 °C/S, 1.2 °C/S, and 1.5 °C/S heating rates are taken into account in the binding energy determination whereas 1 °C/S TDS spectra is seen as an outlier.

Since the 0.66 °C/s TDS spectra is formed by two different peaks as Fig. 24 shows, it was decided that the TDS spectra of all samples used to determine binding energies of traps would follow two different approaches to determine the binding energy: the first one treats the TDS spectra as one peak (i.e only one trap) and will be refereed as "single Gaussian fit", whereas the second one assumes that each TDS peak is constituted by 2 smaller Gaussian functions called "Peak 1" and "Peak 2". For the later case, a deconvolution of the TDS spectra into 2 Gaussian distribution functions has been carried out following the procedure shown in Annex A and Annex B.

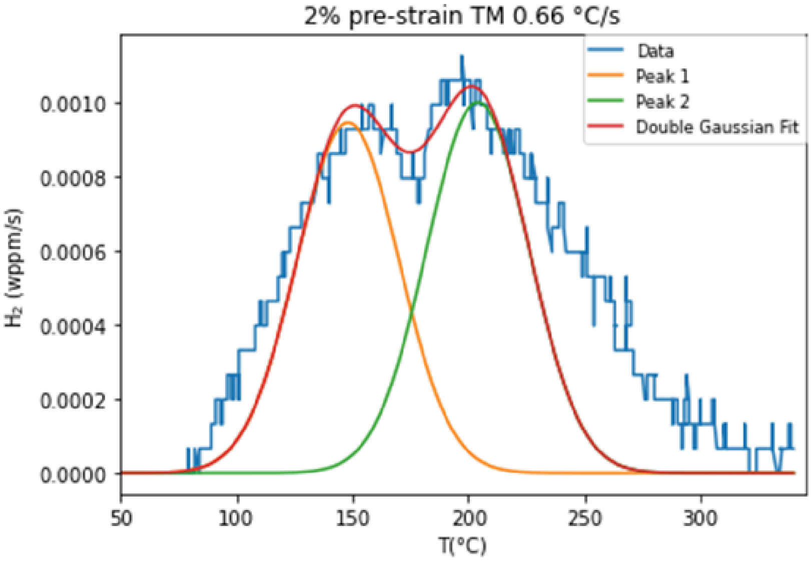

Figure 24: TDS spectra and Double Gaussian data fit of 2% pre-strained TM sample

Fig. 25 depicts the result of both fitting methods for the 2 % pre-strained TM samples that will be taken into account to determine binding energies with the Choo-Lee plot.

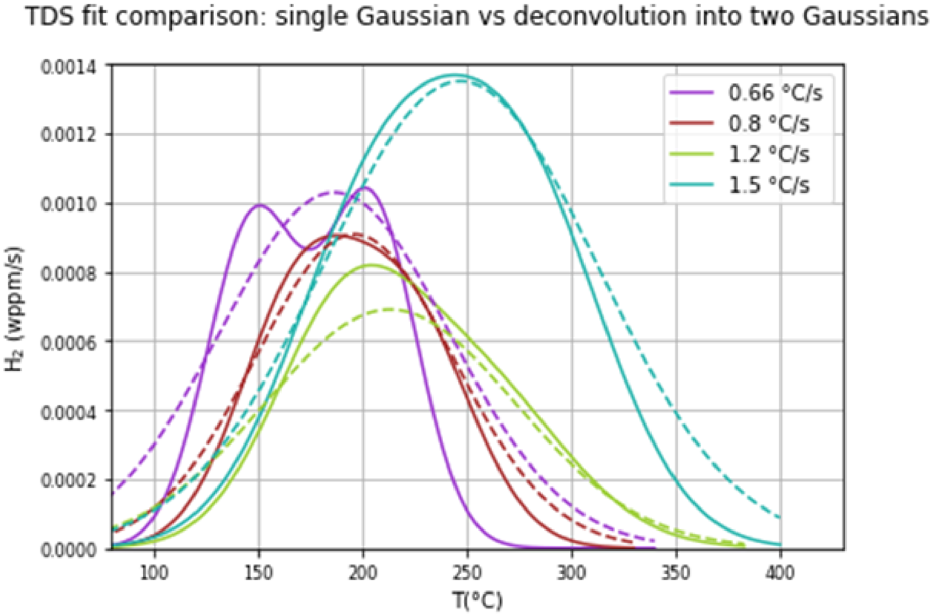

Figure 25: TDS data fit of 2% pre-strained TM samples by both fitting methods. The discontinuous line is for the single Gaussian fit and the continuous one for the sum of the two deconvoluted peaks

The results of applying the Kissinger's theory to the filtered hydrogen concentration peaks are shown in the Choo-Lee plot in Fig. 26. From the slope of the linear regressions the binding energies are calculated and shown in Table 7. The single Gaussian approach gives a slighter higher value to binding energy than Peak 1 and Peak 2. Also, the binding energy values of Peak 1 and 2 are almost identical.

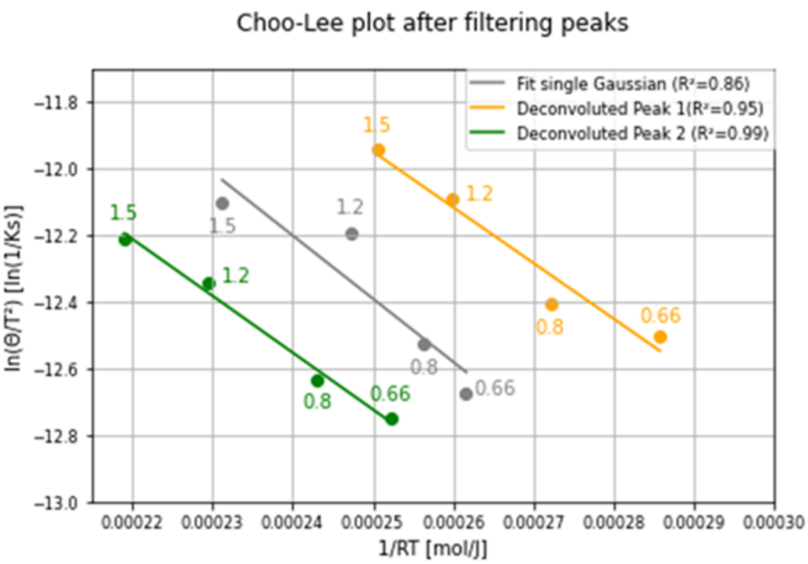

Figure 26: Choo-Lee plot of the 2% TM pre-strained samples

Table 7: Binding energy values for different fits of 2% pre-strained TM samples

Fit	**Binding energy [kJ/mol]**
Single Gaussian	19.0
Peak 1 Double Gaussian	16.7
Peak 2 Double Gaussian	17.0

When looking only to these results, we would say that all the TDS tests are valid due to the low standard deviation of the hydrogen content within the five tests. However, when studying the binding energies, the TDS test performed at heating rates of 1 °C/s weas not taken into account because the location of their peaks was not in accordance with the rest of peaks. On the other hand, since the total hydrogen concentration of the spectra obtained at 1 °C/s is similar to the hydrogen quantity of the rest of the samples, it is taken into account in terms of hydrogen quantity. The average hydrogen concentration, taken from Table8, of the 2%TM pre-strained samples is 0.16 ± 0.040 Hwppm.

Pre-strain (%)	**Charging time (h)**	**Heating rate (°C/s)**	**Total hydrogen (wppm)**
2	3.5	0.66	0.19
2	3.5	0.8	0.16
2	3.5	1	0.21
2	3.5	1.2	0.086
2	3.5	1.5	0.14

Table 8: Overview of the 2 % pre-strained TM samples

4.2.3 Hydrogen trapping in 8% pre-strain TM samples

Six 8% pre-strained TM samples were tested with different heating rates (0.66, 0.8, 1, 1.2 and 1.5 °C/s) in order to determine the binding energy of the traps as well as the amount of hydrogen that these samples could absorb and retain. In Fig. 27 the fit of the TDS tests that have passed the filter and will be taken into account to determine the hydrogen binding energy can be seen.

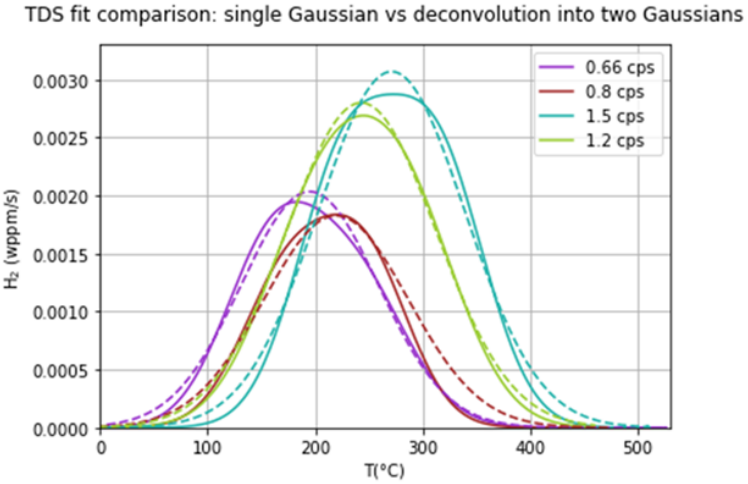

Figure 27: TDS data fit of 8% pre-strained TM samples by both fitting methods. The discontinuous line is for the single Gaussian fit and the continuous one for the sum of the two deconvoluted peaks

The results of applying the Kissinger's theory to the filtered hydrogen concentration peaks are shown in the Choo-Lee plot in Fig. 28. From the slope of the linear regressions the binding energies are calculated and shown in Table 9. In this case, The Peak 1 fit has a lower value of binding energy than Peak 2 fit and single Gaussian fit, which are really similar.

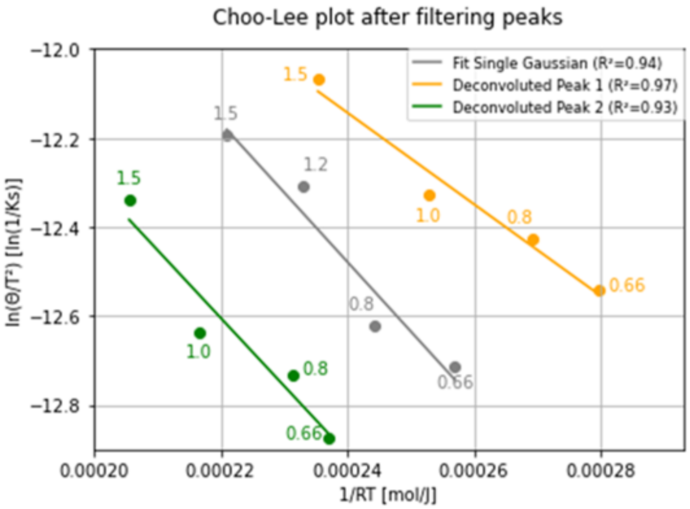

Figure 28: Choo-Lee plot of the 8% TM pre-strained samples

Table 9: Binding energy values for different fits of 8% pre-strained TM samples

Fit	**Binding energy [kJ/mol]**
Single Gaussian	15.6
Peak 1 Double Gaussian	10.3
Peak 2 Double Gaussian	15.3

The average hydrogen concentration of the 8% TM pre-strained samples is 0.38 ± 0.050 Hwppm.Due to the low standard deviation of the hydrogen content within the six tests, none of them would be considered an outlier. The TDS tests performed at heating rates of 1 °C/s and one of the two performed at 0.8 °C/s were not taken into account when calculating the binding energy in order to obtain an accurate result.

Pre-strain (%)	**Charging time (h)**	**Heating rate (°C/s)**	**Total hydrogen (wppm)**
8	3.5	0.66	0.47
8	3.5	0.8	0.31
8	3.5	0.8	0.38
8	3.5	1	0.35
8	3.5	1.2	0.41
8	3.5	1.5	0.36

Table 10: Overview of the 8 % pre-strained TM samples

4.2.4 Hydrogen trapping in 16% pre-strain TM samples

Ten 16% pre-strained TM samples were tested in the TDS with five different heating rates: 0.8, 1, 1.2, 1.5 and 2°C/s (two samples per heating rate).

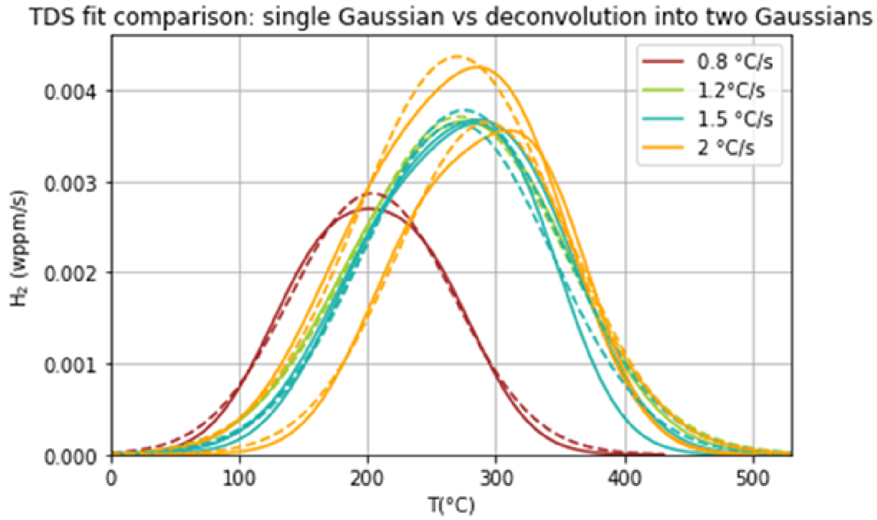

Figure 29: TDS data fit of 16% pre-strained TM samples by both fitting methods. The discontinuous line is for the single Gaussian fit and the continuous one for the sum of the two deconvoluted peaks

Fig. 30 shows the Choo-Lee plot of the 16% pre-strained samples, where it can be observed that the linear regressions are less accurate than in the case of 2% and 8% pre-strained TM samples. The binding energies are calculated and shown in Table 11. In this case, The binding energy of Peak 1 is half of the one of Peak 2 fit and single Gaussian fit, which are almost identical.

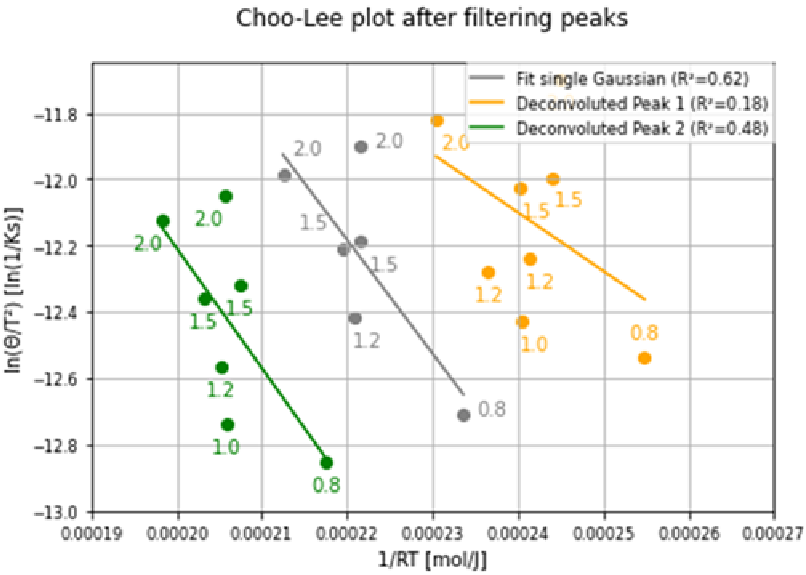

Figure 30: Choo-Lee plot of the TM samples pre-strained 16%

Table 11: Binding energy values for different fits of TM samples pre-strained 16%

Fit	**Binding energy [kJ/mol]**
Single Gaussian	34.2
Peak 1 Double Gaussian	17.6
Peak 2 Double Gaussian	36.2

The average hydrogen concentration of the 16% TM pre-strained samples is 0.52 ± 0.076 Hwppm, which shows that the results obtained for the hydrogen concentration are accurate and almost identical, the only ones that are lower are the two samples that were heated in the TDS with a rate of 2 °C/s , but they do not represent an outlier when applying the Kissinger theory.

Pre-strain (%)	**Charging time (h)**	**Heating rate (°C/s)**	**Total hydrogen (wppm)**
16	3.5	0.8	0.59 ±0.049
16	3.5	1	0.55 ±0.064
16	3.5	1.2	0.55 ±0.12
16	3.5	1.5	0.52 ±0.049
16	3.5	2	0.37 ±0.057

Table 12: Overview of the 16% pre-strained TM samples

4.2.5 Hydrogen trapping in 8% pre-strain 1050AC samples

To study the hydrogen trapping characteristics of the 1050AC, 8% pre-strained samples, four samples were tested. The TDS heating rates were: 0.8, 1, 1.2 and 1.5 °C/s. In this case, all the samples have passed the filter so all of four are taken into account to calculate the binding energies. Fig. 63 shows the TDS peaks obtained, which then are fitted with the single and double Gaussian fits, as depicted in 31.

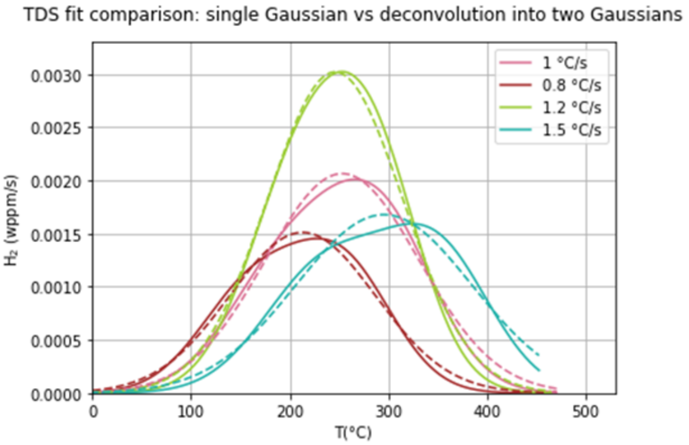

Figure 31: TDS data fit of 8% pre-strained 1050AC samples by both fitting methods. The discontinuous line is for the single Gaussian fit and the continuous one for the sum of the two deconvoluted peaks

Fig. 32 shows the Choo-Lee plot of the 8% pre-strained 1050AC samples. Calculating the slope of the regression line, the binding energies are obtained and shown in Table 13. In this case, as seen in 32, the regression lines present low values of the coefficient of determination R^2, indicating a poor accuracy of the results in this case. This could explain the low values of the binding obtained, that can be consulted in Table 13.

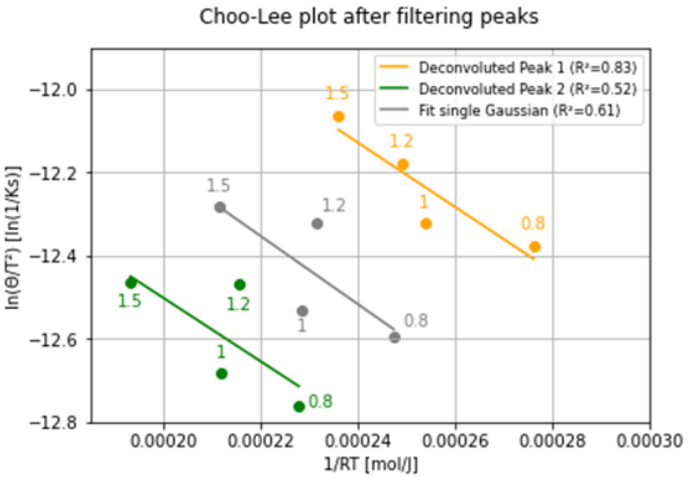

Figure 32: Choo-Lee plot of the 8% pre-strained 1050AC samples

Table 13: Binding energy values for different fits of 8% pre-strained 1050AC samples

Fit	**Binding energy [kJ/mol]**
Single Gaussian	8.2
Peak 1 Double Gaussian	7.7
Peak 2 Double Gaussian	7.6

Regarding the hydrogen concentration, the 8% pre-strained 1050AC samples are able to trap 0.36 ± 0.066 Hwppm. Again, just as in TM samples, because the total hydrogen effused from the samples is similar, with low deviation within the results, all samples tested are taken into account for the total hydrogen concentration.

Pre-strain (%)	**Charging time (h)**	**Heating rate (°C/s)**	**Total hydrogen (wppm)**
8	3.5	0.8	0.34
8	3.5	1	0.40
8	3.5	1.2	0.43
8	3.5	1.5	0.26

Table 14: Overview of the 8 % pre-strained 1050AC samples

4.2.6 Key findings of hydrogen trapping

4.2.6.1 Hydrogen binding energy of traps

As it was pointed by Vandewalle et al. in [14], the binding energy of hydrogen to dislocations depends not only on the position of hydrogen at the dislocation but also on the dislocation type. Even in the same dislocation type there are high variances in the results, as it is shown in [75] and [76]. Both papers study the binding energy of hydrogen in screw dislocations, but the first one gets a value of 25kJ/mol whereas the second gets 43kJ/mol. Other studies give values that range between 26-34 kJ/mol [77], [78], [79].

With the lack of consensum shown in literature, the dynamic character of dislocations, and the high variance of results obtained in this study for the different levels of pre-strain, it is difficult to get a clear conclusion only taking into account the binding energies but not the microstructure features; this will be discussed in Section 4.2.6.3. Moreover, as discussed by Drexler et al., Kissinger's theory is suggested to be applied only in the case of single peaks. In the case of peak overlapping a deeper understanding of the microstructure of the material should be taken into account, as knowing the kind of trapping sites present may help to interprete the TDS data [71].

In Table 15 the binding energies of the two fitting method for each combination of microstructure and pre-strain are shown. The color of the cells changes following the R^2 value of the linear regression obtained in the Choo-Lee plot in this way: for values of R^2 between 0.85 and 1, green is chosen; values of R^2 between 0.5 and 0.65 are shown in orange and values of R^2 below 0.5 are in red.

	TM			**1050AC**
	2%	**8%**	**16%**	**8%**
Single Gaussian	19.0	15.6	34.2	8.2
Peak 1	16.7	10.3	17.6	7.7
Peak 2	17.0	15.3	36.2	7.6

Table 15: Color-coded table depending on the value of the coefficient of determination R^2 of the linear regression

4.2.6.2 Hydrogen concentration

The variation on total hydrogen concentration with increasing levels of pre-strain seems to follow a power law, as shown in Fig. 33 . The power law seems to be close to an asymptote with necking. The standard deviation of the hydrogen concentration grows with pre-strain. So, in terms of wppm, as pre strain increases the results are less reliable.

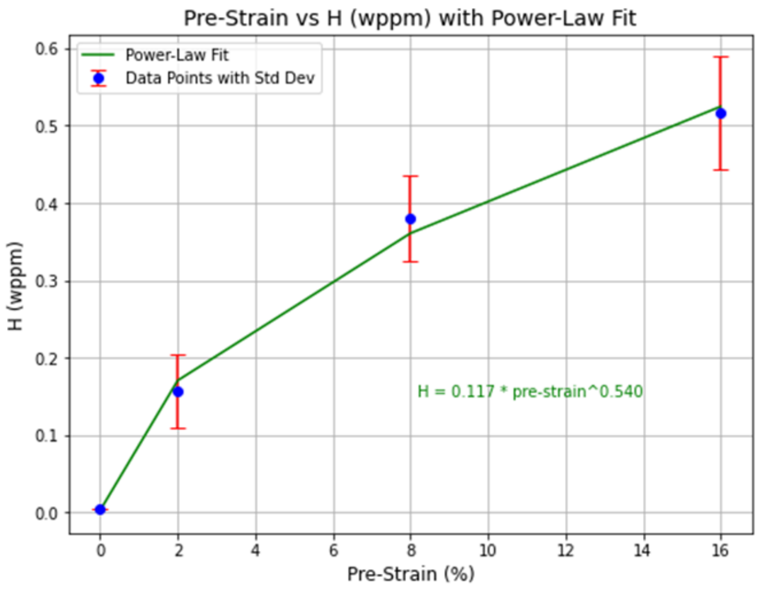

Figure 33: Evolution of hydrogen concentration with increasing pre-strain for TM samples

To be able to discuss the effect of pre-strain hydrogen trapping, dislocation density was studied applying the USDM method to XRD spectra, as discussed previously. As seen in Fig. 34, no effect of pre-strain is observed in the diffraction peaks, since there is no broadening when comparing the 0% TM sample to the 8% TM sample (close ups of the XRD spectra can be found in the Annex D). Consequently, the dislocation density was not calculated, since its value from the USDM method depends on the peak width. As there is no peak broadening, no increase in the dislocation density will be obtained.

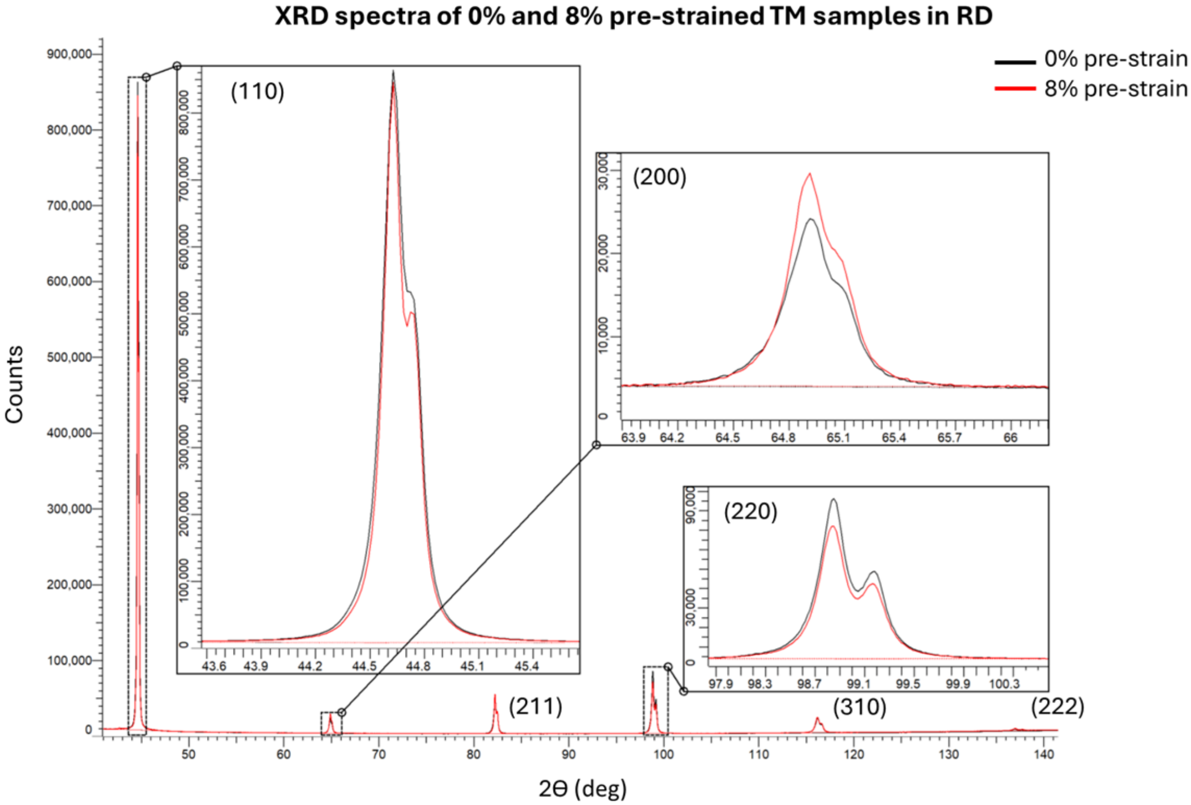

Figure 34: XRD spectra of 0 and 8 % pre-strain TM samples

The absense of peak broadening in the XRD peaks for the 8% pre-strained TM sample could be attributed to the sensitivity of the XRD towards the statistically stored dislocations (SSDs) rather than to geometrically necessary dislocations (GNDs), as explained by Gallet et al. in [48] and exemplified in Fig. 35. XRD assumes the presence of crystallite domains and measures dislocations within them. Consequently, dislocations near or at grain boundaries and thsoe grouped in cells are not taken into account.

Moreover, Sidor et al. observed a saturation when studying a cold-rolled aluminum alloy with XRD due to the equilibrium between dislocation multiplication and annihilation in [80], so this can also be the reason why there's no peak broadening in our case. This hypothesis does not match with the fact that, according to TDS results, the hydrogen quantity increases with pre-strain, as seen previously in Fig. 33

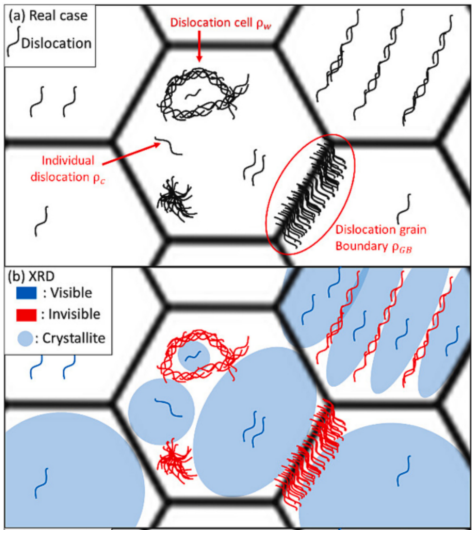

Figure 35: Representation of (a) different types of dislocations present in the microstructure and (b) the ones that XRD can discern [48]

Zheng et al. studied with XRD and TEM how different microstructures in an eutectoid steel affect its strain-hardening behavior [81]. They concluded that, at 0.7% strain (yield point region), high number of GNDs are formed in the ferrite-cementite interfaces. At 4% strain, the GND density keeps increasing near cementite particles and SSDs start appearing inside of ferrite. At 10% pre-strain there are more GNDs in the interface between ferrite and cementite and SSDs keeps growing in ferrite as well; apart from that, dynamic recovery is observed. This article concluded that GND increase in number as the cementite particles are more closely spaced, and SSD density decreases with smaller particle size.

Taking these studies' findings to our case, it makes sense to see no peak broadening with increasing pre-strain level, mainly due to:

- XRD only studies SSDs, not GNDs.
- Our sample has small grains, so SSD density could not vary significantly between both samples.
- 8% pre-strained sample can be in the recovery range.
- The main number of dislocations could be in the interface pearlite-ferrite as GNDs, so they wouldn't be seen by the XRD.

4.2.6.3 Effect of microstructure on hydrogen trapping

To understand the effect of the microstructure on hydrogen trapping of S355ML, comparing the 8% pre-strained 1050AC samples to the 8% pre-strained TM samples is needed. Regarding the hydrogen content, no significant difference is observed between both sample groups. This could imply that, for S355ML, microstructure does not play a significant role in hydrogen trapping, being the dislocations the main contribution to it. the other hand, the binding energies obtained for the 8% TM samples double the ones obtained for 1050AC samples. However, as previously mentioned, the binding energies obtained for the 1050AC samples are not accurate, since they are based on a linear regression with low R^2 values, as seen in Table 15. Moreover, as it was explained in [71], even high values of R^2 do not guarantee that the TDS analysis is trustworthy; is in this same article where it was stated that a comprehensive understanding of how the different microstructural features interact with hydrogen is needed in order to perform a correct interpretation of the results. In this case, the available results are not enough to conclude the effect of microstructure in hydrogen trapping for S355ML.

There is not much data of the role of bainite on hydrogen trapping in literature but Park et al. concluded that increasing the bainite content in a ferritic steel, hydrogen diffusivity decreased [82]. However, when looking at Fig. 22, it can be seen that the vast majority of the 1050AC microstructura is composed of ferrite. Therefore, bainite is not expected to influence the hydrogen diffusivity in this case.

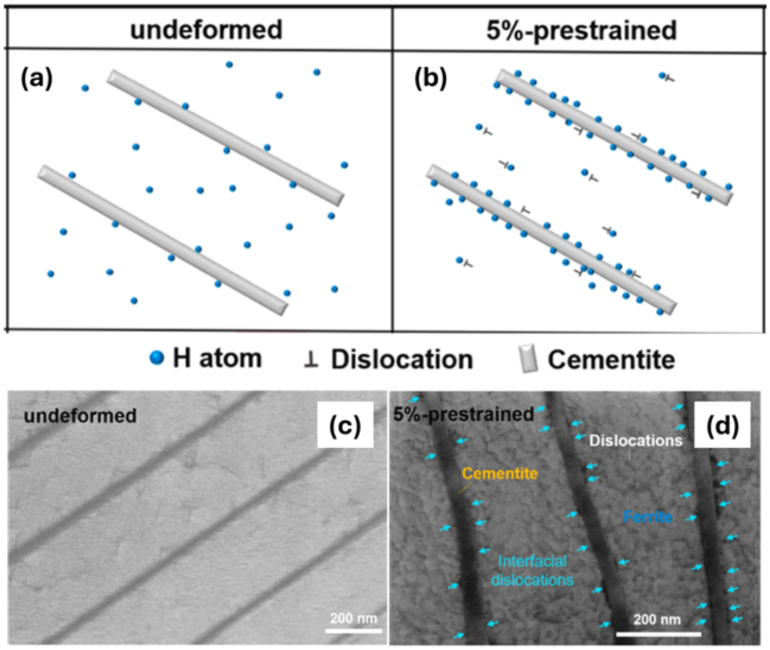

Figure 36: Schematic representation of hydrogen distribution (a) without deformation, (b) with 5% pre-strain. (c) and (d) are TEM images showing dislocation distribution in the undeformed and 5% pre-strained sample, respectively [83]

It can be argued that the pearlitic-ferritic interface could be a trapping site. However, based on the almost identical hydrogen concentration on the 8% pre-strained samples (TM and 1050AC) and on the fact that at 0% pre-strain in TM samples did not retain any hydrogen, the most likely scenario is that the main traps are the dislocations induced by the pre-strain. Zhang et al. studied the effect of pre-strain in the hydrogen trapping capabilities of a pearlitic steel and proved that when pre-strain is applied, there is an increase of dislocations in the ferrite-cementite interface, as seen in Fig. 36. These dislocations will be primarily GNDs since they are not randomly distributed and they appear to accommodate the strain mismatch between ferrite and pearlite during the deformation caused by the pre-strain. This alligns with the discussion in Section 4.2.6.2, where the increase of GNDs over SSDs was considered to be one of the possible reasons why there was no peak broadening in the XRD analysis. On the other hand, the binding energy attributed to dislocations in the (incoherent) ferrite-cementite interface of that study is 40 kJ/mol, much higher than the ones obtained for the S355ML in this project. However, in the same paper it is mentioned as well that the coherent ferrite-cementite phases have a calculated binding energy of 17 kJ/mol, so maybe in the case of S355ML the ferrite-cementite interface was coherent for 2% and 8% pre-strained samples and incoherent for the 16% pre-strain. This could explain the great difference between the binding energies obtained for 2% and 8% pre-strained samples with respect to the 16% pre-strained ones.

4.3 Effect of hydrogen on mechanical properties

To study the effect of hydrogen on mechanical properties, ex-situ SSRT and PIP tests have been carried out. With the SSRT an effect of the pre-strain rate and the HE behavior of TM samples pre-strained 8% wants to be studied after having been charged for 2 hours. The amount of hydrogen in this samples is taken to be around 0.6 wppm H, as the TDS samples show in Fig. 46.

PIP test were performed in order to study a possible variation in tensile properties after charging the samples for 2 hours time as a consequence of hydrogen effusion at room temperature. The results of the PIP tests will be compared to the ones of the ex situ SSRT.

4.3.1 Effect of strain-rate on HE: Ex-situ SSRT

One 0% pre-strained TM, uncharged sample (SSRT1) and six 8% pre-strained TM samples (SSRT2-SSRT7) charged for two hours were subjected to SSRT to failure. The results of the SSRT are summarized in the Table 16 and in the Fig. 37. After failure, one half of the sample was tested in TDS to see if there was some hydrogen left inside it (results in Fig. 46) and the other fractography surface was inspected in the SEM.

Sample Code	Pre-strain (%)	Charging time (h)	**Cross Head Displacement rate (mm/min)**	**UTS (MPa)**	**Strain at necking (%)**	**Elongation at failure (%)**
SSRT1	0	0	1.00	532.88	20.65	35
SSRT2, SSRT3	8	2	2.70	531.87 ±2.98	12.99 ±$5E-03$	28 ±1
SSRT4	8	2	0.46	525.68	14.20	25
SSRT5, SSRT6, SSRT7	8	2	0.11	517.68 ±0.11	11.4 ±2.13	22 ±2.45

Table 16: SSRT results

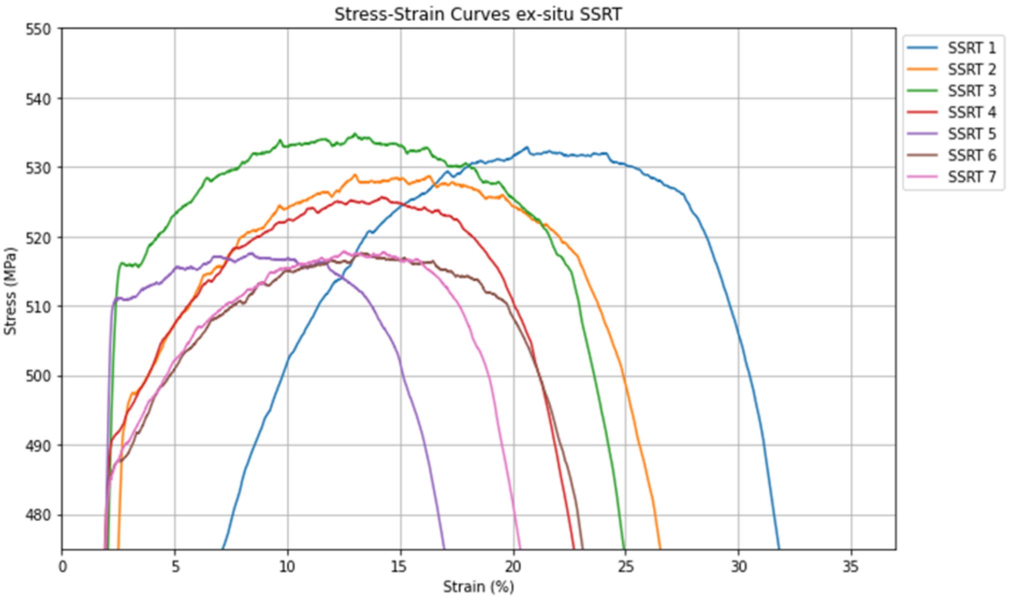

Figure 37: Stress-strain curves of the samples subjected to ex-situ SSRT

4.3.1.1 Signs of HE in fractography

Only the samples with HE signs in their fractography are shown in this section. Fig.38 is the uncharged, not pre-strained sample, so it shows how fractography would look like without hydrogen embrittlement. In Fig. 38 only voids are observed. Out of the six hydrogen charged samples, only three show signs of quasi-cleavage: SSRT2 (Fig. 39), SSRT3 (Fig. 40) and SSRT7 (Fig. 41).

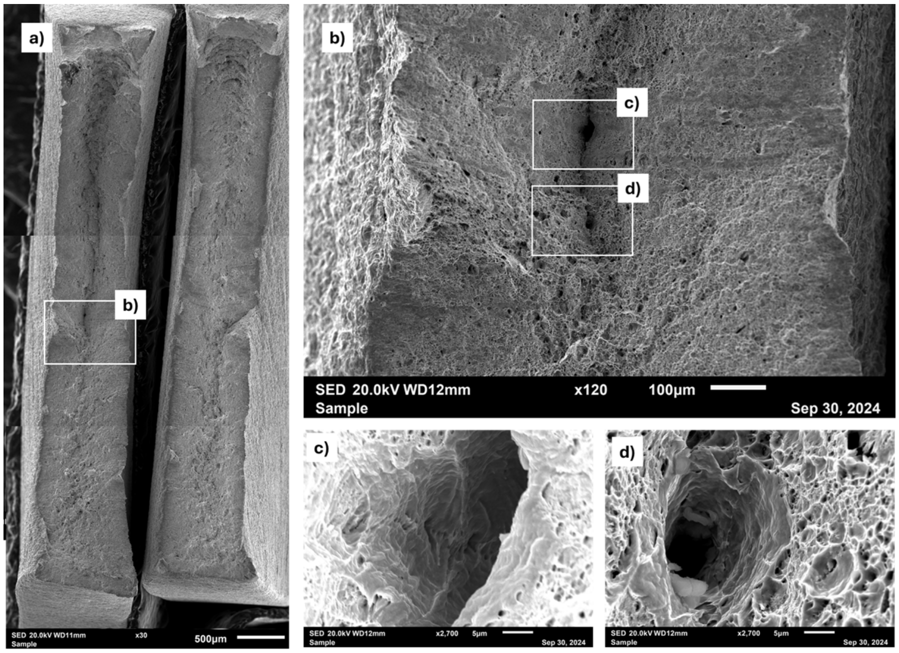

Figure 38: Fractography of SSRT1 sample. (a) shows the overview of the fractographic surface. (b), (c) and (d) present some details of the fractography

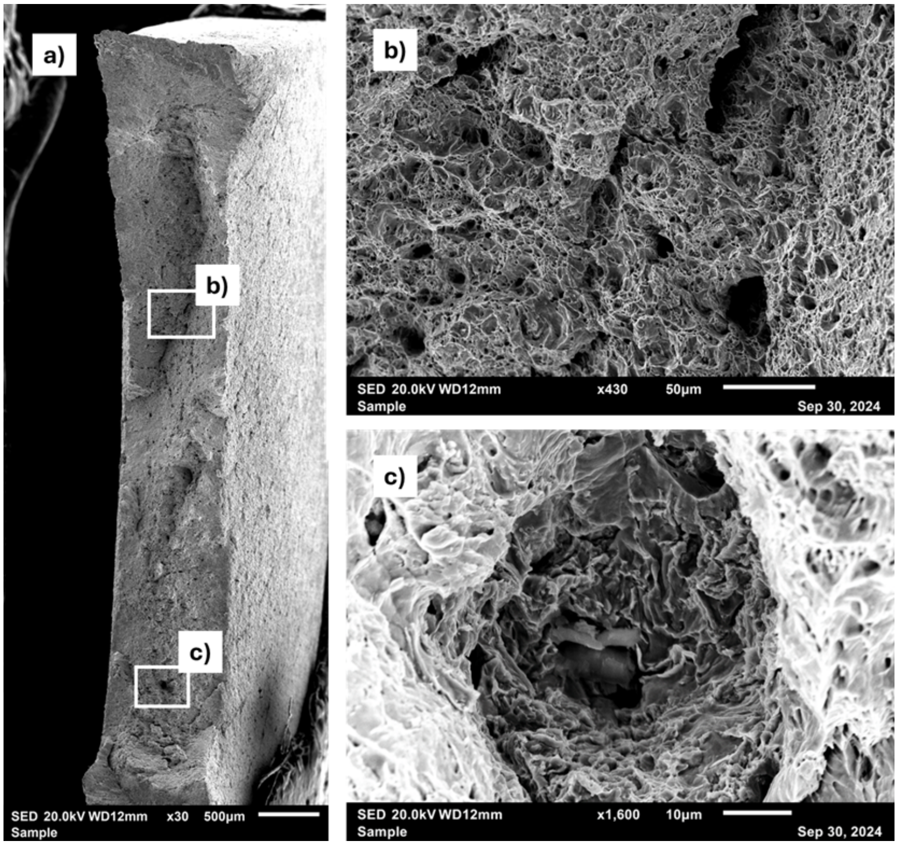

Figure 39: Fractography of SSRT2 sample. (a) shows the overview of the fractographic surface. (b) and (c) present some details of the fractography

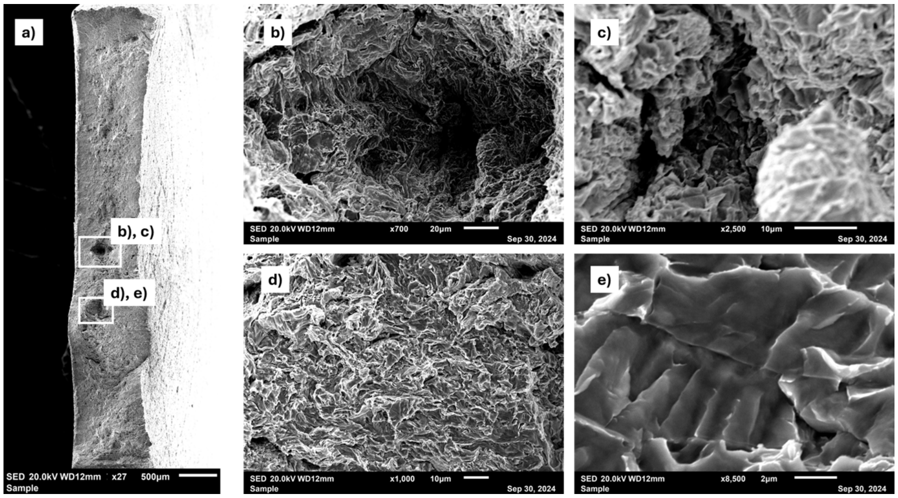

Figure 40: Fractography of SSRT3 sample. (a) shows the overview of the fractographic surface. (b), (c), (d) and (e) present some details of the fractography

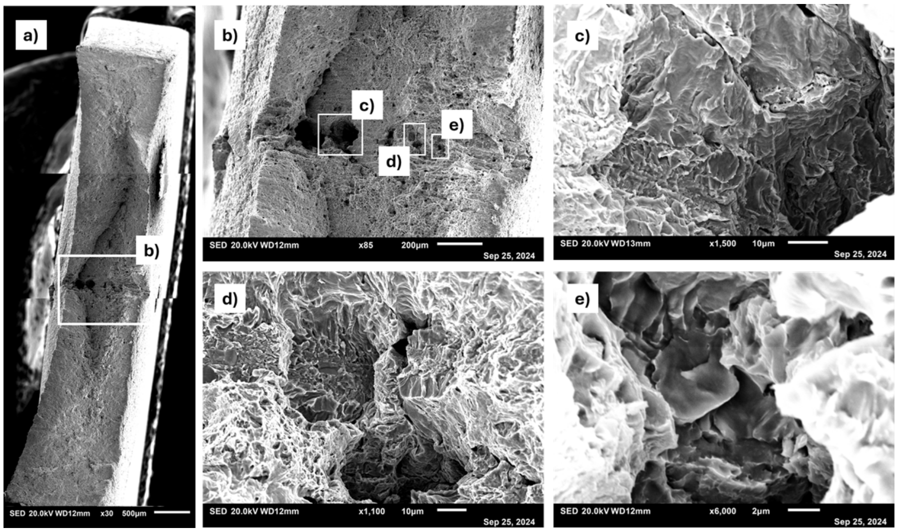

Figure 41: Fractography of SSRT7 sample. (a) shows the overview of the fractographic surface. (b), (c), (d) and (e) present some details of the fractography

4.3.1.2 Hydrogen Embrittlement Index (HEI)

The HEI is usually taken as a way to quantify hydrogen embrittlement. The HEI was calculated following the following steps:

1. The fractography surface area of all the samples subjected to SSRT was measured with SEM following the procedure explained in Section 3.2.6.1.
2. The area reduction with respect to the cross-sectional area of the SSRT sample in the gauge section 20 (mm^2) was calculated following the Eq. 13.

$$AR = \frac{A_0 - A_f}{A_0} \times 100 \tag{13}$$

   where:

   $A_0 = 20\ mm^2$

   A_f = Area after SSRT

3. The HEI was calculated with Eq. 14

$$HEI = \frac{AR_H - AR_{Ref}}{AR_{Ref}} \times 100 \tag{14}$$

   where:

   AR_H = Area reduction of the samples that have been charged with hydrogen (%)

   AR_{Ref} = Area reduction of the reference sample: SSRT1, uncharged sample (%)

Table 17 shows the different values of area reduction and HEI for the SSRT samples subjected to hydrogen. As it can be seen, there is some loss in the area reduction, which means that ductility has decreased with respect to sample SSRT1, the uncharged one. However, no clear trend it is observed with decreasing crosshead displacement rate, since HEI is 7.84 ± 2.15% for samples subjected to cross-head displacement of 2.70 mm/min,2.51% for the sample strained at cross-head displacement of 0.46 mm/min and 8.54 ± 4.29% for the samples strained at cross-head displacement of 0.11 mm/min.

Sample Code	**Area after SSRT (mm^2)**	**Area reduction (%)**	**HEI (%)**
SSRT1	4.89	75.55	-
SSRT2, SSRT3	6.07 ±0.32	69.63 ±1.63	7.84 ±2.15
SSRT4	5.27	73.65	2.51
SSRT5, SSRT6, SSRT7	6.18 ±0.65	69.1 ±6.24	8.54 ±4.29

Table 17: Fractographic surface area of the samples subjected to SSRT and HEI with respect to the $20mm^2$ initial crossectional area of the sample's gauge

4.3.2 Effect of hydrogen diffusion on tensile properties: PIP tests

PIP tests were performed for two reasons: the first one is to maximize the number of available samples (since at least four PIP samples were obtained from the gauge of one 8% pre-strained SSRT sample) to determine the mechanical properties; the second reason was to study if it was possible to study the effect of hydrogen effusion with time in mech properties, since the conventional SSRT were performed ex-situ.

4.3.2.1 Effect of hydrogen diffusion on UTS

The change in UTS with respect to the uncharged, 0% pre-strain sample is due to the strain hardening that was introduced with the 8% pre-strain, but not due to HE of the material, since there is no difference between the 8% pre-strained TM samples that have been charged for two hours to the uncharged ones, as Fig. 42 shows. This is consistent with the SSRT results, since it was shown that the presence of hydrogen did not vary the UTS.

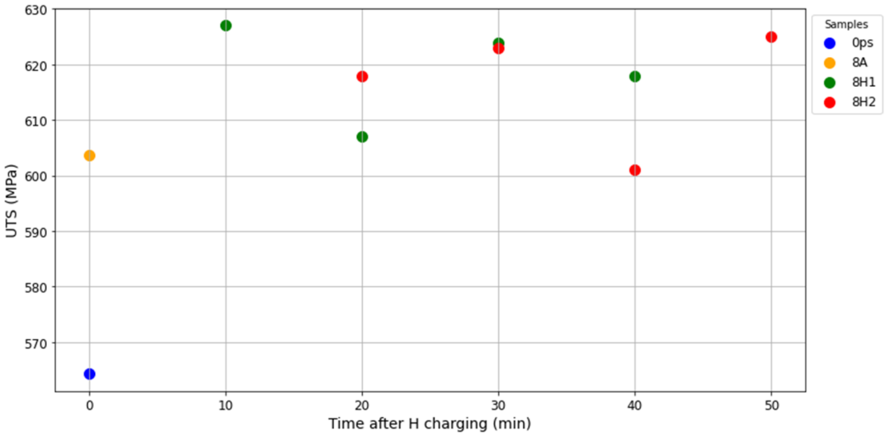

Figure 42: Variation and evolution of UTS with pre-strain and time in atmosphere after charging

4.3.2.2 Effect of hydrogen diffusion on Yield strength

The Yield strength increases with respecto to the 0% pre-strain TM sample as a consequence of the 8% pre-strain applied to samples 8A, 8H1 and 8H2. Hydrogen does not seem to play a role, as it can be seen in Fig. 43. This result complies with the data available in the literature and with the SSRT results of this thesis, where it is shown that hydrogen does not have an effect on yield strength.

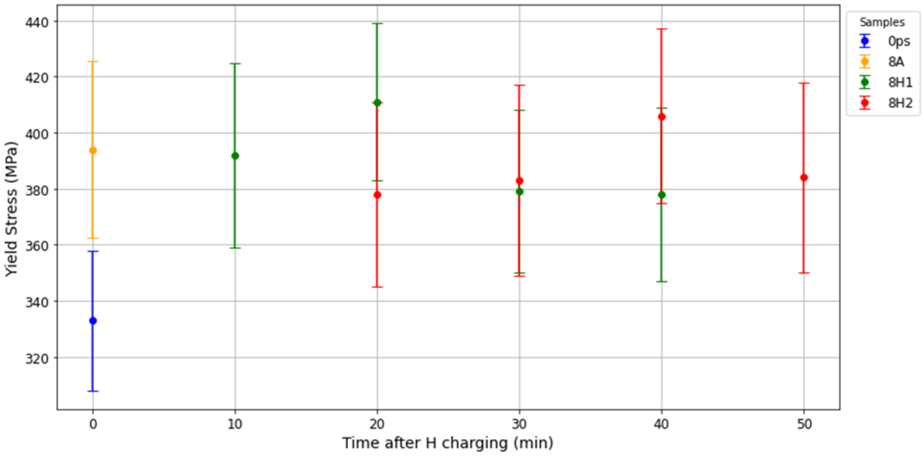

Figure 43: Variation and evolution of yield strength with pre-strain and time in atmosphere after charging

4.3.2.3 Effect of hydrogen diffusion on necking

The effect of pre-strain and hydrogen are not observed in the strain at which necking takes place, as it is depicted in Fig. 44. Within the same sample it is observed a 2% strain at necking variation, so PIP tests do not show a difference in necking that is distinguishable.

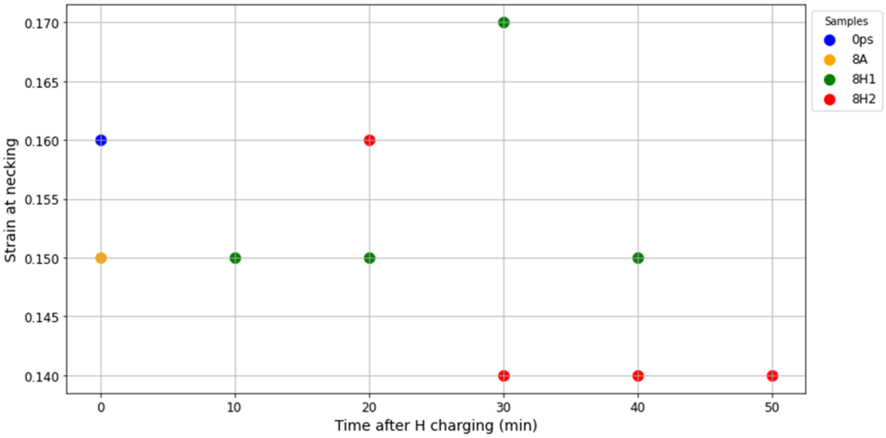

Figure 44: Variation and evolution of necking point with pre-strain and time in atmosphere after charging

4.3.2.4 Effect of hydrogen diffusion on hardness

According to Fig. 45, the increase in hardness is due solely to the strain hardening effect induced by the pre-strain.

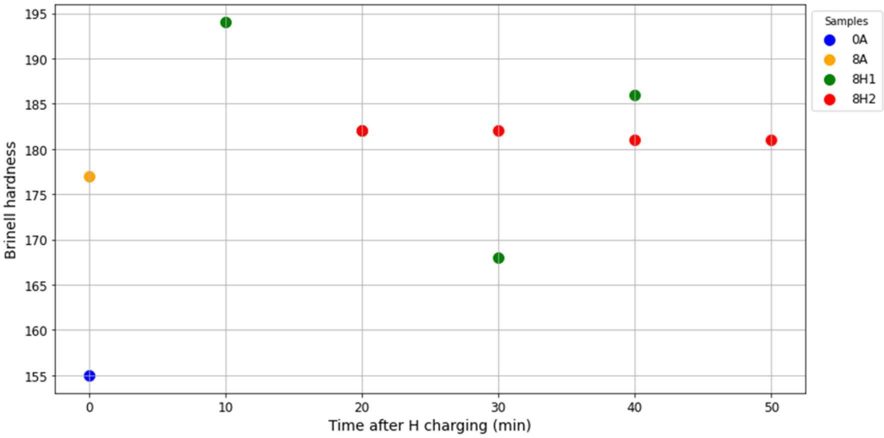

Figure 45: Variation and evolution of hardness with pre-strain and time in atmosphere after charging

4.3.3 Effect of stress on hydrogen diffusion

TDS samples were charged under the same conditions as SSRT and PIP samples and then they were let to rest in the atmosphere, at ambient temperature, before performing the TDS to compare the hydrogen effusion behavior when subjected to different stress conditions (tensile stress for SSRT, indentation for PIP, and no stress for TDS samples). From Fig. 46 it can be deduced that, when no stress is applied in the samples, although hydrogen concentration within the sample decreases with time, hydrogen effusion is slower than in PIP and SSRT cases.

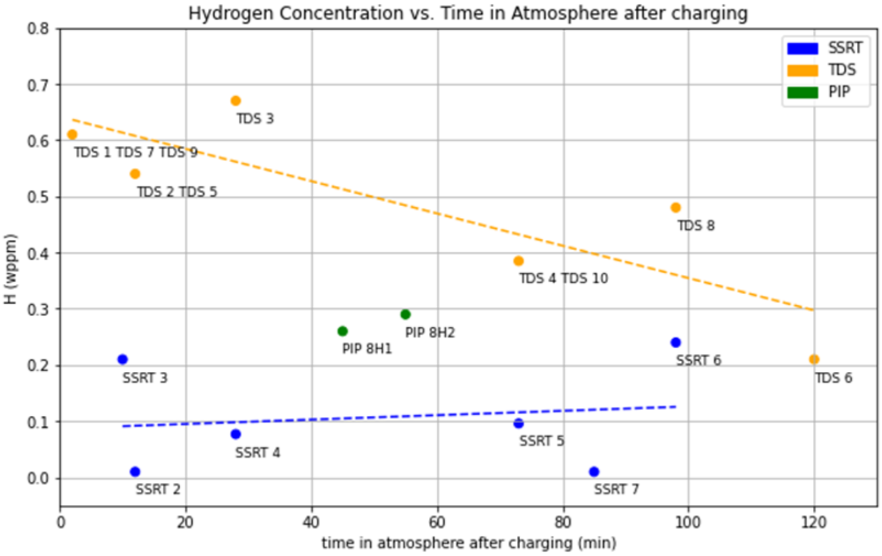

Figure 46: Effect of stress on hydrogen diffusion for TDS non-stressed samples, PIP samples and SSRT samples

4.3.4 Key Findings of Effect of Hydrogen on Mechanical Properties

4.3.4.1 Discussion on the effect of hydrogen in ex-situ SSRT

Only three samples show QC: SSRT2, SSRT3 and SSRT7. However, all the hydrogen pre-charged samples show a lower area reduction with respect to the uncharged sample, which means that the charged samples present lower ductility than the uncharged one. The fact that not all the hydrogen charged samples show embrittled fractographic features can be explained with the concept "critical hydrogen concentration", which makes reference to the hydrogen concentration threshold above which decohesion takes place. It can be the case that the hydrogen concentration in the material is not high enough, or the hydrogen could be well distributed along the ferrite-cementite interface, preventing its local accumulation and thus not causing quasi-cleavage.

Since HE is observed by a reduction of toughness and ductility, it could be stated that all the hydrogen charged samples are embrittled. However, only one uncharged sample has been tested, so the accuracy of this result is not known (it could be that, when testing more uncharged non pre-strained samples, the mechanical parameters greatly differ from one test to the other). Moreover, a clear trend of HEI with crosshead displacement rate is not observed for the charged samples, presenting high spread of the HEI values for the ones strained at 0.11 mm/min (SSRT5, SSRT6 and SSRT7).

However, when looking at Table 16 it's clear that hydrogen has an effect on the mechanical behavior of S355ML steel:

- The UTS values of the SSRT samples, they follow a decreasing trend with lower crosshead displacement rates.
- Strain at necking of the pre-charged samples decreases with respect to the uncharged one, but their values are similar within the hydrogen charged samples.
- Elongation at failure decreases with lower crosshead displacement rates. It makes sense that the slower the strain rate, the greater the embrittlement experienced, since hydrogen diffusion throughout the metal is time-dependent. As a consequence, for lower strain rates, the hydrogen is able to diffuse and concentrate in the areas which are experiencing higher stresses.

This discrepancies between the variation of mechanical properties with hydrogen presence and lack of trend in the HEI of SEM analyses can be due to the fact that, as seen in Fig. 47, the fractographic surface of the SSRT samples is not flat. Consequently, the 2D area measurements made by SEM are not a reliable method to measure the HEI.

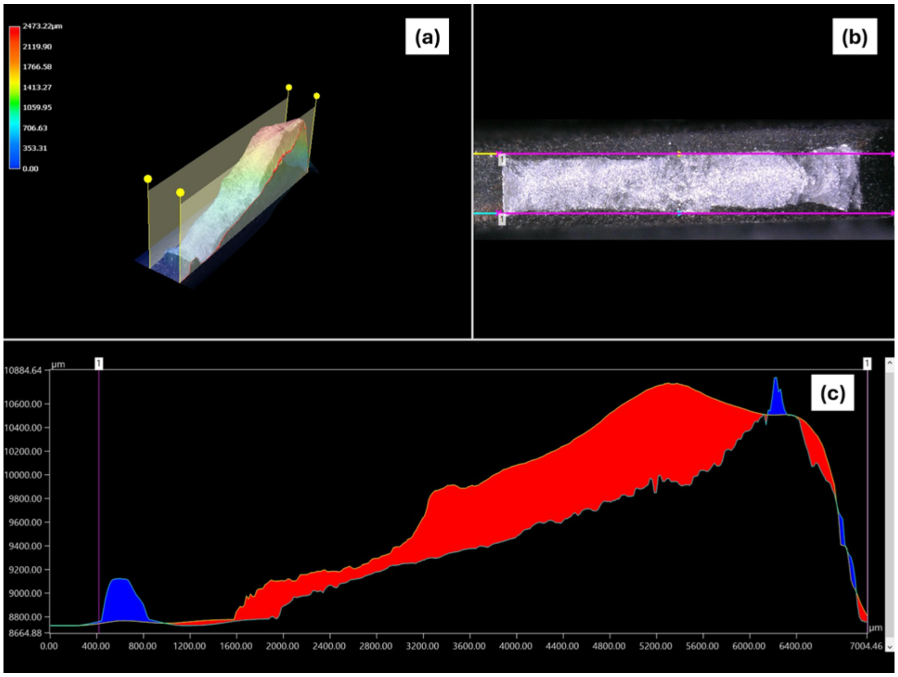

Figure 47: Keyence's images of SSRT4 sample which show: (a) 3D image of the fractography surface, (b) 2D projection of the fractographic surface and (c) profilometric profile

4.3.4.2 Suitability of PIP tests to study HE

PIP results are consistent among the different indentations but they show that is not an effective method to study HE. Al thought HE does not affect yield strength nor UTS, it does decrease ductility, and PIP results do not show any sign of embrittlement. Moreover, although there's an increase in the yield strength and in the UTS in the pre-strained samples with respect to the non pre-strained ones, the relative variation does not match with the ones observed in conventional SSRT:

- Yield Strength: SSRT samples with 8% pre-strain that have been charged experience an increase of 9% in yield strength with respect to uncharged, 0% pre-strain sample. The yield strength increase in 8% pre-strained samples is almost identical for charged (17%) to uncharged (18%) samples when compared to the non charged, 0% pre-strain sample. This indicates that the increase in yield strength in the case of PIP is due to the strain hardening effect, the hydrogen does not play any roll. 8% pre-strain uncharged samples should be tested in SSRT to compare to which extent the variation in props is due to the effect of hydrogen to the effect of strain hardening.
- Ultimate Tensile Strength (UTS): in SSRT samples a decrease of UTS is observed in the 8% pre-strain samples when comparing them to the 0% pre-strain sample. In the 8% pre-strain precharged samples, UTS decreases with decreasing strain rate.
- Strain at necking: No effect of hydrogen nor of pre-strain is seen in these values.
- Hardness: No effect of hydrogen is seen in the hardness values, being the strain hardening induced by the pre-strain the responsible for an increase in hardness from the 0% to the 8% samples.

5 Conclusions

1. S355ML does not trap hydrogen without applied tensile pre-strain.
2. Hydrogen concentration is consistent and increases with pre-strain following the power law $H = 0.12\epsilon^{0.54}$.
3. XRD did not show any differences between the 0% and the 8% pre-strained TM samples, most likely because this method does not take into account the GNDs. As a consequence, no dislocation density could be calculated to be compared to the power law that defines hydrogen concentration variation with pre-strain.
4. A good stud weld replication of the CGHAZ of S355ML was obtained by heating up the TM samples in an oven at 1050 °C for one hour and then air cooled.
5. The dislocations induced by pre-strain seem to be the main traps present in TM and 1050AC samples.
6. In TM samples the dislocations are likely GNDs and are located in the ferrite-cementite interface.
7. The 8% pre-strained samples of TM and 1050AC microstructures present almost identical hydrogen concentrations when following the same preparation and charging method: 0.38 wppm H for the TM sample and 0.36 wppm sample for the 1050AC samples.
8. The hydrogen binding energies for the 2%, 8% and 16% pre-strained TM samples vary within different levels of pre-strain and the reliability of the results decreases when increasing the pre-strain. For the Single Gaussian fit method, the 2% pre-strained TM samples have a binding energy of 19 kJ/mol, 15.6 kJ/mol for the 8% pre-strained TM samples and 34.2 kJ/mol for the 16% pre-strained TM samples. This increase in binding energy for the 16% pre-strain can be due to a change in the ferrite-cementite interface, from coherent to incoherent to accommodate increasing levels of pre-strain.
9. 8% pre-strained TM samples present binding energies that double the values of 8% pre-strained 1050AC samples, but the lower reliability the binding energies for the 1050AC samples makes difficult to investigate the reason why such a difference in binding energy takes place.
10. The results obtained by making use of the Kissinger equation and the Choo-Lee plot present high variability even for the same combination of pre-strain and microstructure. The dispersion in the results increases with pre-strain, with R^2 values of less than 0.5 for the case of 16% pre-strain.
11. The filtering method applied to select the data points that should be used to calculate the binding energies seems to work, since it increases the R^2 values of the linear regression from the Choo-Lee plot.
12. Overall, it seems difficult to determine which TDS tests should be treated as outliers, since tests that can be used to calculate the hydrogen concentration in a sample are discarded when calculating the binding energies. The hydrogen concentration is determined by the area below the curve, and the binding energies are calculated using the temperature at which the maximum hydrogen effusion takes place (T_{max}.
13. The presence of yield point and the fact that the onset of necking happens at around 15% strain

in S355ML may add unwanted variables when studying the binding energy of dislocations of 2% and 16% pre-strain.

14. PIP test are not suitable to study HE phenomena of S355ML because strain rate plays an important role in HE.
15. The ex-situ SSRT cause hydrogen embrittmeent in 8% pre-strained TM samples. The embrittlement is shown in the decrease of elongation at failure up to 37% and in the presence of quasi-cleavage in fractographic surfaces.

6 Recommendations

Since the 2% strain falls into the yield point region and the 16% strain is the onset of necking, more samples in the strain hardening region (as the ones of 8%) should be tested when studying the hydrogen binding energy, hydrogen concentration and effect of hydrogen on mechanical properties.

To further investigate the effect of microstructure in HE behavior of S355ML and compare it to the TM samples, more pre-strain levels in the 1050AC samples should be applied. By doing this, the effect of residual stresses caused by welding in the monopile manufacture would be studied as well.

Use other characterization methods, such as EBSD or TEM, together with XRD to study the dislocation density evolution with pre-strain of S355ML samples. This way, it could be possible to determine if the proposed hypothesis given about the dislocations being mainly of GNDs and located mainly in the grain boundaries and in the ferrite-cementite interface is true.

Althought a good reproduction of stud weld microstructure of S355ML was obtained with the heat treatment performed, further research should involve making use of a Gleeble to analyze if it is a good representation of the HAZ caused by the welding that takes place in the monopile manufacturing.

More samples should be used to determine the spread and accuracy of results when applying the Kissinger equation and the Choo-Lee plot.

Permeation experiments in TM and 1050AC microstructures with increasing levels of pre-strain would provide useful knowledge to further understand the effect of pre-strain and microstructure in hydrogen capture and hydrogen embrittlement of S355ML.

In situ SSRT should be performed and a higher number of samples should be tested.

In situ hydrogen charging fatigue tests should be carried out to S355ML since it would reproduce better the in-service conditions.

References

[1] M. Bilgili, A. Yasar, and E. Simsek. “Offshore wind power development in Europe and its comparison with onshore counterpart”. In: *Renewable and Sustainable Energy Reviews* 15.2 (2011), pp. 905–915. ISSN: 13640321. DOI: `10.1016/j.rser.2010.11.006`. URL: `http://dx.doi.org/10.1016/j.rser.2010.11.006`.

[2] P. E. Morthorst and L. Kitzing. “Economics of building and operating offshore wind farms”. In: *Offshore Wind Farms: Technologies, Design and Operation*. Elsevier Ltd, 2016, pp. 9–27. ISBN: 9780081007808. DOI: `10.1016/B978-0-08-100779-2.00002-7`. URL: `http://dx.doi.org/10.1016/B978-0-08-100779-2.00002-7`.

[3] T. Stehly et al. “2017 Cost of Wind Energy Review NREL/TP-6A20-72167”. In: *National Renewable Energy Laboratory* September (2018).

[4] C. Pérez-Collazo, D. Greaves, and G. Iglesias. “A review of combined wave and offshore wind energy”. In: *Renewable and Sustainable Energy Reviews* 42 (2015), pp. 141–153. ISSN: 18790690. DOI: `10.1016/j.rser.2014.09.032`. URL: `http://dx.doi.org/10.1016/j.rser.2014.09.032`.

[5] S. Anandavijayan, A. Mehmanparast, and F. Brennan. “A numerical analysis of the effects of manufacturing processes on material pre-strain in offshore wind monopiles”. In: *Procedia Structural Integrity* 13 (2018), pp. 953–958. ISSN: 24523216. DOI: `10.1016/j.prostr.2018.12.178`. URL: `https://doi.org/10.1016/j.prostr.2018.12.178`.

[6] Seok Ki Jan, Min Su Han, and Seong Jong Kim. “Electrochemical characteristics of stainless steel using impressed current cathodic protection in seawater”. In: *Transactions of Nonferrous Metals Society of China (English Edition)* 19.4 (2009), pp. 930–934. ISSN: 10036326. DOI: `10.1016/S1003-6326(08)60380-5`. URL: `http://dx.doi.org/10.1016/S1003-6326(08)60380-5`.

[7] M.B. Djukic et al. “Hydrogen Embrittlement of Low Carbon Structural Steel”. In: *Procedia Materials Science* 3 (2014), pp. 1167–1172. ISSN: 22118128. DOI: `10.1016/j.mspro.2014.06.190`. URL: `http://dx.doi.org/10.1016/j.mspro.2014.06.190`.

[8] M. B. Djukic et al. “Hydrogen damage of steels: A case study and hydrogen embrittlement model”. In: *Engineering Failure Analysis* 58 (2015), pp. 485–498. ISSN: 13506307. DOI: `10.1016/j.engfailanal.2015.05.017`. URL: `http://dx.doi.org/10.1016/j.engfailanal.2015.05.017`.

[9] Alfons H.M. Krom and A. D. Bakker. “Hydrogen trapping models in steel”. In: *Metallurgical and Materials Transactions B: Process Metallurgy and Materials Processing Science* 31.6 (2000), pp. 1475–1482. ISSN: 10735615. DOI: `10.1007/s11663-000-0032-0`.

[10] M. Dadfarnia, P. Sofronis, and T. Neeraj. “Hydrogen interaction with multiple traps: Can it be used to mitigate embrittlement?” In: *International Journal of Hydrogen Energy* 36.16 (2011), pp. 10141–10148. ISSN: 03603199. DOI: `10.1016/j.ijhydene.2011.05.027`. URL: `http://dx.doi.org/10.1016/j.ijhydene.2011.05.027`.

[11] P. Castaño Rivera, V. P. Ramunni, and P. Bruzzoni. “Hydrogen trapping in an API 5L X60 steel”. In: *Corrosion Science* 54.1 (2012), pp. 106–118. ISSN: 0010938X. DOI: `10.1016/j.corsci.2011.09.008`.

[12] Yakai Zhao et al. “The role of hydrogen in hardening/softening steel: Influence of the charging process”. In: *Scripta Materialia* 107 (Oct. 2015), pp. 46–49. ISSN: 13596462. DOI: `10.1016/j.scriptamat.2015.05.017`.

[13] Alan Turnbull. *Hydrogen diffusion and trapping in metals*. Woodhead Publishing Limited, 2012, pp. 89–128. ISBN: 9780857095367. DOI: `10.1533/9780857095374.1.89`. URL: `http://dx.doi.org/10.1533/9780857095374.1.89`.

[14] Liese Vandewalle et al. “The Potential of the Internal Friction Technique to Evaluate the Role of Vacancies and Dislocations in the Hydrogen Embrittlement of Steels”. In: *Steel Research International* 92.6 (2021), pp. 1–15. ISSN: 1869344X. DOI: `10.1002/srin.202100037`.

[15] M. Loidl et al. “Characterization of hydrogen embrittlement in automotive advanced high strength steels”. In: *Materialwissenschaft und Werkstofftechnik* 42.12 (Dec. 2011), pp. 1105–1110. ISSN: 09335137. DOI: `10.1002/mawe.201100917`.

[16] D. Wang et al. “Investigation of hydrogen embrittlement behavior in X65 pipeline steel under different hydrogen charging conditions”. In: *Materials Science and Engineering: A* 860 (Dec. 2022). ISSN: 09215093. DOI: `10.1016/j.msea.2022.144262`.

[17] Xinfeng Li et al. “Effect of pre-strain on hydrogen embrittlement of high strength steels”. In: *Materials Science and Engineering: A* 616 (Oct. 2014), pp. 116–122. ISSN: 09215093. DOI: `10.1016/j.msea.2014.07.085`.

[18] D. Hardie, E. A. Charles, and A. H. Lopez. “Hydrogen embrittlement of high strength pipeline steels”. In: *Corrosion Science* 48.12 (2006), pp. 4378–4385. ISSN: 0010938X. DOI: `10.1016/j.corsci.2006.02.011`.

[19] Xinfeng Li et al. “Review of Hydrogen Embrittlement in Metals: Hydrogen Diffusion, Hydrogen Characterization, Hydrogen Embrittlement Mechanism and Prevention”. In: *Acta Metallurgica Sinica (English Letters)* 33.6 (2020), pp. 759–773. ISSN: 21941289. DOI: `10.1007/s40195-020-01039-7`. URL: `https://doi.org/10.1007/s40195-020-01039-7`.

[20] A. Laureys et al. “Microstructural characterization of hydrogen induced cracking in TRIP-assisted steel by EBSD”. In: *Materials Characterization* 112 (2016), pp. 169–179. ISSN: 10445803. DOI: `10.1016/j.matchar.2015.12.017`. URL: `http://dx.doi.org/10.1016/j.matchar.2015.12.017`.

[21] Sandeep Kumar Dwivedi and Manish Vishwakarma. “Effect of hydrogen in advanced high strength steel materials”. In: *International Journal of Hydrogen Energy* 44.51 (2019), pp. 28007–28030. ISSN: 03603199. DOI: `10.1016/j.ijhydene.2019.08.149`. URL: `https://doi.org/10.1016/j.ijhydene.2019.08.149`.

[22] H. Vehoff and P. Neumann. “Crack propagation and cleavage initiation in Fe-2.6%-Si single crystals under controlled plastic crack tip opening rate in various gaseous environments”. In: *Acta Metallurgica* 28.3 (1980), pp. 265–272. ISSN: 00016160. DOI: `10.1016/0001-6160(80)90161-3`.

[23] M. L. Martin et al. “Hydrogen-induced intergranular failure in nickel revisited”. In: *Acta Materialia* 60.6-7 (2012), pp. 2739–2745. ISSN: 13596454. DOI: `10.1016/j.actamat.2012.01.040`. URL: `http://dx.doi.org/10.1016/j.actamat.2012.01.040`.

[24] O. Barrera et al. *Understanding and mitigating hydrogen embrittlement of steels: a review of experimental, modelling and design progress from atomistic to continuum*. May 2018. DOI: `10.1007/s10853-017-1978-5`.

[25] P. J. Ferreira, I. M. Robertson, and H. K. Birnbaum. “Hydrogen effects on the interaction between dislocations”. In: *Acta Materialia* 46.5 (1998), pp. 1749–1757. ISSN: 13596454. DOI: `10.1016/S1359-6454(97)00349-2`.

[26] M. L. Martin, I. M. Robertson, and P. Sofronis. “Interpreting hydrogen-induced fracture surfaces in terms of deformation processes: A new approach”. In: *Acta Materialia* 59.9 (2011), pp. 3680–3687. ISSN: 13596454. DOI: `10.1016/j.actamat.2011.03.002`. URL: `http://dx.doi.org/10.1016/j.actamat.2011.03.002`.

[27] T. Neeraj, R. Srinivasan, and Ju Li. “Hydrogen embrittlement of ferritic steels: Observations on deformation microstructure, nanoscale dimples and failure by nanovoiding”. In: *Acta Materialia* 60.13-14 (2012), pp. 5160–5171. ISSN: 13596454. DOI: `10.1016/j.actamat.2012.06.014`.

[28] Milos B. Djukic et al. “The synergistic action and interplay of hydrogen embrittlement mechanisms in steels and iron: Localized plasticity and decohesion”. In: *Engineering Fracture Mechanics* 216.February (2019), p. 106528. ISSN: 00137944. DOI: `10.1016/j.engfracmech.2019.106528`. URL: `https://doi.org/10.1016/j.engfracmech.2019.106528`.

[29] Motomichi Koyama et al. “In situ observations of silver-decoration evolution under hydrogen permeation: Effects of grain boundary misorientation on hydrogen flux in pure iron”. In: *Scripta Materialia* 129 (2017), pp. 48–51. ISSN: 13596462. DOI: `10.1016/j.scriptamat.2016.10.027`. URL: `http://dx.doi.org/10.1016/j.scriptamat.2016.10.027`.

[30] E. Protopopoff and P. Marcus. “Corrosion Mechanisms in Theory and Practice”. In: chap. Surface Ef. ISBN: 9781420094633.

[31] Mathias Truschner, Anton Trautmann, and Gregor Mori. “The Basics of Hydrogen Uptake in Iron and Steel”. In: *BHM Berg- und Hüttenmännische Monatshefte* 166.9 (2021), pp. 443–449. ISSN: 0005-8912. DOI: `10.1007/s00501-021-01142-x`.

[32] M. Gao and R. P. Wei. “A ”Hydrogen partitioning” model for hydrogen assisted crack growth”. In: *Metallurgical Transactions A* 16.11 (1985), pp. 2039–2050. ISSN: 03602133. DOI: `10.1007/BF02662405`.

[33] Dell P. Williams and Howard G. Nelson. “Embrittlement of 4130 steel by low-pressure gaseous hydrogen”. In: *Metallurgical Transactions* 1.1 (1970), pp. 63–68. ISSN: 10735615. DOI: `10.1007/BF02819243`.

[34] A. W. Loginow and E. H. Phelps. “Steels for Seamless Hydrogen Pressure Vessels.” In: *American Society of Mechanical Engineers (Paper)* 74 -Pet-4 (1974), pp. 274–282. ISSN: 04021215.

[35] N. E. Nanninga et al. “Comparison of hydrogen embrittlement in three pipeline steels in high pressure gaseous hydrogen environments”. In: *Corrosion Science* 59 (2012), pp. 1–9. ISSN: 0010938X. DOI: `10.1016/j.corsci.2012.01.028`. URL: `http://dx.doi.org/10.1016/j.corsci.2012.01.028`.

[36] Jeffrey Venezuela et al. “Equivalent hydrogen fugacity during electrochemical charging of some martensitic advanced high-strength steels”. In: *Corrosion Science* 127.March (2017), pp. 45–58. ISSN: 0010938X. DOI: `10.1016/j.corsci.2017.08.011`.

[37] Johannes Rehrl et al. “Mechanical properties and fracture behavior of hydrogen charged AHSS/UHSS grades at high- and low strain rate tests”. In: *Materials Science and Engineering: A* 590 (2014), pp. 360–367. ISSN: 09215093. DOI: `10.1016/j.msea.2013.10.044`. URL: `http://dx.doi.org/10.1016/j.msea.2013.10.044`.

[38] Izabela Pietkun-Greber. “Comparison of resistance to damage of unalloyed carbon steels under the influence of hydrogen”. In: *MATEC Web of Conferences* 174 (2018), pp. 0–9. ISSN: 2261236X. DOI: `10.1051/matecconf/201817401015`.

[39] Qian Liu et al. “Determination of the hydrogen fugacity during electrolytic charging of steel”. In: *Corrosion Science* 87 (2014), pp. 239–258. ISSN: 0010938X. DOI: `10.1016/j.corsci.2014.06.033`. URL: `http://dx.doi.org/10.1016/j.corsci.2014.06.033`.

[40] Erik Koren et al. “Experimental comparison of gaseous and electrochemical hydrogen charging in X65 pipeline steel using the permeation technique”. In: *Corrosion Science* 215 (May 2023). ISSN: 0010938X. DOI: `10.1016/j.corsci.2023.111025`.

[41] A Turnbull. “CRITICAL REVIEW OF CORROSION SCIENCE AND ENGINEERING Modeling of the Chemistry and Electrochemistry in Cracks-A Review”. In: *Corrosion* 57.2 (2001), pp. 175–189.

[42] A. Zafra et al. “Hydrogen-assisted fatigue crack growth: Pre-charging vs in-situ testing in gaseous environments”. In: *Materials Science and Engineering: A* 871 (Apr. 2023). ISSN: 09215093. DOI: `10.1016/j.msea.2023.144885`.

[43] I. Moro et al. “Hydrogen embrittlement susceptibility of a high strength steel X80”. In: *Materials Science and Engineering: A* 527.27-28 (2010), pp. 7252–7260. ISSN: 09215093. DOI: `10.1016/j.msea.2010.07.027`.

[44] Y. D. Han et al. “Hydrogen embrittlement sensitivity of X100 pipeline steel under different pre-strain”. In: *International Journal of Hydrogen Energy* 44.39 (2019), pp. 22380–22393. ISSN: 03603199. DOI: `10.1016/j.ijhydene.2019.06.054`.

[45] Yanfei Wang et al. “Hydrogen embrittlement of catholically hydrogen-precharged 304L austenitic stainless steel: Effect of plastic pre-strain”. In: *International Journal of Hydrogen Energy* 39.25 (2014), pp. 13909–13918. ISSN: 03603199. DOI: `10.1016/j.ijhydene.2014.04.122`. URL: `http://dx.doi.org/10.1016/j.ijhydene.2014.04.122`.

[46] Chengshuang Zhou et al. “Effect of pre-strain on hydrogen embrittlement of metastable austenitic stainless steel under different hydrogen conditions”. In: *International Journal of Hydrogen Energy* 44.47 (2019), pp. 26036–26048. ISSN: 03603199. DOI: `10.1016/j.ijhydene.2019.08.046`. URL: `https://doi.org/10.1016/j.ijhydene.2019.08.046`.

[47] J. A. Ronevich et al. “Hydrogen effects in prestrained transformation induced plasticity steel”. In: *Metallurgical and Materials Transactions A: Physical Metallurgy and Materials Science* 43.7 (2012), pp. 2293–2301. ISSN: 10735623. DOI: `10.1007/s11661-011-1075-3`.

[48] J. Gallet et al. “Experimental measurement of dislocation density in metallic materials: A quantitative comparison between measurements techniques (XRD, R-ECCI, HR-EBSD, TEM)”. In: *Materials Characterization* 199.March (2023), p. 112842. ISSN: 10445803. DOI: `10.1016/j.matchar.2023.112842`. URL: `https://doi.org/10.1016/j.matchar.2023.112842`.

[49] Mehul S. Dave et al. “Unravelling NbSe2 single crystal: First principle insights, optical properties, synthesis and X-ray diffraction profile investigation”. In: *Next Materials* 7 (Apr. 2025), p. 100361. ISSN: 29498228. DOI: `10.1016/j.nxmate.2024.100361`.

[50] W. Conshohocken. *Standard Test Method for Measurement of Fracture Toughness 1.* 2001. DOI: `10.1520/E1820-23B`.

[51] N. Nanninga et al. “A review of fatigue crack growth for pipeline steels exposed to hydrogen”. In: *Journal of Research of the National Institute of Standards and Technology* 115.6 (2010), pp. 437–452. ISSN: 1044677X. DOI: `10.6028/jres.115.030`.

[52] Cast Aluminum et al. “Standard Practice for Slow Strain Rate Testing to Evaluate the Susceptibility of Metallic Materials to Environmentally Assisted Cracking 1”. In: *Test* 00.November 2000 (2006), pp. 1–7. DOI: `10.1520/G0129-00R06.2`. URL: `http://www.ncbi.nlm.nih.gov/pubmed/17577132`.

[53] D. Rudomilova, T. Prošek, and G. Luckeneder. “Techniques for investigation of hydrogen embrittlement of advanced high strength steels”. In: *Corrosion Reviews* 36.5 (2018), pp. 413–434. ISSN: 03346005. DOI: `10.1515/corrrev-2017-0106`.

[54] T. Chida et al. “Comparison of constant load, SSRT and CSRT methods for hydrogen embrittlement evaluation using round bar specimens of high strength steels”. In: *ISIJ International* 56.7 (2016), pp. 1268–1275. ISSN: 09151559. DOI: `10.2355/isijinternational.ISIJINT-2015-565`.

[55] *NEN-EN 10025-4+A1.*

[56] S. Anandavijayan et al. “Material pre-straining effects on fatigue behaviour of S355 structural steel”. In: *Journal of Constructional Steel Research* 183 (2021), p. 106707. ISSN: 0143974X. DOI: `10.1016/j.jcsr.2021.106707`. URL: `https://doi.org/10.1016/j.jcsr.2021.106707`.

[57] Victor Igwemezie, Ali Mehmanparast, and Athanasios Kolios. “Current trend in offshore wind energy sector and material requirements for fatigue resistance improvement in large wind turbine support structures – A review”. In: *Renewable and Sustainable Energy Reviews* 101.October 2016 (2019), pp. 181–196. ISSN: 18790690. DOI: `10.1016/j.rser.2018.11.002`. URL: `https://doi.org/10.1016/j.rser.2018.11.002`.

[58] M. Hirofumi, U. Shuji, and M. Ryo. *JFE Engineering’s Initiatives in Offshore Wind Power Foundation Business.* Tech. rep. JFE, Mar. 2023.

[59] S. Anandavijayan et al. “Material pre-straining effects on fracture toughness variation in offshore wind turbine foundations”. In: *Engineering Fracture Mechanics* 252.June 2020 (2021), p. 107844. ISSN: 00137944. DOI: `10.1016/j.engfracmech.2021.107844`. URL: `https://doi.org/10.1016/j.engfracmech.2021.107844`.

[60] G. Álvarez et al. “Hydrogen embrittlement of structural steels: Effect of the displacement rate on the fracture toughness of high-pressure hydrogen pre-charged samples”. In: *International Journal of Hydrogen Energy* 44.29 (2019), pp. 15634–15643. ISSN: 03603199. DOI: `10.1016/j.ijhydene.2019.03.279`.

[61] Muhammad Wasim, Milos B. Djukic, and Tuan Duc Ngo. “Influence of hydrogen-enhanced plasticity and decohesion mechanisms of hydrogen embrittlement on the fracture resistance of steel”. In: *Engineering Failure Analysis* 123 (May 2021). ISSN: 13506307. DOI: `10.1016/j.engfailanal.2021.105312`.

[62] Akihide Nagao et al. “The role of hydrogen in hydrogen embrittlement fracture of lath martensitic steel”. In: *Acta Materialia* 60.13-14 (2012), pp. 5182–5189. ISSN: 13596454. DOI: `10.1016/j.actamat.2012.06.040`. URL: `http://dx.doi.org/10.1016/j.actamat.2012.06.040`.

[63] Akihide Nagao et al. “Interpretation of Hydrogen-induced Fracture Surface Morphologies for Lath Martensitic Steel”. In: *Procedia Materials Science* 3 (2014), pp. 1700–1705. ISSN: 22118128. DOI: `10.1016/j.mspro.2014.06.274`.

[64] E. D. Merson et al. “Quasi-cleavage hydrogen-assisted cracking path investigation by fractographic and side surface observations”. In: *Engineering Fracture Mechanics* 214.April (2019), pp. 177–193. ISSN: 00137944. DOI: `10.1016/j.engfracmech.2019.04.042`. URL: `https://doi.org/10.1016/j.engfracmech.2019.04.042`.

[65] Evgeniy Merson et al. “The fundamental difference between cleavage and hydrogen-assisted quasi-cleavage in ferritic materials revealed by multiscale quantitative fractographic and side surface characterization”. In: *Materials Science and Engineering: A* 824 (Sept. 2021). ISSN: 09215093. DOI: `10.1016/j.msea.2021.141826`.

[66] W Y Choo and Jai Young Lee. *Thermal Analysis of Trapped Hydrogen in Pure Iron*. Tech. rep.

[67] T. Depover et al. “Understanding the interaction between a steel microstructure and hydrogen”. In: *Materials* 11.5 (2018). ISSN: 19961944. DOI: `10.3390/ma11050698`.

[68] Qinglong Liu et al. “Equivalent Hydrogen Fugacity during Electrochemical Charging of 980DP Steel Determined by Thermal Desorption Spectroscopy”. In: *Advanced Engineering Materials* 20.1 (2018). ISSN: 15272648. DOI: `10.1002/adem.201700469`.

[69] Timing Zhang et al. “Comparison of hydrogen embrittlement susceptibility of three cathodic protected subsea pipeline steels from a point of view of hydrogen permeation”. In: *Corrosion Science* 131.November 2017 (2018), pp. 104–115. ISSN: 0010938X. DOI: `10.1016/j.corsci.2017.11.013`. URL: `https://doi.org/10.1016/j.corsci.2017.11.013`.

[70] Vorgelegt Von and M Sc Qi Gao. *Investigations on Hydrogen Embrittlement of Advanced High Strength Steels for Automotive Applications*. Tech. rep.

[71] Andreas Drexler et al. “Critical verification of the Kissinger theory to evaluate thermal desorption spectra”. In: *International Journal of Hydrogen Energy* 46.79 (2021), pp. 39590–39606. ISSN: 03603199. DOI: `10.1016/j.ijhydene.2021.09.171`. URL: `https://doi.org/10.1016/j.ijhydene.2021.09.171`.

[72] Y. T. Tang et al. “Profilometry-based indentation plastometry to obtain stress-strain curves from anisotropic superalloy components made by additive manufacturing”. In: *Materialia* 15 (Mar. 2021). ISSN: 25891529. DOI: `10.1016/j.mtla.2021.101017`.

[73] Trevor William Clyne et al. *Profilometry-Based Inverse Finite Element Method Indentation Plastometry*. Sept. 2021. DOI: `10.1002/adem.202100437`.

[74] Oliver Brätz and Knuth Michael Henkel. “Investigations on the microstructure of drawn arc stud welds on structural steels by quantitative metallography”. In: *Welding in the World* 67.1 (2023), pp. 195–208. ISSN: 18786669. DOI: `10.1007/s40194-022-01417-y`. URL: `https://doi.org/10.1007/s40194-022-01417-y`.

[75] M. Itakura et al. “The effect of hydrogen atoms on the screw dislocation mobility in bcc iron: A first-principles study”. In: *Acta Materialia* 61.18 (Oct. 2013), pp. 6857–6867. ISSN: 13596454. DOI: `10.1016/j.actamat.2013.07.064`.

[76] M. Wen, S. Fukuyama, and K. Yokogawa. “Atomistic simulations of effect of hydrogen on kink-pair energetics of screw dislocations in bcc iron”. In: *Acta Materialia* 51.6 (Apr. 2003), pp. 1767–1773. ISSN: 13596454. DOI: `10.1016/S1359-6454(02)00575-X`.

[77] Jai Young Lee and S. M. Lee. “Hydrogen trapping phenomena in metals with B.C.C. and F.C.C. crystals structures by the desorption thermal analysis technique”. In: *Surface and Coatings Technology* 28.3-4 (1986), pp. 301–314. ISSN: 02578972. DOI: `10.1016/0257-8972(86)90087-3`.

[78] L. Cupertino-Malheiros et al. “Hydrogen Diffusion and Trapping in Low-Alloy Tempered Martensitic Steels”. In: *Metallurgical and Materials Transactions A: Physical Metallurgy and Materials Science* 54.4 (Apr. 2023), pp. 1159–1173. ISSN: 10735623. DOI: `10.1007/s11661-023-06967-4`.

[79] Maoqiu Wang, Eiji Akiyama, and Kaneaki Tsuzaki. “Effect of hydrogen and stress concentration on the notch tensile strength of AISI 4135 steel”. In: *Materials Science and Engineering: A* 398.1-2 (2005), pp. 37–46. ISSN: 09215093. DOI: `10.1016/j.msea.2005.03.008`.

[80] Jurij J. Sidor et al. “Assessment of dislocation density by various techniques in cold rolled 1050 aluminum alloy”. In: *Metals* 11.10 (Oct. 2021). ISSN: 20754701. DOI: `10.3390/met11101571`.

[81] Chengsi Zheng et al. “Micromechanical behavior of eutectoid steel quantified by an analytical model calibrated by in situ synchrotron-based X-ray diffraction”. In: *Materials Science and Engineering: A* 631 (Apr. 2015), pp. 181–188. ISSN: 09215093. DOI: `10.1016/j.msea.2015.02.003`.

[82] Jin Ho Park, Min Suk Oh, and Sung Jin Kim. “Effect of bainite in microstructure on hydrogen diffusion and trapping behavior of ferritic steel used for sour service application”. In: *Journal of Materials Research* 32.7 (Apr. 2017), pp. 1295–1303. ISSN: 20445326. DOI: `10.1557/jmr.2016.480`.

[83] Binglu Zhang et al. “Improving the hydrogen embrittlement resistance by straining the ferrite / cementite interfaces”. In: *Acta Materialia* 270 (May 2024). ISSN: 13596454. DOI: `10.1016/j.actamat.2024.119850`.

A Methodology to fit TDS spectra for binding energy determination

Both fitting methods are carried out in Spyder with the help of ChatGPT.

A.1 Single Gaussian Fit

The steps followed to obtain the binding energies of the different traps with a single Gaussian function are:

1. A Gaussian function (Eq. 15 is used to model the hydrogen desorption peaks at different heating rates.

$$G(T) = A \cdot e^{-\frac{(T-T_{max})^2}{2\sigma^2}} \tag{15}$$

   where:

   - T is the instantaneous temperature
   - G(T) is the hydrogen desorption rate
   - A is the fitted amplitude of the peak,
   - T_{max} is the temperature at which the maximum hydrogen desorption takes place,
   - σ is the fitted standard deviation of the peak

2. Convert $T_{max}(°C)$ into $T_{max}(K)$.
3. Apply the Kissinger equation.
4. Generate Choo-Lee plot.

A.2 Double Gaussian Fit (Deconvolution)

To calculate the binding energies assuming that each peak of the TDS spectra is made by two Gaussian equations, the next procedure is followed:

1. For the double Gaussian deconvolution, the equation becomes Eq. 16:

$$G(T) = A_1 \cdot e^{-\frac{(T-T_{max,1})^2}{2\sigma_1^2}} + A_2 \cdot e^{-\frac{(T-T_{max,2})^2}{2\sigma_2^2}} \tag{16}$$

   where each peak is represented by:

   - T: instantaneous temperature
   - $G(T)_i$: hydrogen desorption rate
   - A_i: fitted amplitude of the peak,
   - $T_{max,i}$: temperature at which the maximum hydrogen desorption takes place,
   - σ_i: fitted standard deviation of the peak

2. Compare areas of Peak 1 and Peak 2. Assume that when the difference between them is greater than 10%, the deconvolution is not correct.

3. Convert $T_{max}(^\circ C)$ into $T_{max}(K)$.
4. Apply the Kissinger equation.
5. Generate Choo-Lee plot.

B Double Gaussian fit deconvolution of TDS spectra

In this section, the deconvolution of TDS spectra into two Gaussian functions (Peak 1 and Peak 2) is shown for the different levels of pre-strain and microstructures.

B.1 2% pre-strain TM samples

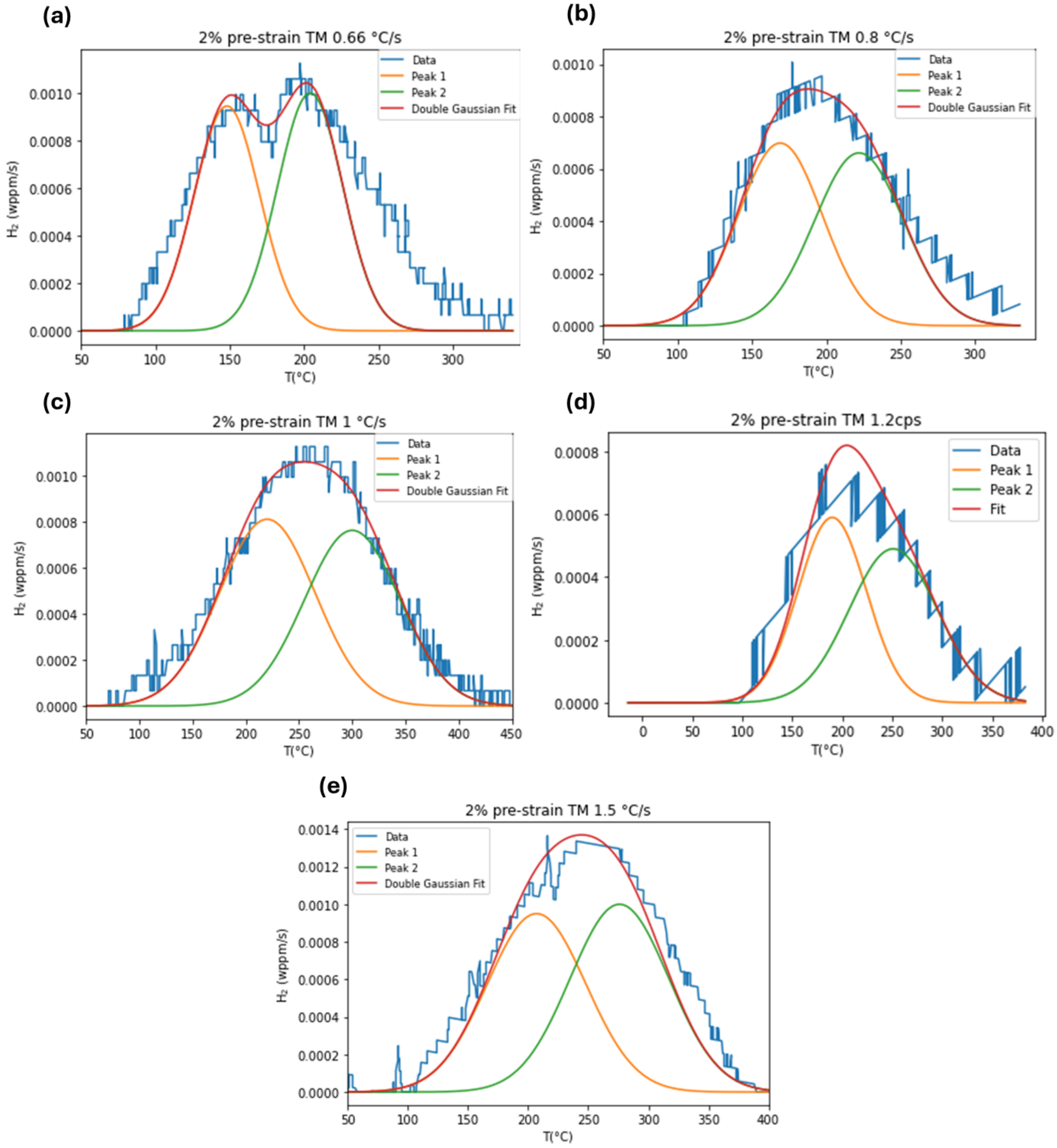

Figure 48: Deconvolution of the TDS spectra of 2% pre-strained TM samples into two Gaussian curves for (a) 0.66 °C/s, (b) 0.8 °C/s, (c) 1 °C/s , (c) 1.2 °C/s and (d) 1.5 °C/s

B.2 8% pre-strain

B.2.1 8 % pre-strain TM samples

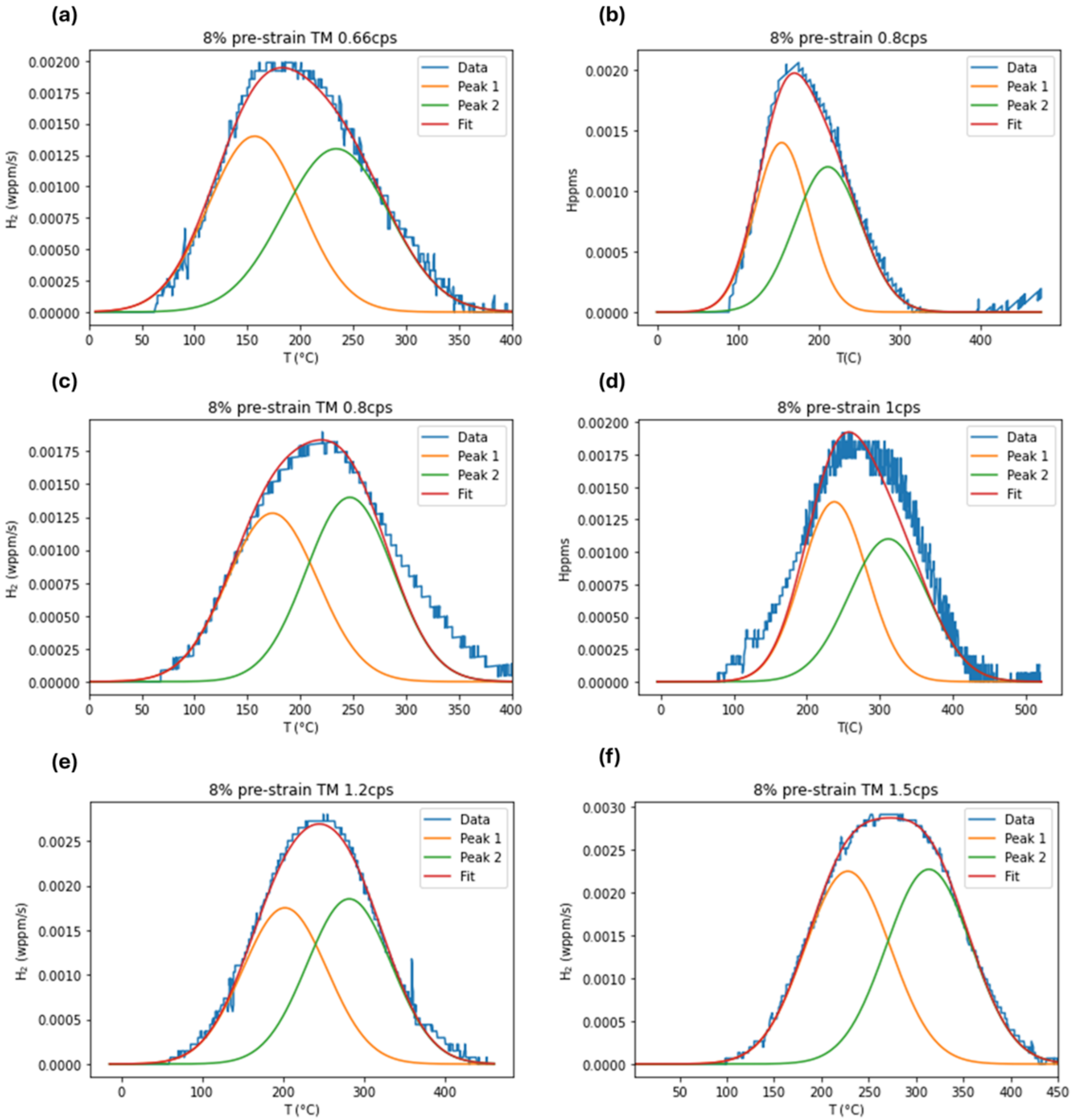

Figure 49: Deconvolution of the TDS spectra of 8% pre-strained TM samples into two Gaussian curves for (a) 0.66 °C/s, (b, c) 0.8 °C/s, (d) 1 °C/s, (e) 1.2 °C/s and (e) 1.5 °C/s

B.2.2 8 % pre-strain 1050AC samples

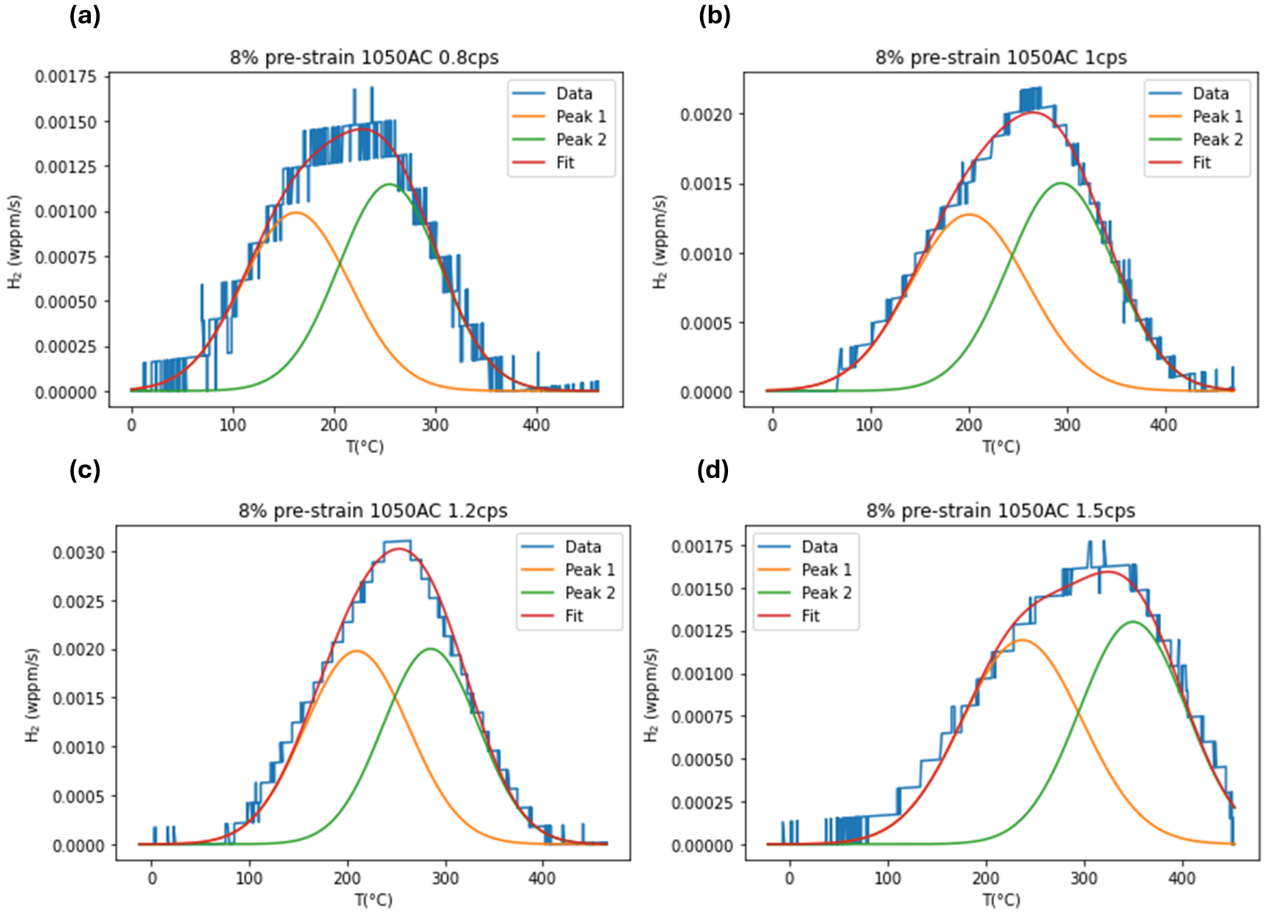

Figure 50: Deconvolution of the TDS spectra of 8% pre-strained 1050AC samples into two Gaussian curves for (a) 0.8 °C/s, (b) 1 °C/s, (c) 1.2 °C/s and (d) 1.5 °C/s

B.3 16% pre-strain TM samples

B.3.1 16% pre-strain TM samples, 194mm/min crosshead displacement

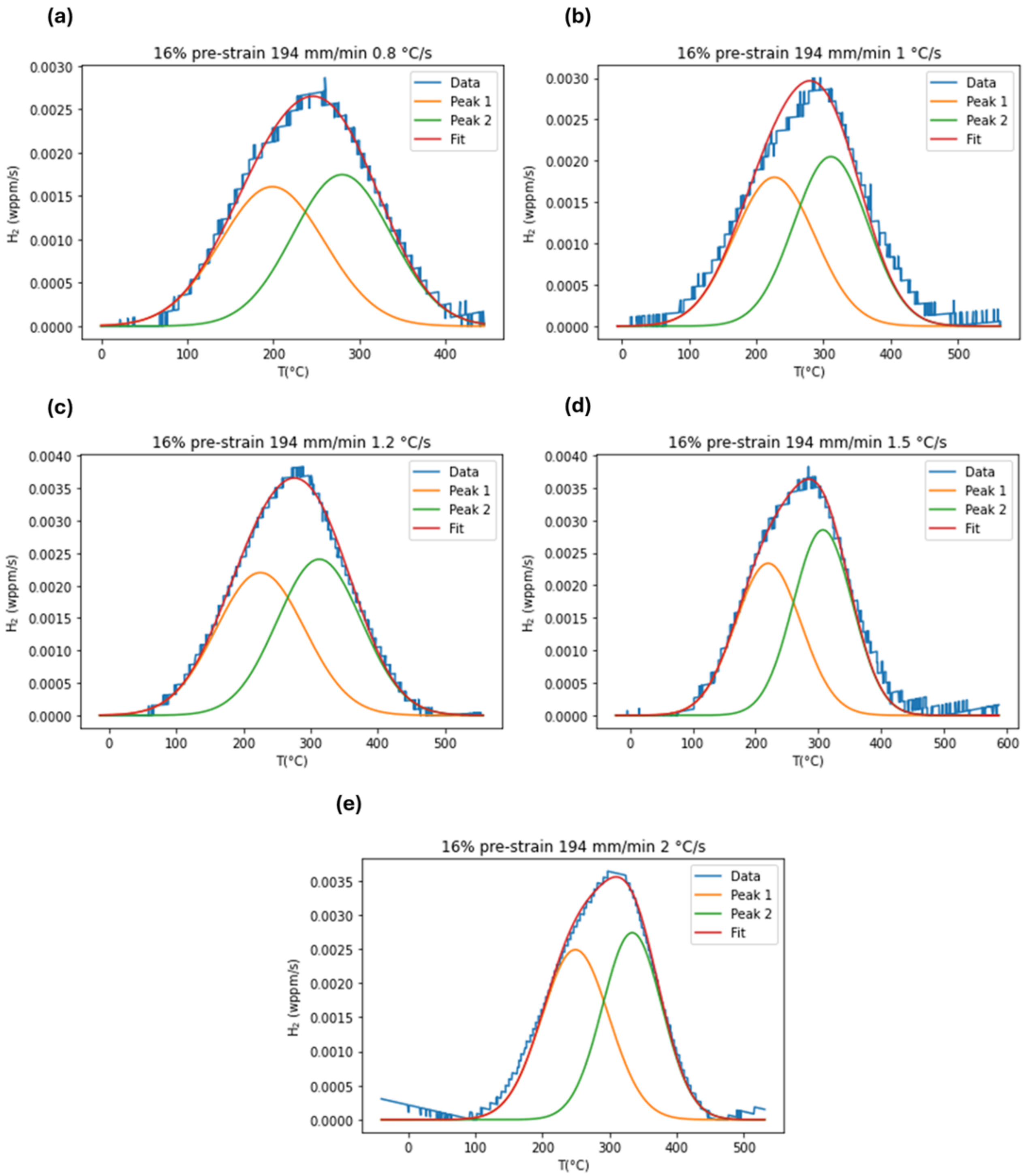

Figure 51: Deconvolution of the TDS spectra of TM samples pre-strained 16% at 194mm/min into two Gaussian curves for (a) 0.8 °C/s, (b) 1 °C/s, (c) 1.2 °C/s, (d) 1.5 °C/s and (e) 2 °C/s

B.3.2 16% pre-strain TM samples, 1mm/min crosshead displacement

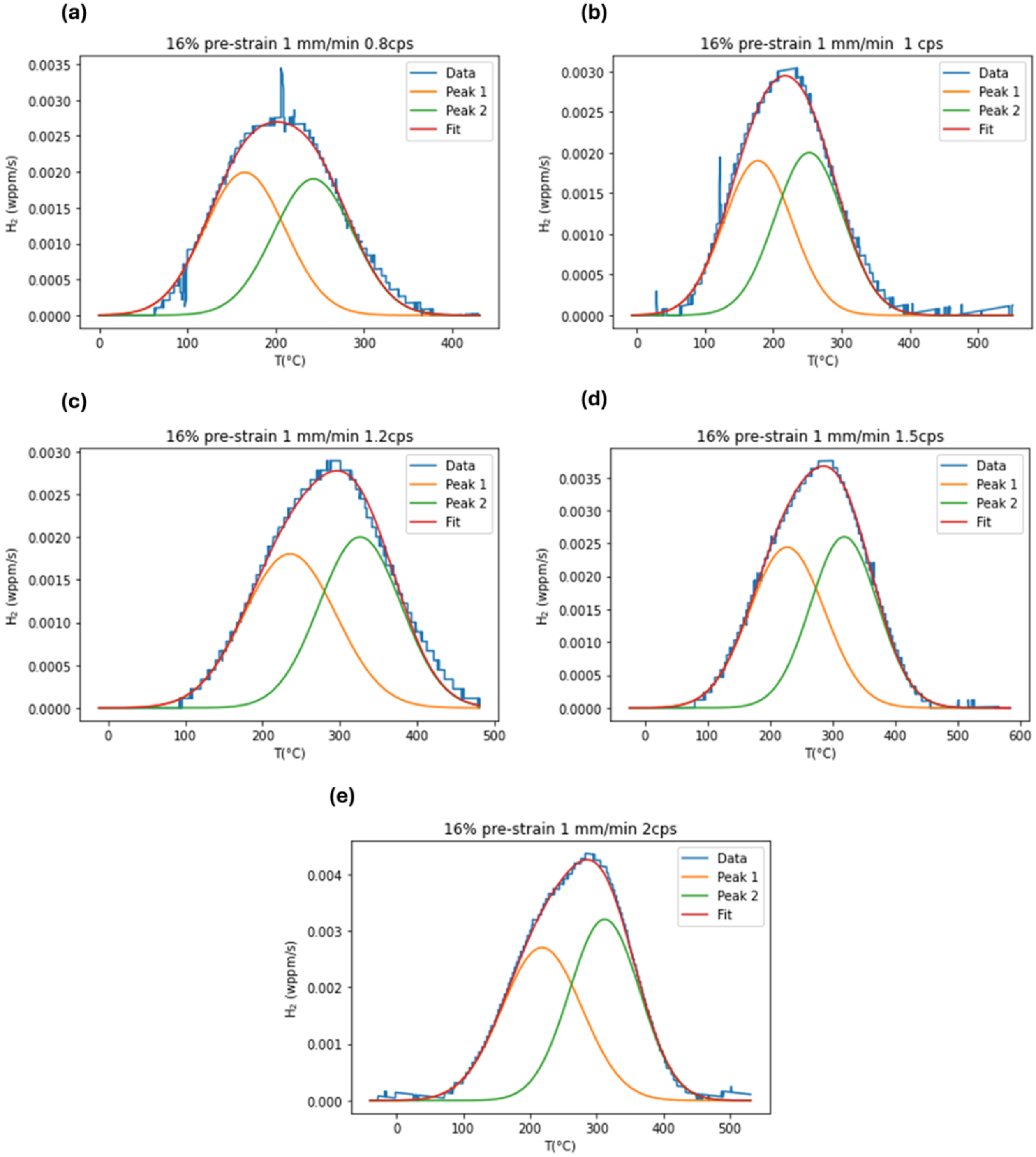

Figure 52: Deconvolution of the TDS spectra of TM samples pre-strained 16% at 1mm/min into two Gaussian curves for (a) 0.8 °C/s, (b) 1 °C/s, (c) 1.2 °C/s, (d) 1.5 °C/s and (e) 2 °C/s

C Filter data points for trapping energy calculation

TDS peaks move towards higher temperatures with increasing heating rates because the hydrogen does not have time to effuse at lower ones.

Regarding this, it is easy to get an idea only by looking to Fig. 57 (a) that some peaks are not ”well located” with respect to the other ones, that is why a filtering method was implemented. The filtered peaks will be the ones taken into account to calculate the binding energy of the traps. appear in Fig. 57 (b).

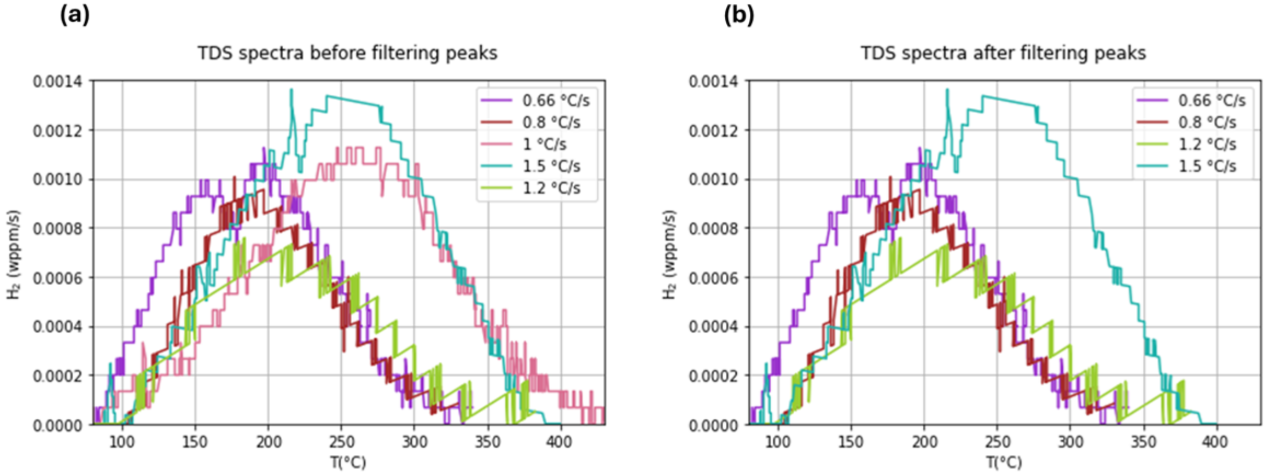

Figure 53: TDS spectra of 2% pre-strained samples at different heating rates. (a) All heating rates tested. (b) Valid TDS spectra used to apply the Kissinger theory.

The filtering process is carried out to eliminate unreliable data points from the Choo-Lee plot by eliminating values with a relative error greater than 5%, ensuring that only high-quality data contributes to the final activation energy calculation. This filter step provides a more reliable estimation of activation energy.

The stepsfollowed are:

1. Compute Absolute and Relative Errors: A linear regression is plotted to model the peak temperature T_{max} as a function of the heating rate. The absolute and relative errors from the actual temperatures to the regression line are calculated using the Eq. 17:

   The absolute error is computed as:

$$\text{Error}_{\text{absolute}} = |T_{\text{measured}} - T_{\text{predicted}}| \tag{17}$$

   where:

   - T_{measured} is the experimentally measured peak temperature.
   - $T_{\text{predicted}}$ is the temperature of the linear regression.

   The relative error is then calculated as shown in Eq. 18:

$$\mathrm{Error}_{\mathrm{relative}\ (\%)} = \frac{|T_{\mathrm{actual}} - T_{\mathrm{predicted}}|}{|T_{\mathrm{actual}}|} \times 100 \tag{18}$$

2. Filter data: Data points with a relative error greater than 5% are removed.
3. Repeat Choo-Lee analysis with filtered data

C.1 2% pre-strain

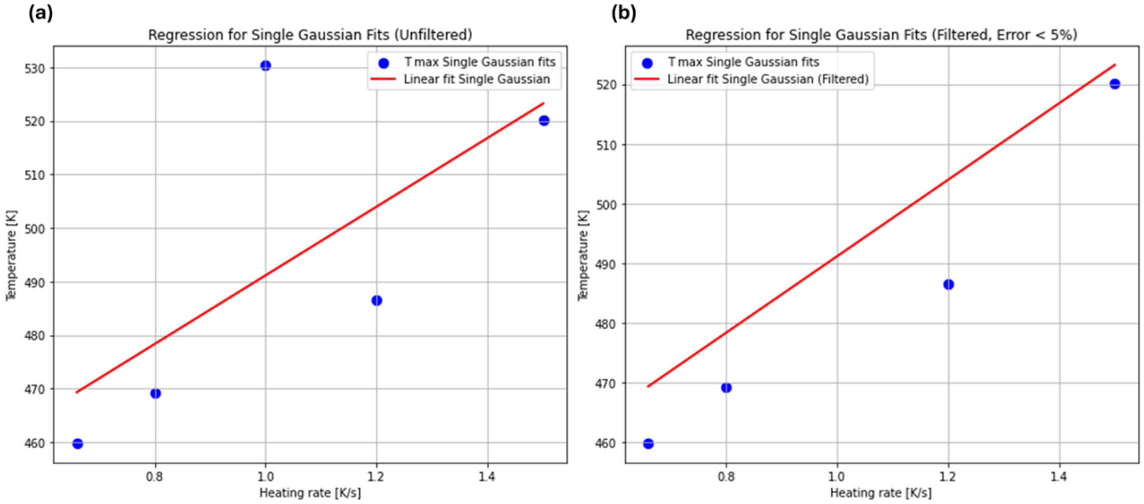

Figure 54: Filter data points of single Gaussian fit 2% pre-strained TM samples for trapping energy calculation. (a) all data point tested (b) data points to be used in Kissinger Theory to determine the hydrogen binding energy

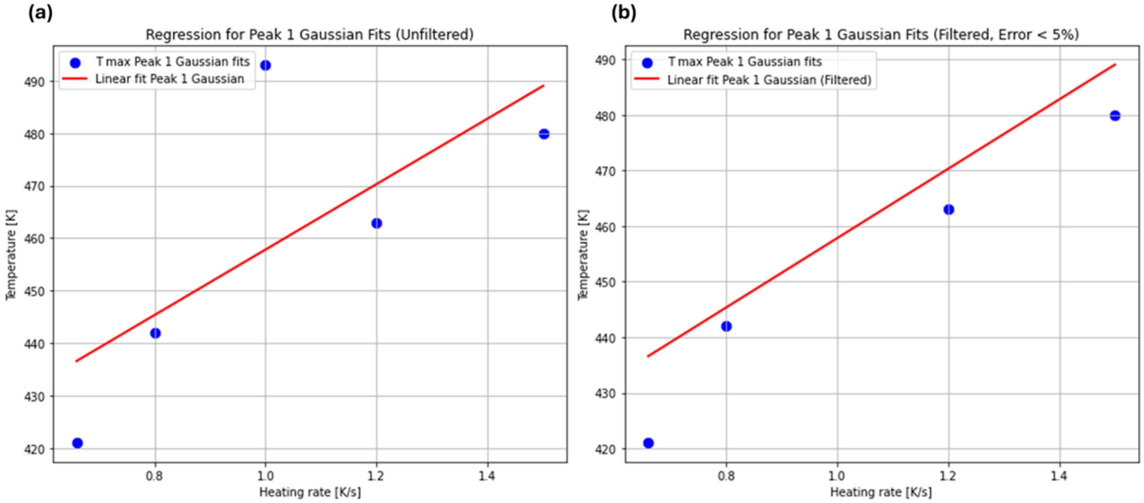

Figure 55: Filter data points of Peak 1 of double Gaussian fit 2% pre-strained TM samples for trapping energy calculation. (a) all data point tested (b) data points to be used in Kissinger Theory to determine the hydrogen binding energy

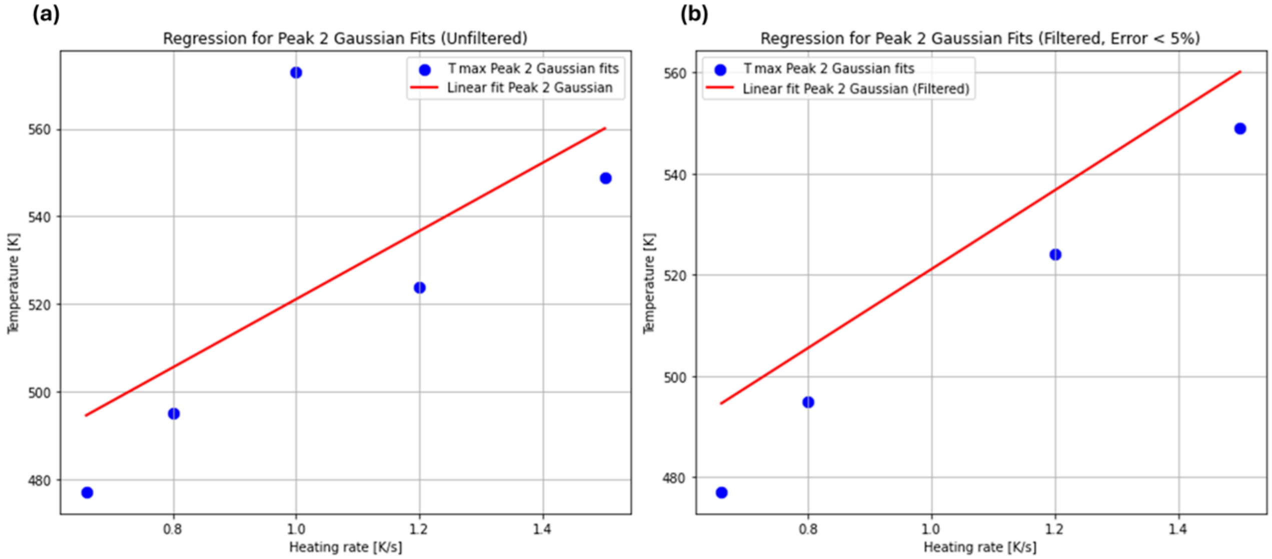

Figure 56: Filter data points of Peak 2 of double Gaussian fit 2% pre-strained TM samples for trapping energy calculation. (a) all data point tested (b) data points to be used in Kissinger Theory to determine the hydrogen binding energy

C.1.1 Results of filtering

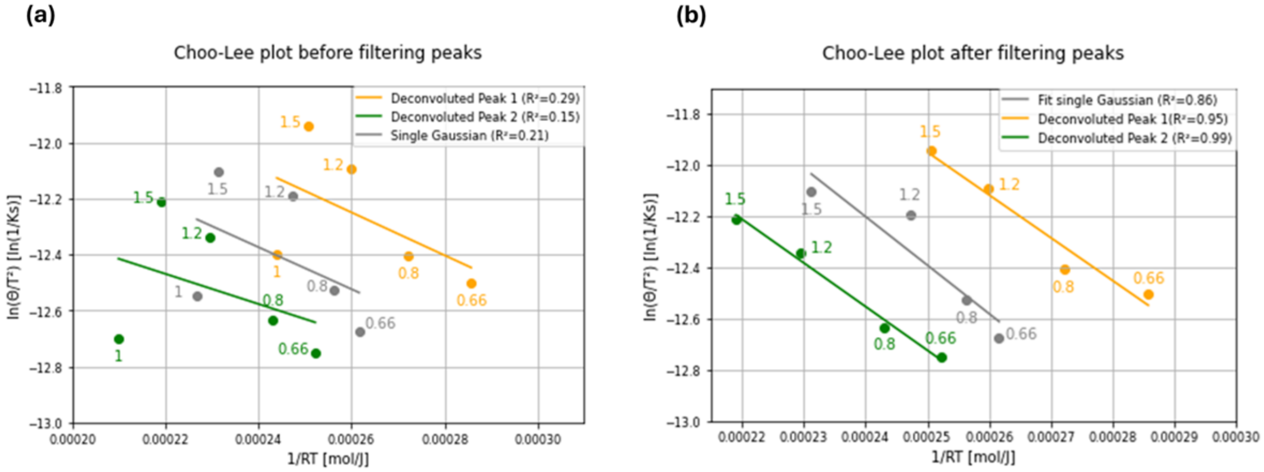

Figure 57: Choo-Lee plots of 2% pre-strained TM samples when (a) taking into account all TDS peaks, and (b) when only considering filtered TDS spectra.

C.2 8% pre-strain

C.2.1 8 % pre-strain TM samples

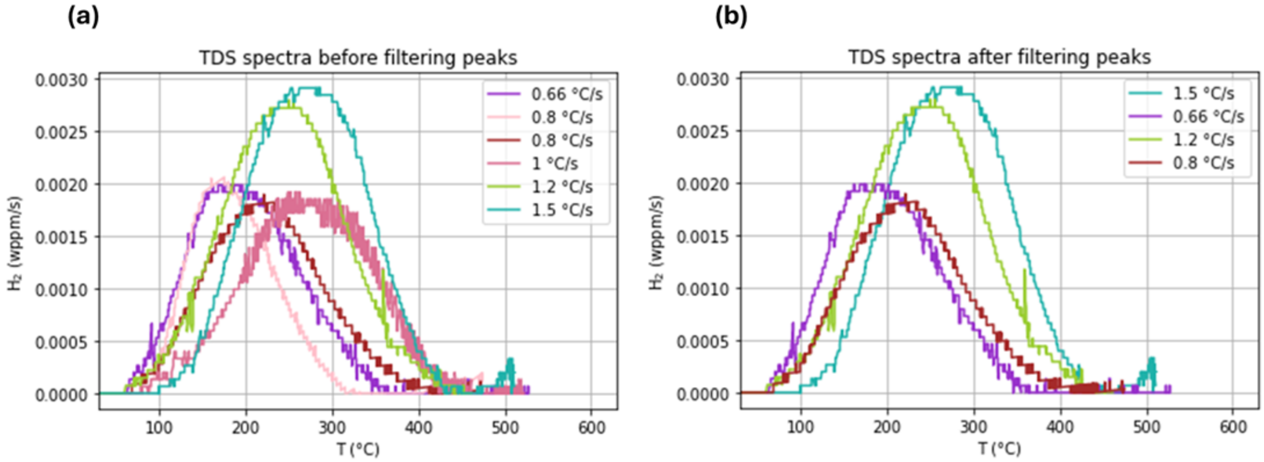

Figure 58: TDS spectra of 8% pre-strained samples at different heating rates. (a) All heating rates tested. (b) Valid TDS spectra used to apply the Kissinger theory.

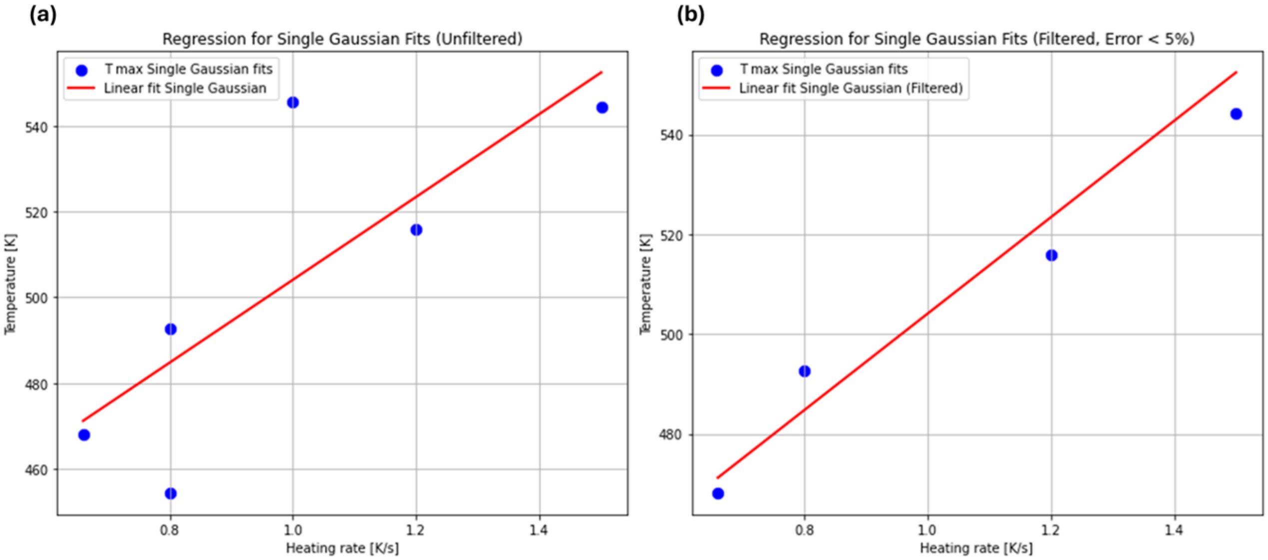

Figure 59: Filter data points of single Gaussian fit for 8% pre-strained TM samples for trapping energy calculation. (a) all data point tested (b) data points to be used in Kissinger Theory to determine the hydrogen binding energy

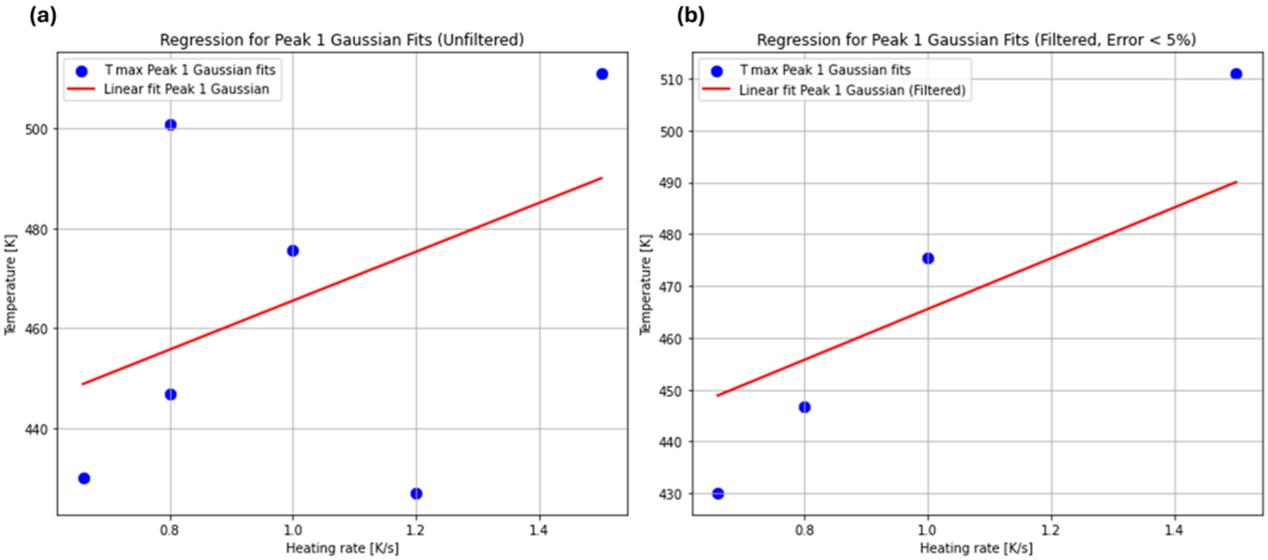

Figure 60: Filter data points of double Gaussian fit's Peak 1 for 8% pre-strained TM samples for trapping energy calculation. (a) all data point tested (b) data points to be used in Kissinger Theory to determine the hydrogen binding energy

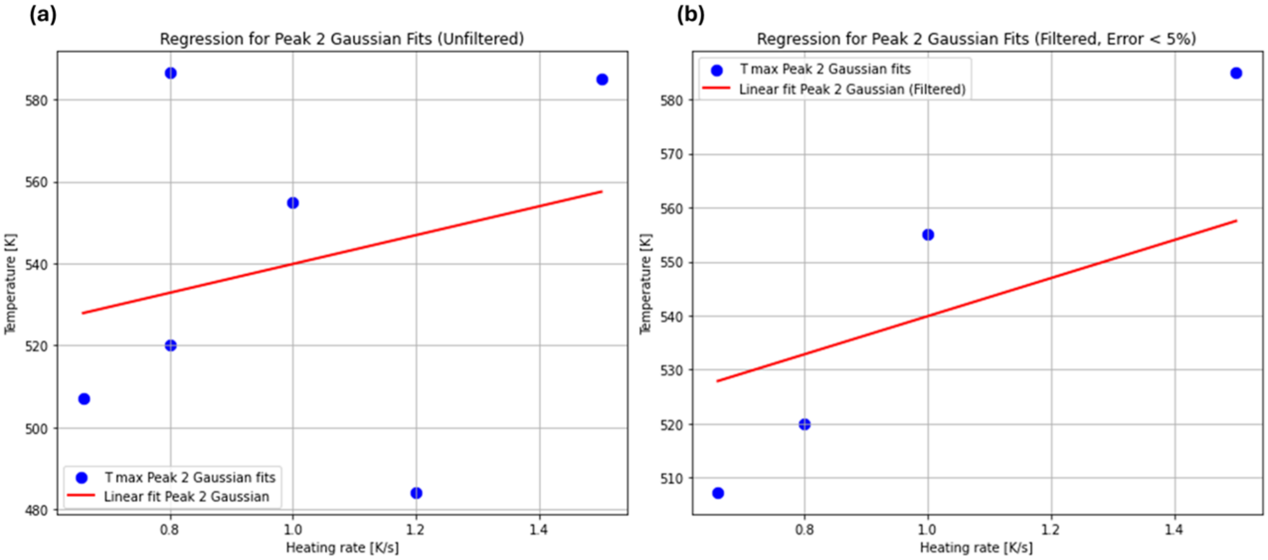

Figure 61: Filter data points of double Gaussian fit's Peak 2 for 8% pre-strained TM samples for trapping energy calculation. (a) all data point tested (b) data points to be used in Kissinger Theory to determine the hydrogen binding energy

C.2.2 Results of filtering

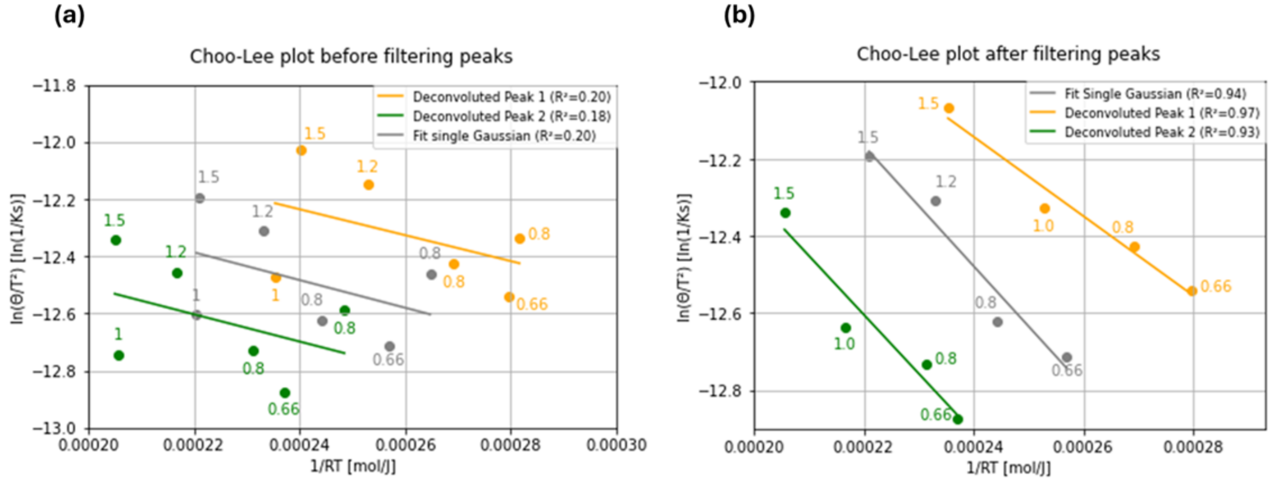

Figure 62: Choo-Lee plots of 8% pre-strained TM samples when (a) taking into account all TDS peaks, and (b) when only considering filtered TDS spectra.

C.2.3 8 % pre-strain 1050AC samples

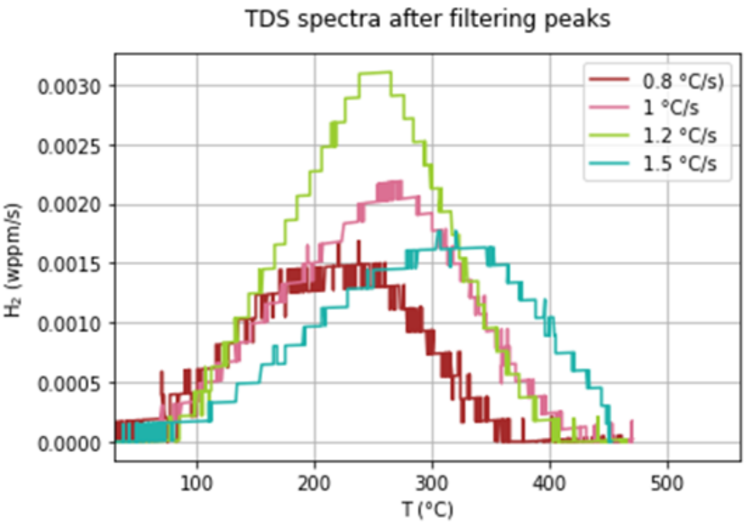

Figure 63: TDS spectra of 8% pre-strained 1050AC samples at different heating rates used to apply the Kissinger theory.

C.3 16 % pre-strain

Fig. 64 shows in (a) all the samples tested and in (b) only the filtered peaks. The comparison of the two fitting methods is plotted in Fig. 29

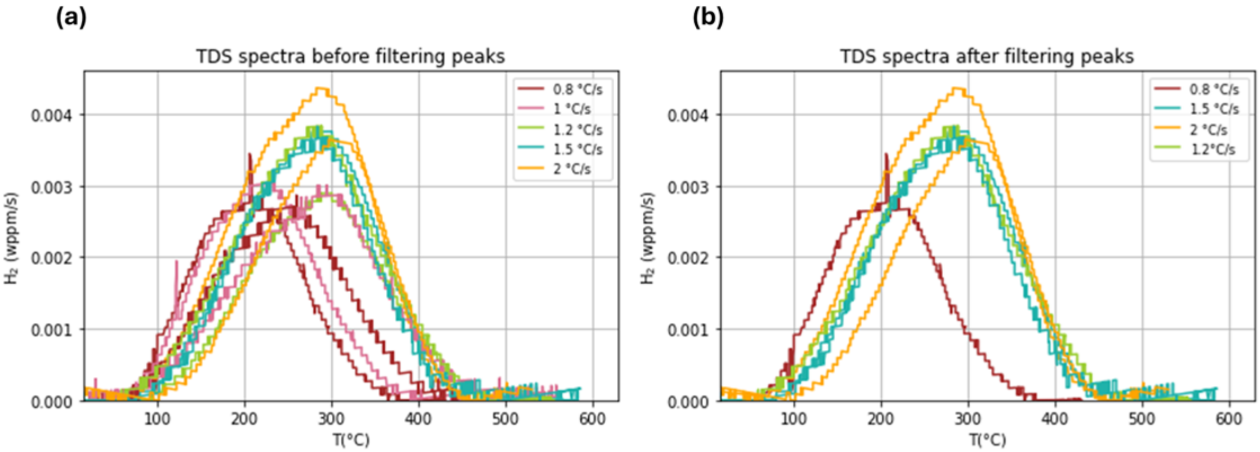

Figure 64: TDS spectra of TM samples pre-strained 16% at different heating rates used to apply the Kissinger theory.

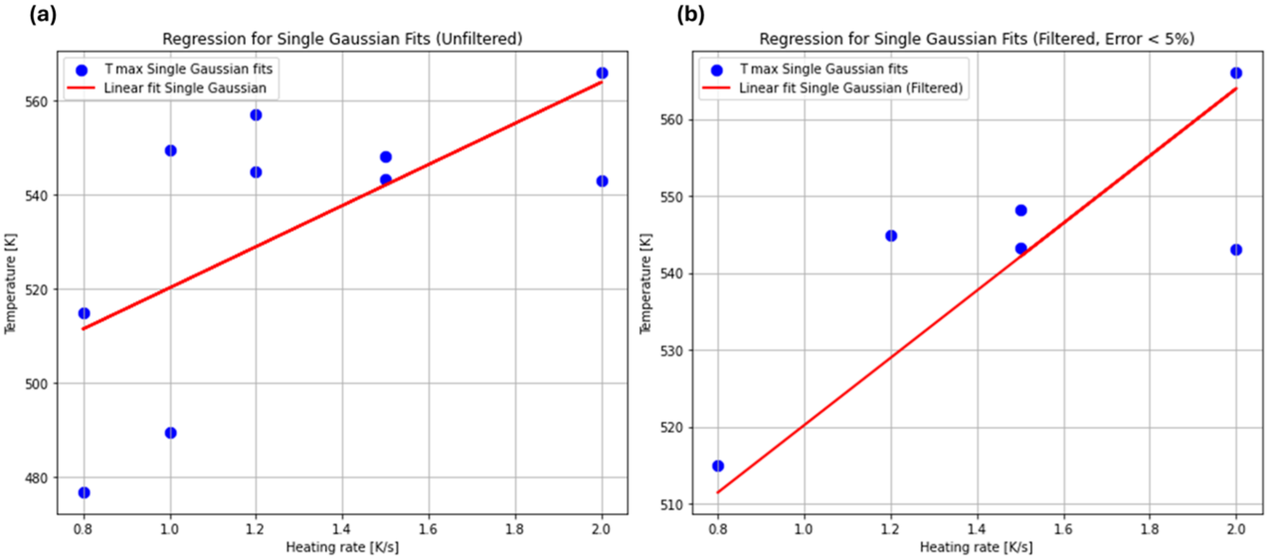

Figure 65: Filter data points of single Gaussian fit for 16% pre-strained TM samples for trapping energy calculation. (a) all data point tested (b) data points to be used in Kissinger Theory to determine the hydrogen binding energy

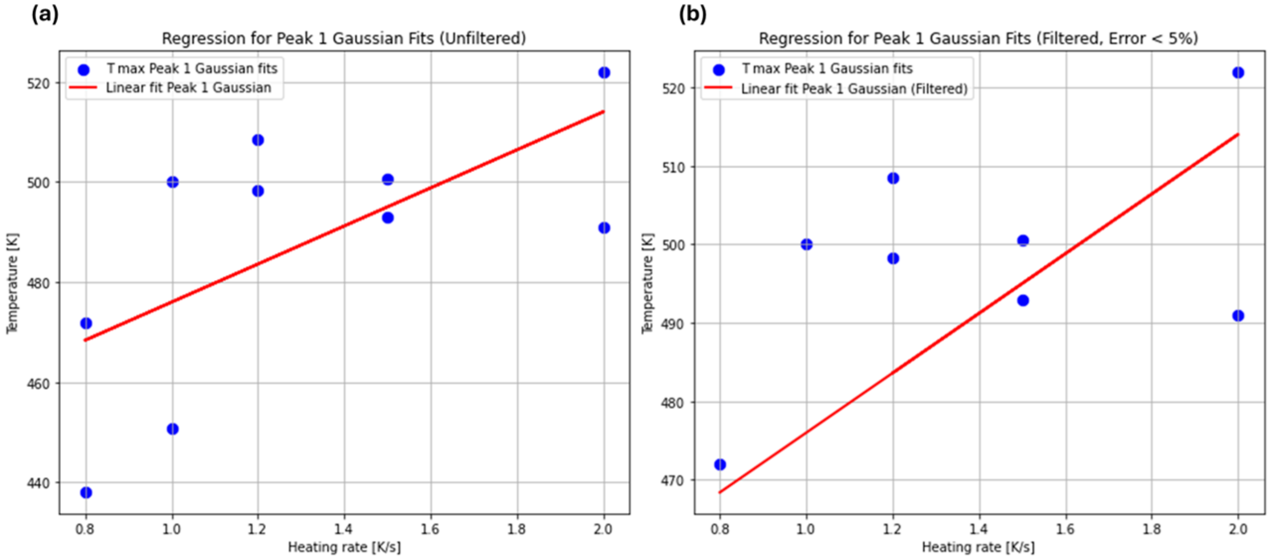

Figure 66: Filter data points of double Gaussian fit's Peak 1 for 16% pre-strained TM samples for trapping energy calculation. (a) all data point tested (b) data points to be used in Kissinger Theory to determine the hydrogen binding energy

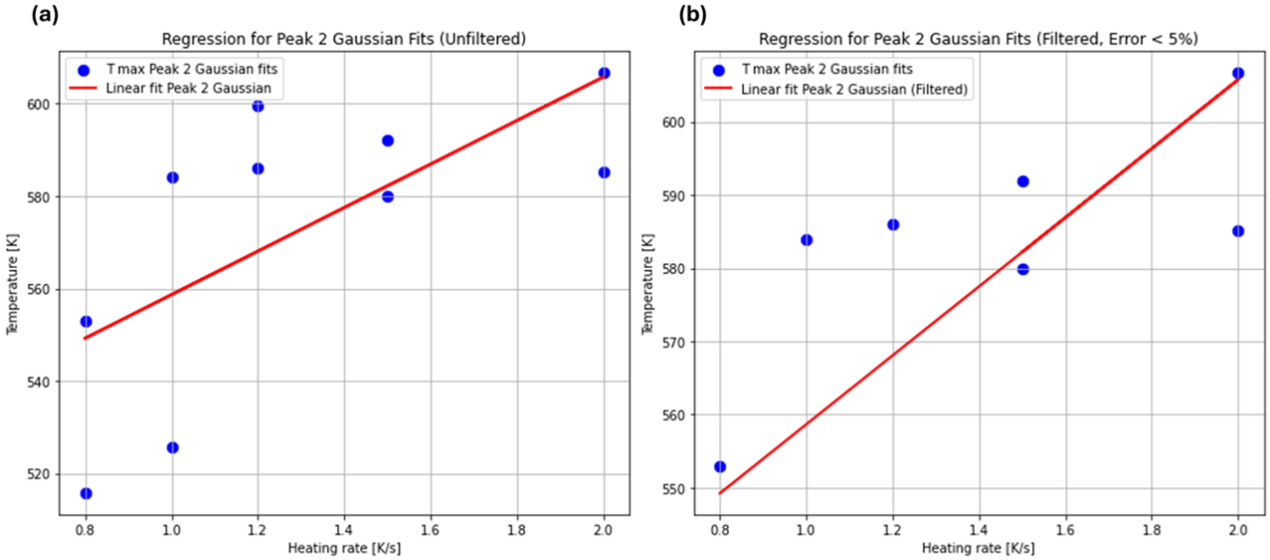

Figure 67: Filter data points of double Gaussian fit's Peak 2 for 16% pre-strained TM samples for trapping energy calculation. (a) all data point tested (b) data points to be used in Kissinger Theory to determine the hydrogen binding energy

C.3.1 Results of filtering

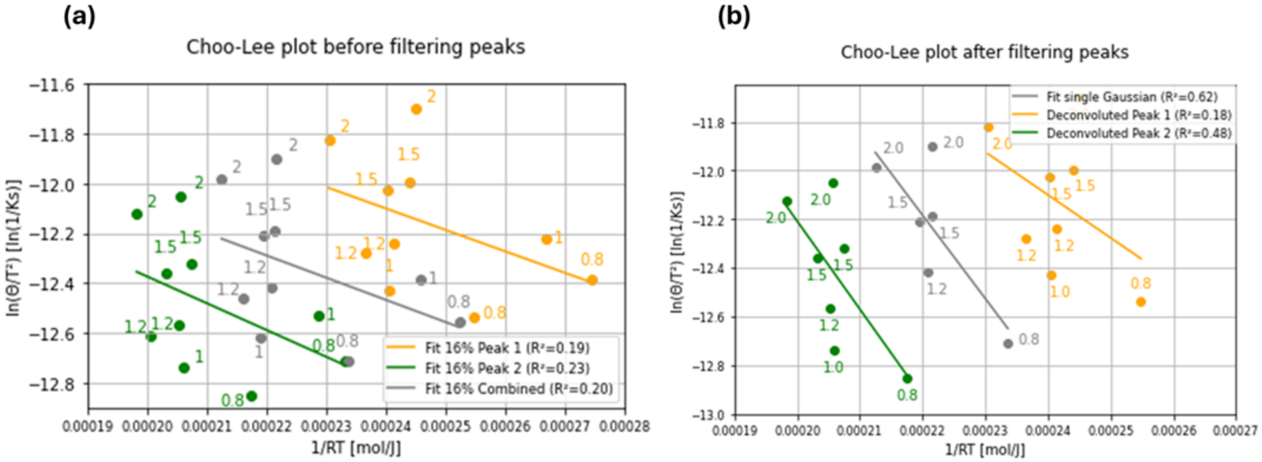

Figure 68: Choo-Lee plots of 16% pre-strained TM samples when (a) taking into account all TDS peaks, and (b) when only considering filtered TDS spectra.

D Comparison of XRD spectra of 0% and 8% pre-strained TM samples

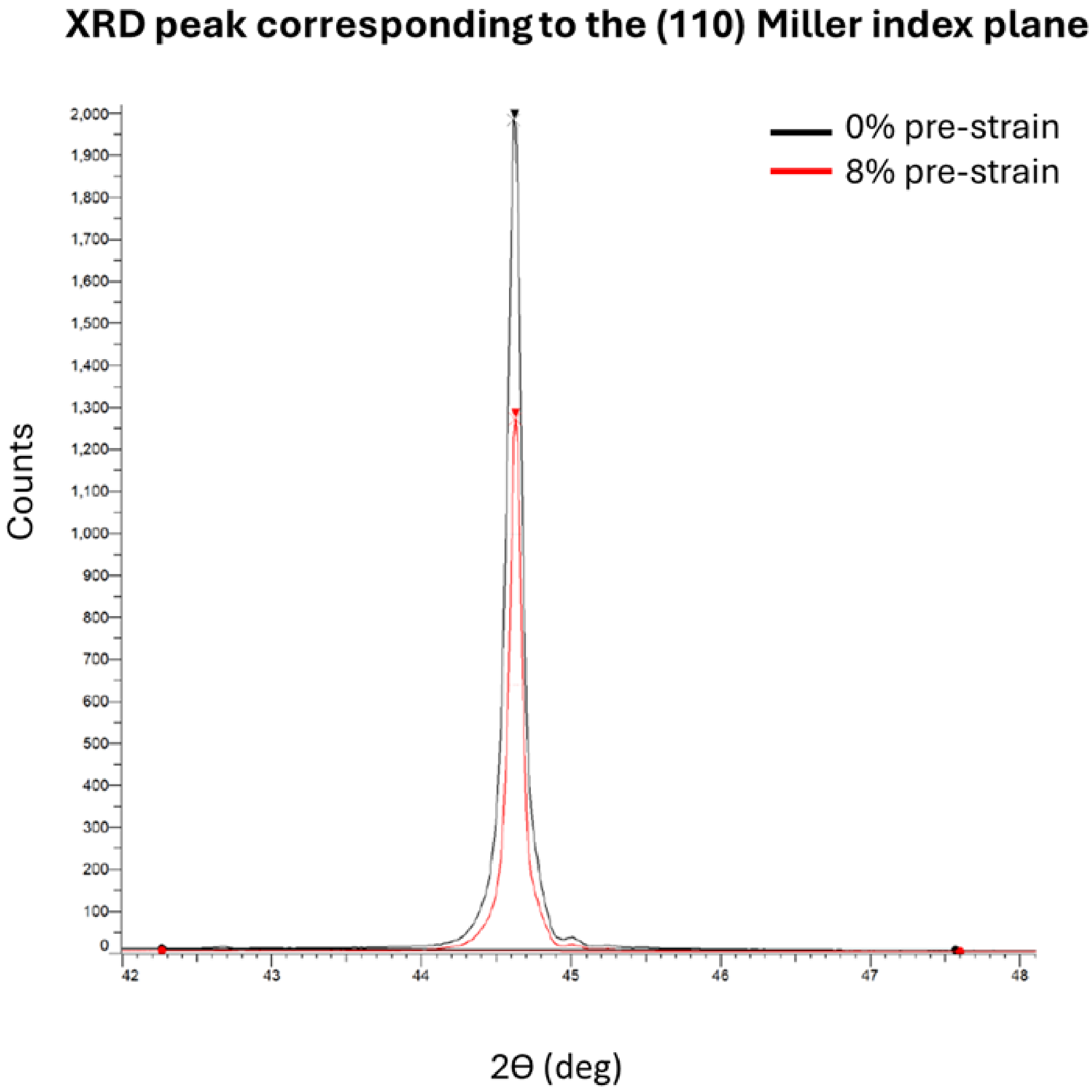

Figure 69: Close up of the XRD peak correspondint to (110)

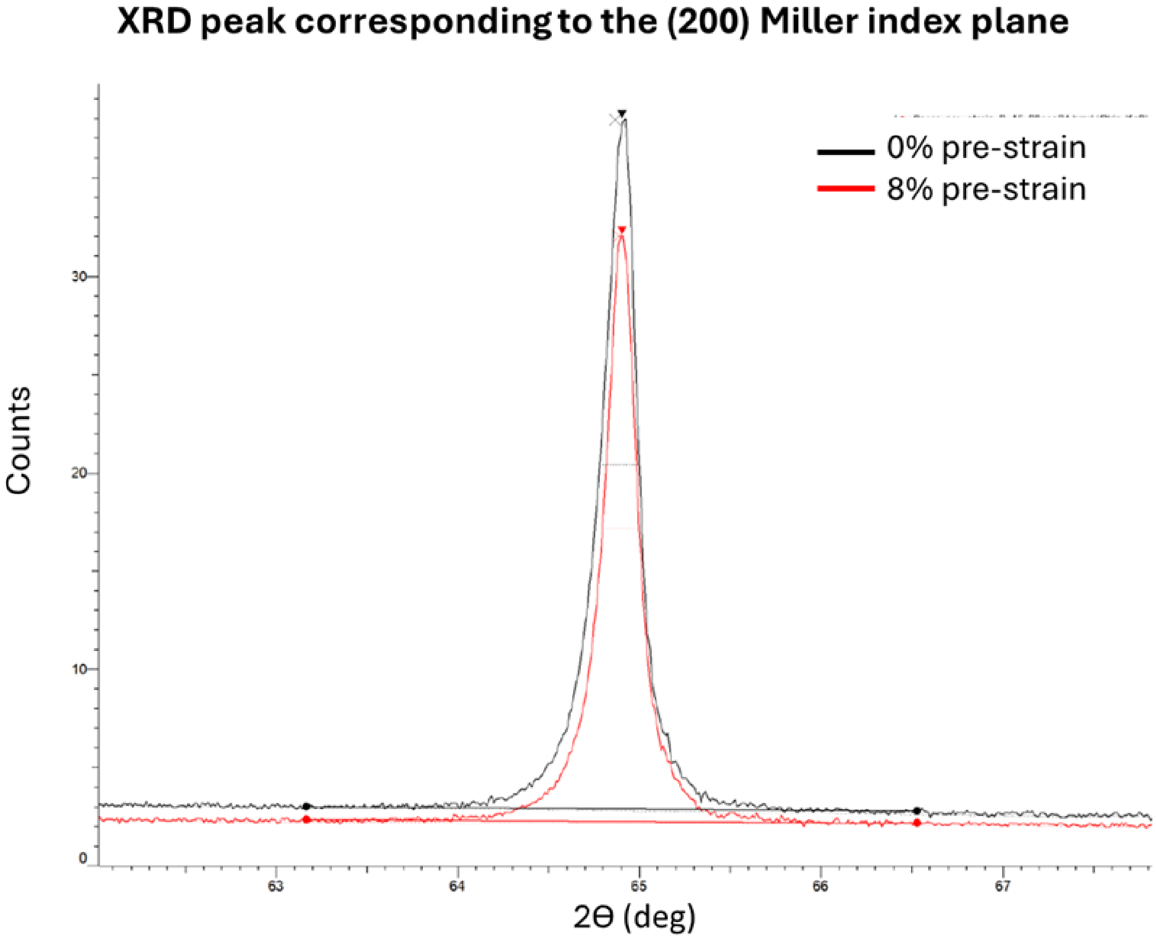

Figure 70: Close up of the XRD peak correspondint to (200)

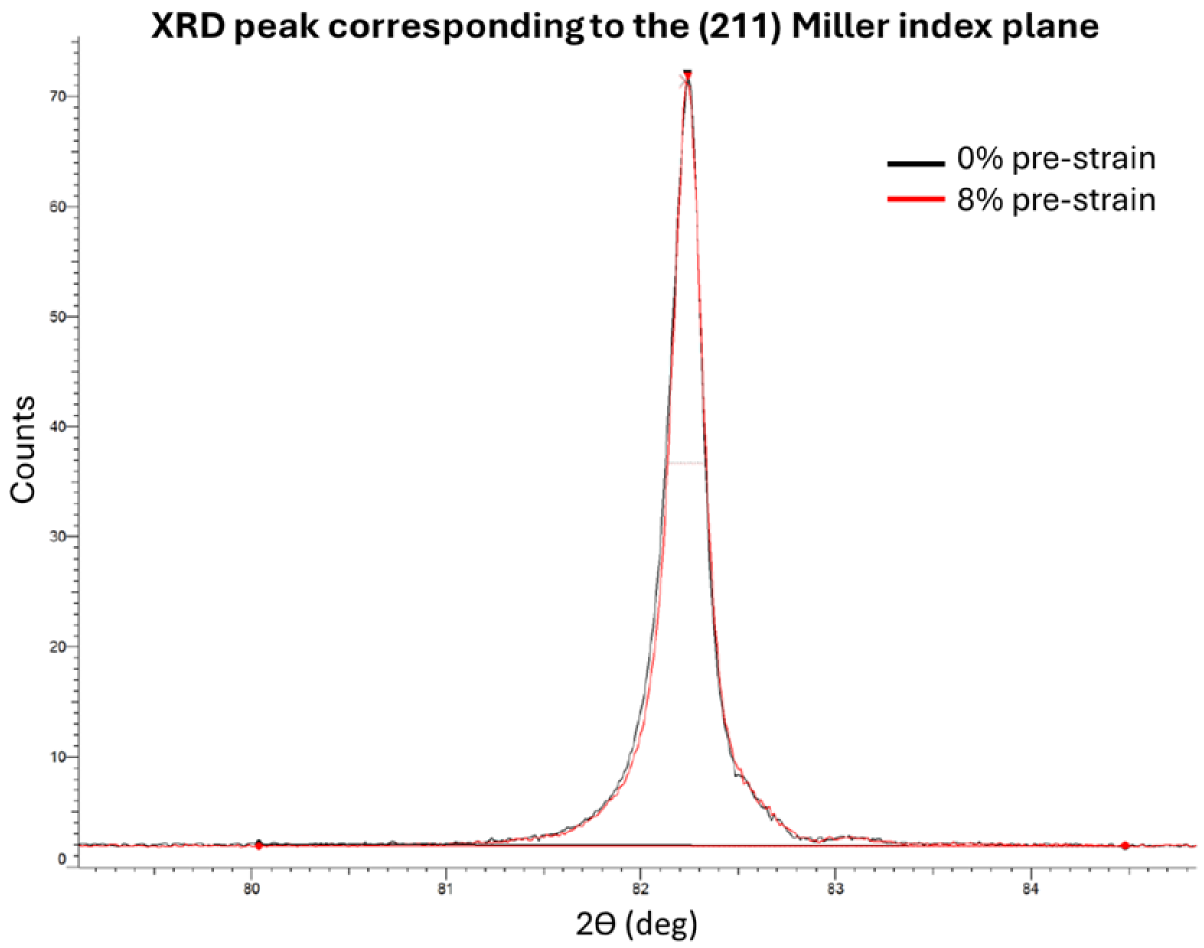

Figure 71: Close up of the XRD peak correspondint to (211)

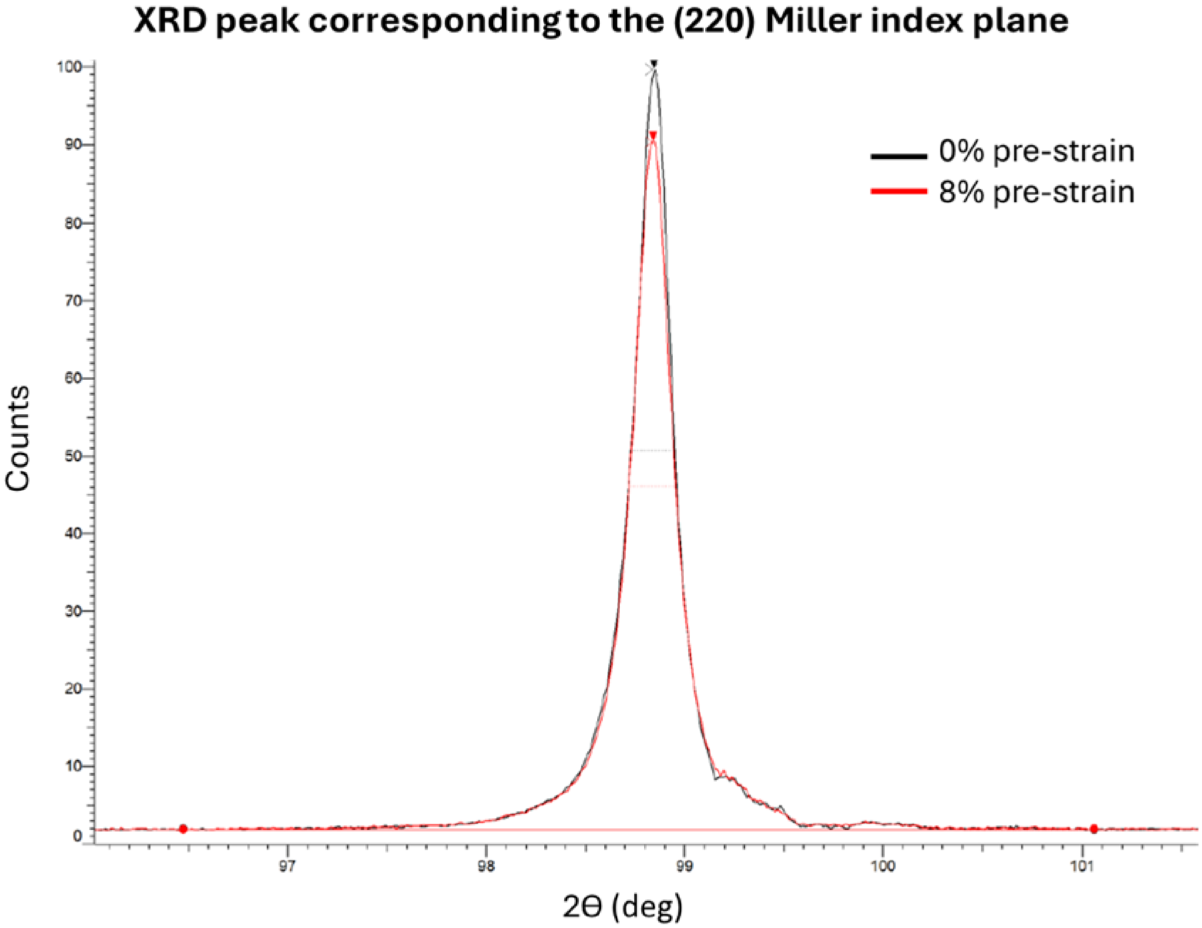

Figure 72: Close up of the XRD peak correspondint to (220)

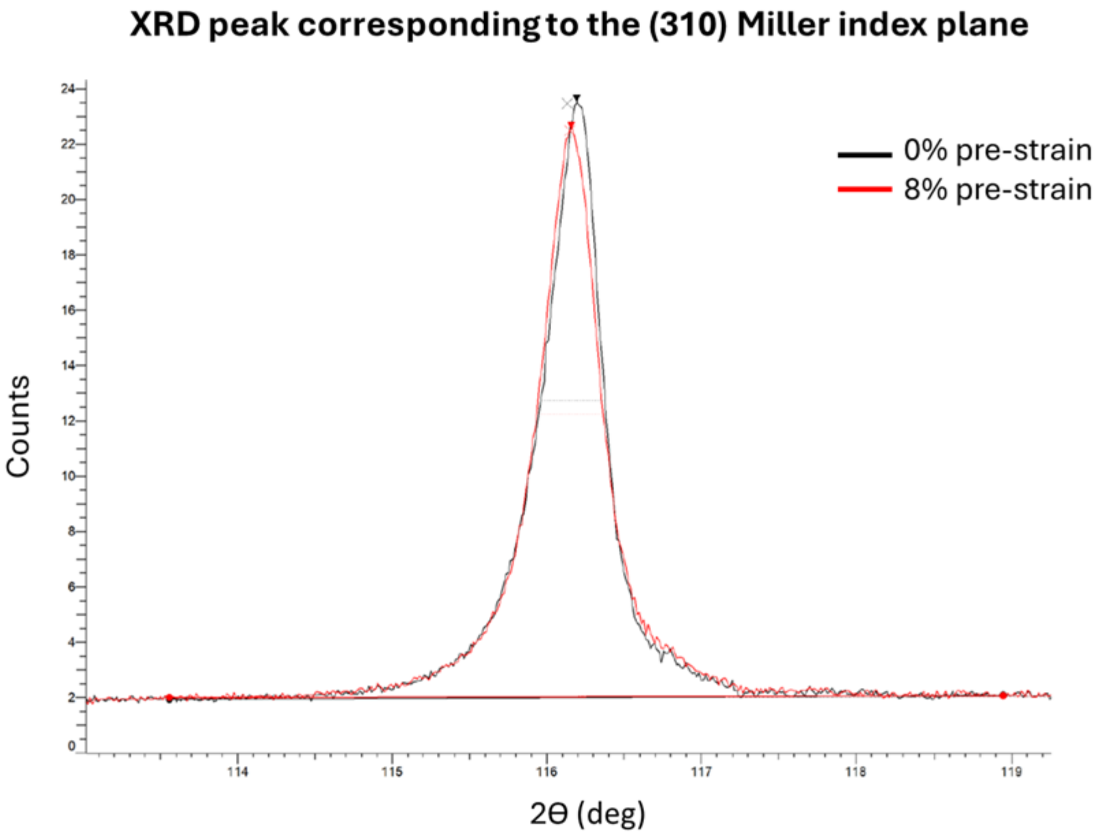

Figure 73: Close up of the XRD peak correspondint to (310)

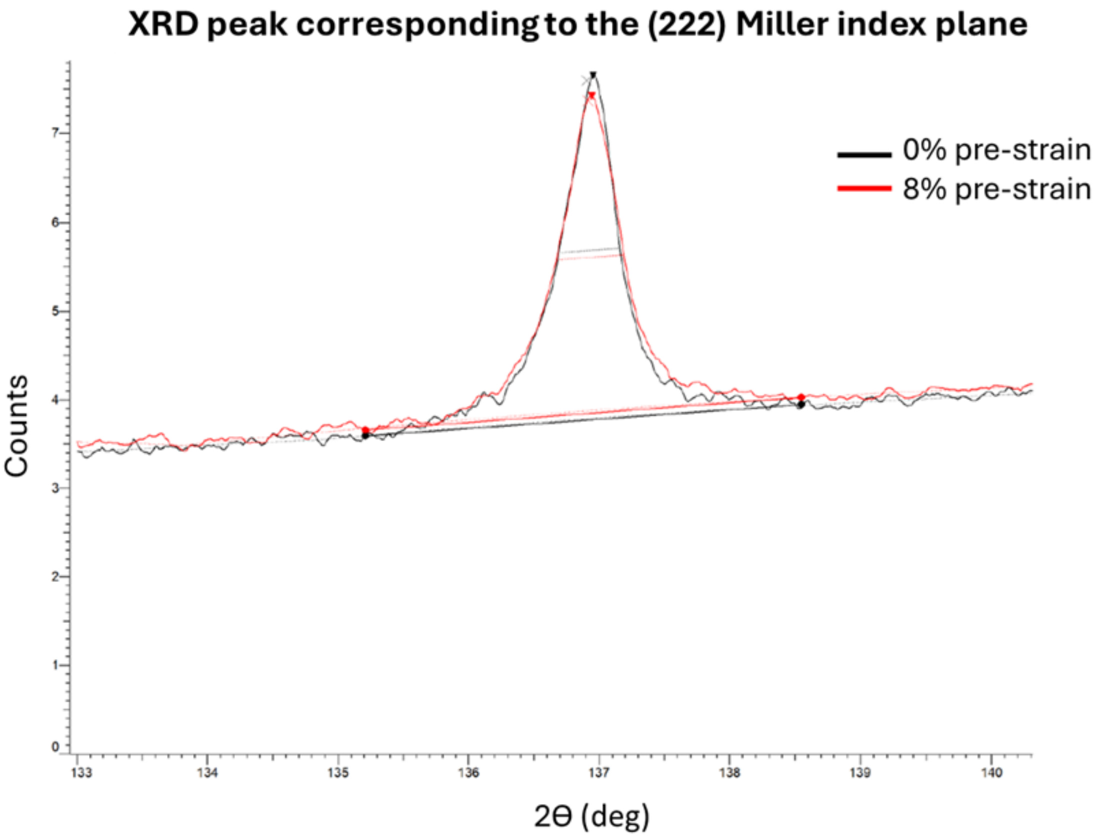

Figure 74: Close up of the XRD peak correspondint to (222)

D.1 Data for 0 % pre-strain TM sample

Table 18: Table of XRD Parameters and Calculations

XRD Peak Parameters for the 0% pre-strained TM sample					
hkl	**Obs. Max** (deg)	**FWHM** (deg)	**Instr broad** (deg)	**FWHM-corr** (deg)	**Ehkl** (GPa)
110	45	0.11	0.023	0.11	2.2e+02
200	65	0.22	0.01	0.22	1.3e+02
211	82	0.2	0.02	0.2	2.2e+02
220	99	0.22	0.031	0.22	2.2e+02
310	1.2e+02	0.42	0.05	0.41	1.5e+02
222	1.4e+02	0.47	0.092	0.46	2.8e+02

D.2 Data for 8 % pre-strain TM sample

Table 19: Table of XRD Parameters for the 8% pre-strained TM sample

XRD Peak Parameters and Calculations					
hkl	**Obs. Max** (deg)	**FWHM** (deg)	**Instr broad** (deg)	**FWHM-corr** (deg)	**Ehkl** (GPa)
110	45	0.095	0.023	0.092	2.2e2
200	65	0.20	0.010	0.20	1.3e2
211	82	0.20	0.020	0.20	2.2e2
220	99	0.24	0.031	0.23	2.2e2
310	1.2e2	0.43	0.050	0.42	1.5e2
222	1.4e2	0.52	0.092	0.51	2.8e2